

Carnegie Mellon University

CARNEGIE INSTITUTE OF TECHNOLOGY

THESIS

SUBMITTED IN PARTIAL FULFILLMENT OF THE REQUIREMENTS

FOR THE DEGREE OF Doctor of Philosophy

TITLE

A Physics-Based, Eulerian-Lagrangian Computational Modeling Framework to Predict Particle Flow and Tribological Phenomena

PRESENTED BY

Jeremiah N. Mpagazehe

ACCEPTED BY THE DEPARTMENT OF MECHANICAL ENGINEERING

ADVISOR, MAJOR PROFESSOR

DATE

DEPARTMENT HEAD

DATE

APPROVED BY THE COLLEGE COUNCIL

DEAN

DATE

A Physics-Based, Eulerian-Lagrangian Computational Modeling Framework to Predict Particle Flow and Tribological Phenomena

Submitted in partial fulfillment of the requirements for

the degree of

Doctor of Philosophy

in

Mechanical Engineering

by

Jeremiah N. Mpagazehe

Carnegie Mellon University
Pittsburgh, PA

May 2013

Copyright 2013, Jeremiah N. Mpagazehe

To My Parents, My Brother, and My Sister

Abstract

Tribology – the science and technology of interacting surfaces in relative motion and the related subjects of friction, lubrication and wear – is an important aspect in industrial and natural systems. Multiphase flows, specifically particle-fluid flows, are present in many such tribological processes. Therefore, an increased understanding of the dynamics of particles in fluids and their interaction with the surrounding surfaces is a critical step in improving related industrial processes, many of which contain fluid-mediated sliding contacts. Interestingly, the primary physics which govern a vast number of particle-fluid processes are often similar. As a result, in this work a modeling framework is developed as a general approach to study particle-fluid systems. The modeling approach employs a physics-based, Eulerian-Lagrangian framework in order to predict the performance of applications that involve particle flow and tribological phenomena. More specifically, computational fluid dynamics (CFD) is used to model the Eulerian fluid phase, while the discrete element method (DEM) is used to model the particulate phase from a Lagrangian perspective. The modeling framework is applied to study abrasive wear and erosive wear processes and the results are validated with experimental data obtained during the course of this research.

In this thesis, the Eulerian CFD solver is introduced and validated for its spatial and temporal accuracy with analytical solutions for fluid flow. Two different spatial discretization schemes for the CFD were studied and their comparison is presented in Chapter 2. Similarly to the Eulerian phase, a lengthy discussion of the Lagrangian, DEM

solver is presented in Chapter 3. The implementation of Verlet tables to increase computational efficiency is detailed.

A critical step in the implementation of the framework is in determining the phase interactions. Chapter 4 is dedicated to discussing the particle-particle, particle-fluid, particle-surface, and surface-fluid interactions which are captured by the framework. Stokes drag and Ergun drag are implemented in the framework to provide solutions for different flow conditions. Additionally, the framework can capture the effect of particle heat transfer which is important in heated, packed particle beds. Various case studies are performed and compared to experiments or analytical solutions to validate the model's phase coupling. The framework's ability to predict vortex shedding frequencies for flow around a cylinder using the immersed boundary method matches well to experimental results.

Erosive wear and rotary drilling (Chapters 6 and 7) are two particle-fluid applications to which the framework is applied. By modeling the behavior of the multi-phase flow in those tribo-systems, it is possible to predict their tribological behavior prior to observing them in real life. As a result, money and time can be saved by having a “virtual laboratory” in which the effect of design and/or operational parameters on the system's behavior can be simulated.

Acknowledgements

I would like to thank my parents for creating an environment in which the pursuit, application, and discussion of knowledge were always encouraged. The values they instilled in me at an early age, their support of my scientific curiosity, and the examples they set have had the greatest impact on my life and productivity thus far.

I would also like to thank my sister, my brother, and my extended family for their continual support and encouragement.

There were many people who were instrumental in helping me to complete this research. However, most of all was my advisor, Dr. C. Fred Higgs III, from whom I have learned a great deal.

I would also like to sincerely thank the other members of my committee, Dr. Kenneth W. Street, Jr. (NASA), Dr. Philip R. LeDuc (CMU), and Dr. Shawn Litster (CMU) for their support, questioning, and thoughtful review of this work. Their contribution helped to broaden the applicability of this research.

I am extremely grateful to the NASA Glenn Research Center, especially the Tribology and Mechanical Components Branch, for kindly welcoming me into their laboratory each summer. Specifically, I would like to thank Irebert R. Delgado for all of his time, encouragement, and advice during my time in the NASA GSRP program. Additionally, Dr. Philip Abel's generous support during this project was greatly appreciated. I would be remiss if I did not mention the great efforts of Richard (Rick) Mondry, Jr. who was extremely helpful each summer with testing and imaging. While at NASA, the kind

encouragement of Dr. Malcolm Stanford, Dr. Christopher DellaCorte, and Fransua Thomas, was greatly appreciated.

There were many opportunities that were given to me to explore my affinity for engineering and science. I would like to thank Robert (Bob) M. for providing one of these very important opportunities very early in my career.

I am thankful to the previous researchers in the Particle Flow and Tribology Laboratory (PFTL) for their contributions as they served as a foundation for my research. Specifically, I would like to thank Dr. Elon Terrell for his modeling efforts in chemical mechanical polishing which greatly influenced the work in this thesis. I also had the opportunity to work with many graduate and undergraduate students who were very helpful in many aspects of this work. Finally, the weekly discussion and questioning by my friends and colleagues in the PFTL was very important in the maturation of this research. I am grateful to my PFTL contemporaries, Dr. Martin C. Marinack, Jr., Patrick Dougherty, Gagan Srivastava, Jonatan Sierra, Randy Pudjoprawoto, Kristin Warren, and Dr. John Shelton for their input, suggestions, advice, and camaraderie.

Partial funding for this research was provided by the National Science Foundation under the CAREER Award of Dr. C. Fred Higgs III (award #0645124), the Alfred P. Sloan foundation, the National Aeronautics and Space Administration (NASA) through the Graduate Student Researchers Program (GSRP) (grant# NNX09AK96H) and General Motors. This work also used the Extreme Science and Engineering Discovery Environment (XSEDE), which is supported by National Science Foundation grant number TG-MSS120003. The author of this work is greatly appreciative of this support

and the opportunity that it has provided to contribute to the body of knowledge surrounding multiphase flow science.

Table of Contents

| | |
|--|-----------|
| Abstract | iv |
| Acknowledgments | vi |
| Table of Contents | ix |
| 1.0 Introduction and Background | 1 |
| 1.1 Defining Tribology and Its Importance | |
| 1.2 Particle Flows and Tribology | |
| 1.3 Slurry Tribology | |
| 1.4 Traditional Multiphase Modeling Approaches | |
| 1.5 The Case for Eulerian-Lagrangian Modeling of Multiphase Tribological Phenomena | |
| 2.0 Eulerian Phase Modeling | 19 |
| 2.1 Discretization of the Eulerian Phase | |
| 2.2 The Eulerian Phase Time Step: The Courant-Friedrichs-Lewy (CFL) Condition | |
| 2.3 Eulerian Phase Case Studies | |
| 3.0 Lagrangian Phase Modeling | 31 |
| 3.1 Collision Detection | |
| 4.0 Phase Interactions | 35 |
| 4.1 Particle-Particle Coupling | |
| 4.2 Particle-Fluid Coupling | |
| 4.3 Particle-on-Fluid Forces | |
| 4.5 Surface-Fluid Coupling | |
| 4.4 Particle-Surface Coupling | |

| | |
|---|------------|
| 5.0 Implementation | 62 |
| 5.1 Code Organization | |
| 5.2 Parallelization | |
| 5.3 Pre-Processing | |
| 5.4 Post-Processing | |
| 5.5 Importing Objects from Solidworks™ | |
| 6.0 Erosive Wear Experimentation and Modeling | 70 |
| 6.1 Lunar Dust Erosive Wear Studies | |
| 6.2 Erosive Wear Experimental Methodology and Materials | |
| 6.3 Erosive Wear Experimental Results and Discussion | |
| 6.4 Erosive Wear Modeling | |
| 7.0 Rotary Rock Drilling Modeling | 90 |
| 7.1 Introduction to Rotary Drilling | |
| 7.2 Rotary Drilling Modeling Methodology | |
| 7.3 Modeling the Drill Bit | |
| 7.4 Modeling the Drilling Fluid | |
| 7.5 Modeling the Rock-Fluid Interaction | |
| 7.6 Units and Normalization | |
| 7.7 Rotary Rock Drilling Results and Discussion | |
| 8.0 Conclusions and Future work | 126 |
| 8.1 Conclusion and Future Erosive Wear Modeling | |
| 8.2 Conclusion and Future Work Rotary Rock Drilling | |
| 9.0 Appendix | 131 |
| References | 202 |

List of Figures

| | | |
|------------|--|----|
| Figure 1.1 | Chemical mechanical polishing (CMP) components | 8 |
| Figure 1.2 | The Eulerian-Eulerian vs. Eulerian Lagrangian modeling approach. | 18 |
| Figure 2.1 | Boundary conditions on the lid-driven cavity used to compare the finite-difference and finite-volume codes generated in this work. The dashed lined is the location for which the velocity was plotted in Fig. 2.2 and Fig. 2.3. | 21 |
| Figure 2.2 | A comparison of the finite difference (FD) and finite volume (FV) codes developed in this work at a Reynolds number of 100. | 22 |
| Figure 2.3 | A comparison of the finite-difference (FD) and finite-volume (FV) codes developed in this work at a Reynolds number of 1000. | 22 |
| Figure 2.4 | Qualitative comparison of the finite-volume (FV) and finite-difference (FD) codes developed in this work at a Reynolds number of 1000. (a) finite volume solution (b) finite difference solution | 23 |
| Figure 2.5 | Location of solution for velocity components and pressure in the computational cell of the staggered grid. Note, the velocity of the vector component w is not shown but it is also solved. | 24 |
| Figure 2.6 | Image of computational cells in CFD validation cases | 26 |
| Figure 2.7 | Spatial validation of the Eulerian solver (a) contour of fluid velocity (b) plot of velocity magnitude across length of channel. | 27 |
| Figure 2.8 | Temporal validation of the Eulerian solver (a) contour of fluid velocity (b) plot of velocity magnitude across length of channel at different times. | 29 |
| Figure 3.1 | The spring-dashpot model used in DEM particle collisions | 32 |
| Figure 4.1 | DEM study to validate the effects of COR on the modeling framework | 36 |
| Figure 4.2 | Results from DEM COR verification (a) Typical velocity | 37 |

| | | |
|-------------|---|----|
| | profile of the top particle during the test (b) The COR results from the framework for varying input velocities | |
| Figure 4.3 | Images of particles in contact used for a comparison with the LIGGGHTS modeling framework. | 40 |
| Figure 4.4 | A comparison of the Eulerian-Lagrangian model (E-L_MODEL) and LIGGGHTS (a) Prediction of particle temperatures (b) Percent difference in prediction | 41 |
| Figure 4.5 | Images of the particles for testing heat transfer with many contacts (a) two-dimensional array of particles (b) three-dimensional array of particles | 43 |
| Figure 4.6 | Quantitative comparison of particle temperatures (a) two-dimensional array of particles (b) three-dimensional array of particles | 45 |
| Figure 4.7 | A shear cell developed to validate the particle-fluid coupling – images provided from Marinack, Mpagazehe, and Higgs 2012 [40]. (a) The shear cell domain (b) Results comparing the particle velocity vs. the position in the cell. | 48 |
| Figure 4.8 | Images of the three-dimensional filtration simulation at different times (a) t=1 second (b) t = 2.5 seconds (c) t = 5 seconds | 51 |
| Figure 4.9 | Comparison of analytical equation and the computational framework in the prediction of the pressure drop across the particle bed. | 52 |
| Figure 4.10 | Particles trapped between two contacting surfaces voxelized surfaces. | 54 |
| Figure 4.11 | Computational mesh used to study flow around a cylinder (a) the current Eulerian-Lagrangian modeling framework (b) OpenFOAM | 56 |
| Figure 4.12 | Velocity magnitude around the cylinder as predicted by computational fluid dynamics (a) the current Eulerian-Lagrangian modeling framework (b) OpenFOAM | 58 |
| Figure 4.13 | A comparison of the current Eulerian-Lagrangian framework to experiments and OpenFOAM. | 60 |
| Figure 4.14 | A comparison of the current Eulerian-Lagrangian | 61 |

framework to experiments and OpenFOAM.

| | | |
|------------|---|----|
| Figure 5.1 | The primary directories in the framework | 63 |
| Figure 5.2 | Organization of files in the CFD sub-directory | 64 |
| Figure 5.3 | Decreased computational time as a result of parallelization of the current framework | 66 |
| Figure 5.4 | An image generated in Paraview produced from the current framework showing the streamlines around an immersed particle. | 67 |
| Figure 5.5 | Importing Solidworks CAD models into the current framework. (a) an image of a drill bit in SolidWorks. (b) The same drill bit post-processed in Paraview after having been imported by the current framework. | 69 |
| Figure 6.1 | Images of the Dust Erosion Experiment Rig (DEER) (a) schematic diagram (b) actual test hardware | 74 |
| Figure 6.2 | Images of JSC-1AF at different magnifications (a) 500x magnification (b) 1100x magnification (c) 4500x magnification | 76 |
| Figure 6.3 | Image of the 1045 steel, 6061-T6 aluminum, and acrylic test specimens | 77 |
| Figure 6.4 | Image of the material specimens before and after testing. (a) fresh specimens (b) eroded specimens | 79 |
| Figure 6.5 | SEM of metallic pieces. (a) pre-erosion steel (b) post-erosion steel (c) detail of post-erosion steel (d) pre-erosion aluminum (e) post-erosion aluminum (f) detail of post-erosion aluminum. | 80 |
| Figure 6.6 | Volume removed from each material after being exposed to erosive wear by the JSC-1AF lunar dust simulant. | 81 |
| Figure 6.7 | Optical profilometry of wear scar on metal specimens (a) contour map of aluminum surface depth (b) profile across aluminum specimen (c) contour map of steel surface depth (d) profile across steel specimen | 82 |

| | | |
|--------------|--|-----|
| Figure 6.8 | Images of the DEER setup for different impact angles (a) normal impact angle (b) oblique impact angle | 83 |
| Figure 6.9 | Images of the test specimens post-erosion (a) 90° impact (b) 30° impact | 84 |
| Figure 6.10 | Parameters used to calculate the material removal per particle in the erosive wear formulation | 85 |
| Figure 6.11 | Image of the simulated particles striking the surface at a 30° impact angle | 85 |
| Figure 6.12 | Contour of wear scar generated from the computational framework (a) 90° impact angle (b) 30° impact angle | 86 |
| Figure 6.13 | CFD boundary conditions used in the erosive wear model | 87 |
| Figure 6.14 | A comparison of the model's prediction for erosive wear to the experiment | 88 |
| Figure 7.1 | The spring-dashpot model used in the discrete element method (DEM) for particle collisions along with the bond between particles used in the bonded-particle model (BPM). | 93 |
| Figure 7.2 | Particles in the simulation domain creating the rock formation. | 97 |
| Figure 7.3 | Drill bit particles compared to PDC drill bit (a) PDC drill bit [76] (<i>Copyright 2008, Society of Petroleum Engineers Inc. Reproduced with permission of SPE. Further reproduction prohibited without permission</i>) (b) Drill bit approximation using DEM particles. | 99 |
| Figure 7.4.1 | Snapshot of simulation at $t^* = 52.5$. (a) Trimetric view of simulation domain. (b) Cross-section view of simulation to show detail of rock cutting. (c) Graph of instantaneous drill bit height vs. time data. | 108 |
| Figure 7.4.2 | Snapshot of simulation at $t^* = 405$. (a) Trimetric view of simulation domain. (b) Cross-section view of simulation to show detail of rock cutting. (c) Graph of instantaneous | 109 |

drill bit height vs. time data.

| | | |
|--------------|---|-----|
| Figure 7.4.3 | Snapshot of simulation at $t^* = 1005$. (a) Trimetric view of simulation domain. (b) Cross-section view of simulation to show detail of rock cutting. (c) Graph of instantaneous drill bit height vs. time data. | 109 |
| Figure 7.5 | The drill bit height vs. time for various bond ultimate strengths, F_{ult} | 110 |
| Figure 7.6 | Comparison with experimental data for the effect of rock properties on rate-of-penetration (ROP) (a) results from the current model (b) results from drilling experiments reproduced from Howarth, 1987 [84] | 111 |
| Figure 7.7 | Comparison with experimental data for the effect of weight-on-bit (WOB) on rate-of-penetration (ROP) (a) results from the current model (b) field data from M.J. Fear, 1999 [85] | 112 |
| Figure 7.8 | Drill bit height vs. time displaying the effect of low weight-on-bit (WOB) | 113 |
| Figure 7.9 | (a) Rate-of-penetration (ROP*) vs. drilling fluid viscosity, η^* (b) For Comparison, field data on the HHP/SI reproduced from M.J. Fear, 1999 [85] | 114 |
| Figure 7.10 | The average number of rock cuttings leaving wellbore per unit time vs. viscosity | 117 |
| Figure 7.11 | (a) Rate-of-penetration (ROP*) vs. angular velocity, ω^* (b) For comparison, drilling test data from A.D. Black, 1986 [88] | 119 |
| Figure 7.12 | Fig. 7.12 Drill bit height vs. time displaying the effect of angular velocity | 120 |
| Figure 7.13 | (a) Drill bit height vs. time for weight-on-bit (WOB*) at 0.189 (b) Friction forces experienced by drill bit for WOB* at 0.189 | 122 |

(a) Drill bit height vs. time for weight-on-bit (WOB*) at 0.047 (b) Friction forces experienced by drill bit for WOB* at 0.047 (c) Detail view of drill bit height with the friction forces superimposed.

Nomenclature

| | |
|--------------|---|
| C_p | Specific heat of particles |
| f | Body force |
| F_{ult} | Ultimate bond strength in bonded-particle model |
| K | Thermal conductivity of particles |
| K_{bond} | Bond stiffness in bonded-particle model |
| K_{spring} | Spring stiffness in discrete element model |
| m | Mass |
| Re | Reynolds number |
| ROP | Rate-of-Penetration |
| U_{spring} | Spring extension in bonded-particle model |
| WOB | Weight-on-Bit |

Greek Symbols

| | |
|-------------------|---|
| $\beta_{dashpot}$ | Damping parameter in discrete element model |
| ε | Void-fraction of particle-fluid suspension |
| η | Fluid viscosity |
| ρ | Density |
| σ | Stress tensor |
| ω | Angular velocity of bit |

Chapter 1

Introduction and Background

In this chapter, tribology is introduced and the relation of particle flow to tribology is covered. The case for modeling particle flow and tribological phenomena is outlined. An overview of traditional modeling techniques for these applications is provided. Finally, the case for using an Eulerian-Lagrangian approach to model particle flow and tribological phenomena is made. Portions of the text contained in this introduction and background are under review for publication as a book chapter.

1.1 Defining Tribology and Its Importance

Tribology, from the Greek *Tribo* meaning to rub, is the science and technology of interacting surfaces in relative motion and the related subjects of friction, lubrication and wear [1]. Tribological interactions dictate much of how humans interact with the world. Without friction between our feet and the ground, walking, running, or almost all other forms of human locomotion, would be significantly more challenging. ***Friction*** is a force a body experiences when in contact with, and moving at a relative velocity to, another body. It is what holds the small knots together that keep our shoe laces tied and the large knots together that keep massive ships moored at the dock. Without friction between a car's tires and the road, a car would not be able to accelerate or turn. Almost more alarming, if a car were to attain some velocity from another force, without friction, it

would not be able to stop. This fact has been observed by anyone who has witnessed a vehicle skid on ice, hydroplane on water, or slide on sand. In these cases, lubrication is at work. **Lubrication** is the process of accommodating velocity between surfaces moving in relative motion. Just as friction is a critical aspect of our lives, without lubrication, many of the machines and devices we use would not function. The most straight-forward example of lubrication's importance is the industry that has formed around motor oils and greases which reduce friction in internal combustion engines. However, one does not need to travel that far to observe interesting lubrication phenomena. Like other machinery, the human body has lubrication systems to prevent unwanted friction between moving interfaces. Notably, synovial fluid is produced to lubricate joints such as the knee and the hip. Lubricating these joints is by no means simple and some of tribology's most advanced theories of elasto-hydrodynamic lubrication with non-Newtonian fluids, particulate behavior, and biological films are used just to understand how these joints function [2-4]. Another, sometimes overlooked, instance of lubrication in the human body is the eye. Each time we blink our eyes, our eye lids glide on a thin fluid lubricating film of tears [5, 6]. Even our ability to consume food would be impaired if it were not for the lubrication provided by saliva [7]. However, the study of tribology does not only pertain to work; it pertains to fun as well. The lubrication of interfaces is the fundamental component to many of our most-enjoyed sporting activities. In fact, all of the events of the Winter Olympics – Skating (e.g., Figure, Speed, Short Track), Skiing (e.g., Snowboard, Ski Jumping, Alpine, Freestyle, Nordic Combined, Cross Country), Biathlon, Curling, Bobsleigh (e.g., Bobsleigh, Bobsleigh Skeleton), Luge, and Ice Hockey – are almost entirely based on phenomena that are only possible due to lubrication between

surfaces moving in relative motion. Kids enjoy tribology as well. If given the choice between a typical slide and a water slide, I suspect that most children, who correlate fun with sliding speed, would choose the water slide even without doing any complicated fluid dynamic analysis on the load-carrying capacity of the lubricating water film which creates this benefit.

The introduction of tribology would be incomplete without discussing wear. ***Wear*** is the removal of material from a surface as a result of its motion relative to other surfaces. In the battle between friction and lubrication, wear can often be a means of assessing which side is winning. Though it is straight-forward to envision scenarios in which wear is undesired (e.g., the scratching of eye glasses lenses, wearing of tires on a vehicle, the wearing of bearings in a wind turbine) wear can sometimes be desired (e.g., machining a piece of aluminum, polishing a silicon wafer, drilling into shale). There are several different types of wear, both mechanical (e.g. abrasion, erosion, and adhesion) and non-mechanical (e.g. corrosion), which are well-summarized in tribological texts [1]. However, it is sufficient to say that the mechanisms of wear in complex systems (e.g., chemical mechanical polishing (CMP)), the prediction of wear, and its abatement are some of the most intriguing and still-debated areas of tribology [8].

Though interesting as a topic of fundamental research, tribological phenomena have a large and important economic impact on our society. In the famous 1966 report by Peter Jost, it was indicated that better tribological practices could save more than \$767 million dollars (non-adjusted) by reducing the amount of machine breakdowns, machine maintenance needed, lubricant needed, frictional energy dissipation, etc [1]. As a more recent, startling, and local indication of the importance of tribology in our society, it was

reported in 2012 by Fenske et al. that more energy is consumed by friction in our motor vehicles than is consumed to propel them forward [9]. In other words, more of the money that we pay for gasoline is used just to overcome friction in the vehicle than is used to get us to our destination. Fenske stated that friction in the piston rings/skirt, valve train, breakings, seals, transmission, and differential account for about 15% of the energy consumed by our vehicles. According to the U.S. Environmental Protection Agency (EPA), 135 billion gallons of gasoline were consumed in the year 2010 for transportation in vehicles such as passenger cars, trucks, and buses in the United States [10]. Using the data from Fenske et al. as representative for the year 2010, that means 20 billion gallons of gasoline were consumed by friction in 2010. Taking the current \$3.542 dollars/gallon nationwide average price of gasoline in April 2013 [11] to be representative of average fuel prices, means that \$72 billion dollars were spent on overcoming friction in motor vehicles. A mere 5% reduction in automobile friction, down to 14.25% from 15%, would result in approximately \$3.7 billion dollars of savings per year on gasoline in the U.S. Such figures are astounding, but they speak to the importance of tribology research in our society. This figure does not include the cost to society of having engine components fail due to bad lubrication practices, the cost of motor oil, the cost of worn tires, maintenance, and other tribological concerns associated with motor vehicles. It also does not include frictional wastes in other forms of transportation, such as aircraft and water vessels, nor does it include the vast potential for savings in other aspects of society.

Over the past 80 years, tribologists have made tremendous strides in understanding the surface phenomena which generate friction, lubrication, and wear. Tribologists have linked the theories of contact mechanics and fluid mechanics to

understand elasto-hydrodynamic lubrication [12]. Tribologists have developed lubricants that work in the heat, cold and vacuum of space [13]. Tribologists can even tune an interface to provide more friction or less friction as needed [14]. Though these are examples of success, there is still much work to be done. Friction, lubrication, and wear are surface phenomena that happen on scales at which tribologists have just recently developed the laboratory instruments to probe. The recent profusion of surface metrology tools such as optical and contact profilometers, infrared thermal imaging devices, nano-indentors, scanning electron microscopes (SEM) and computational tools such as computational fluid dynamics (CFD), finite element analysis (FEA), discrete element modeling (DEM), and molecular dynamics (MD) are helping tribologists develop new theories for unexplained tribological phenomena.

In this section, an introduction to tribology and its uses were provided. In the following sections, the topics of particle tribology, which are most relevant to this thesis, will be discussed. Specific examples of current areas of particle tribology are provided and an overview of modeling and experimental techniques used to interrogate them is introduced.

1.2 Particle Flows and Tribology

The overview of tribology in the previous section introduced its applications and provided a reason to study it. In this section a more detailed discussion is presented on tribological interfaces in practice. Specifically, understanding particle behavior is an important aspect of practical tribology. As will be discussed, particles can enter lubricants

due to wear processes, or they can be intentionally introduced to either encourage or discourage wear. Particles can also be used as “smart” switches to clog or unclog pores to control the flow of our lubricant.

Though the modeling framework described in this work is capable of modeling dry particle flows. It was developed with the intent to model particle-fluid systems. As such, the work described in this section of the thesis, and many others, will be focused on particle-fluid multiphase systems. However, the challenges that were overcome in producing a multiphase modeling framework in no way relegates the current modeling framework to study only multiphase problems as it is valid for modeling fluids (gases and liquids), particles, surfaces, and the interaction of all three.

Primarily, the modeling framework in this thesis was designed for a field of tribology called “slurry tribology”. This type of tribology is dominated by particle-fluid interactions that can cause friction, lubrication and wear. In the following sections, slurry tribology is introduced. Portions of this section are to appear in an edited book chapter on slurry tribology.

1.3 Slurry Tribology

“*Slurry tribology*” is the study of particle-fluid suspensions as they relate to friction, lubrication, and wear. In tribology, slurries are often used to remove materials from surfaces in a controlled manner [15-18]. However, often times, engineering solutions are sought to reduce the amount of material removed from surfaces due to

slurry wear mechanisms such as abrasion and erosion [19]. In other scenarios, slurries are formed by adding lubricious particulates to fluid lubricants can actually increase bearing life [13]. Though the behavior of a slurry in a tribological environment is complex, many people are already familiar with natural processes that are dominated by slurry tribology such as the erosion of river beds due to small rocks suspended in the flow.

In one of their most familiar tribological applications, slurries are used as lapping and polishing compounds for the preparation of test specimen surfaces. The micron and sub-micron sized particles used in these polishing applications are essential for achieving the desired surface finishes. Though there are many different particle types in slurries, a few of the most common ones used in slurry polishing are silica, alumina and synthetic diamond. The specific abrasive particle type is chosen based upon parameters such as the material being polished, the base fluid in which the particles are suspended, the polishing load and speed, and the desired surface finish. Typically, the smaller the particle size, the better the surface finish (i.e., lower surface roughness) as large particles may remove more material and produce unwanted scratches.

1.3.1 Slurry Tribology Applications

In this section, several important uses of slurry tribology in relation to nanofabrication, lubrication, and energy production are discussed.

Slurry Tribology in Nanofabrication

Over the last several decades, chemical mechanical polishing (CMP) has become a fundamental application of slurry tribology [20]. CMP is used to fabricate computer chips, or integrated circuits (ICs), because of its ability to planarize and polish the large wafers on which ICs are built. During CMP, the wafer is pressed into a soft rotating polishing pad. Between the pad and the wafer, a chemically-active slurry, containing abrasive nano-particles, is entrained. Though there is still discussion in the literature regarding the details of the wear mechanisms in CMP, it is generally accepted that the nano-particles in the slurry abrade the wafer to remove unwanted material from its surface. In Fig. 1.1, a schematic of the CMP process is provided.

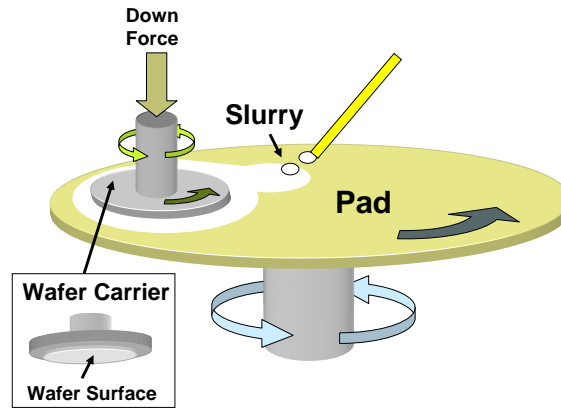


Fig. 1.1 Chemical mechanical polishing (CMP) components

Though widely used in the IC fabrication industry, improper CMP is known to impart defects on the IC's [17]. As the IC is built, nano-sized trenches are etched into the dielectric materials (mostly silicon dioxide) on the surface of the wafer. Conductive copper is deposited into these trenches to form copper lines which serve as the wires in the IC. To ensure that the trenches are filled, it is easier to deposit copper over the entire wafer and remove the excess material using CMP. Once much of the excess copper has

been removed, the resulting wafer surface is a heterogeneous combination of soft copper and hard dielectric materials. The difference in material properties between the copper and the dielectric can result in differential wear rates as CMP is performed. Two defects which occur during this CMP process are commonly known as “dishing”, which is unwanted material removal from the copper line, and “erosion”, which is unwanted material removal of the dielectric. Moreover, contact stresses and fluid pressures in the slurry can cause changes in material removal rates at the edge of the wafer. This unwanted material removal can result in electrical shorts or open circuits which may ultimately require the IC to be discarded. Understanding the mechanics of the slurry during CMP can lead to a reduction of such defects [20].

1.3.1.1 Slurry Tribology in Lubrication

Greases and oils provide essential lubricant films for machine components such as bearings, gears, chains, and seals. However, when tiny particulate matter is entrained into these lubricants, a slurry is formed which, in many cases, exacerbates wear and reduces the lifetime of the hardware [21]. Once the particles get into the interfacial film, they can disrupt the load-carrying capacity of the film and reduce the lubricant’s effectiveness. If the particles are so large that they transmit load between the surfaces, stresses on the surfaces can result in unwanted wear.

There are several examples of this phenomenon. In the internal combustion engine, the air filter helps to prevent particulate matter from entering the engine. However, when sand or dirt particles in the air intake make it past the air filter, these

particles can enter the combustion cylinder and make their way into the lubricant system. Notably, they can become trapped in the lubricant film on the piston rings and cause abrasive wear damage to the cylinder walls [21]. In internal combustion engines, particulates are also generated as a result of the combustion process itself. Soot particles can be formed which affect the lubricant's performance. Finally, a third example is the generation of particulate matter due to wear debris. During startup and shut down, bearings are particularly vulnerable to wear as they transition into the boundary and mixed lubrication regimes. Once this happens, wear debris can be introduced into the lubrication system. Oil filters in engines are used to help remove particulate debris from the lubricant to minimize the effect of these wear particles.

Artificial joints. Another example of slurry formation in lubricants occurs in the human body. When hip and knee replacements are performed, cements, such as polymethyl methacrylate (PMMA) are used to bind materials together. Overtime, the PMMA can chip generating sharp fragments which make their way into the synovial fluid forming a slurry. This slurry of synovial fluid and PMMA fragments can be detrimental to joints and cause unwanted wear to them [22].

Particle additives. It should be noted that not all slurries are detrimental to lubricated interfaces. Particle additives such as polytetrafluoroethylene (PTFE) and molybdenum disulfide (MoS_2) have been discussed in the literature for years. Some studies indicate that the effect of such additives may increase bearing performance [23] and this practice has been adopted commercially. There is however, a balance between

particulate additives acting to increase the bearing performance and the potential for them to clog the interface reducing the entrainment of lubricant into the bearing. That has led to the emerging and exciting new field of nano-fluid slurry lubricants. Nano-fluid slurry lubricants are fluid lubricants to which nano-particles have been added. The particles in nano-fluid slurries may be large enough to help lubricate the interface during boundary and mixed lubrication, but small enough to reduce the potential for clogging [13, 24]. Additionally, because of their fine size, nano-particles may form a more uniform protective layer on the surfaces as compared to larger micron-sized particle [25].

There have been several studies which have investigated the use of nano-particles as lubricant additives which show great promise in improving bearing performance. In a recent work, boric acid particles were added to environmentally-friendly lubricants, such as canola oil, and displayed a reduction in friction [24].

As a final example of the potential benefits of particles in lubricants, there is a class of bearings called “two-phase porous” bearings which rely on the presence of particles, advected by the lubricant, to clog pores in the bearing surfaces reducing their porosity. Once the porosity of the bearing is reduced, sufficient film pressures are generated to carry the bearing loads [26].

1.3.1.2 Slurry Tribology in Energy Production

Slurry tribology is an important component in energy production. There are several examples of the role of slurry tribology in the petroleum industry. Petroleum and

natural gas reserves are found deep under the Earth's surface. When drilling for these fuel reserves, it is common to use a slurry to lubricate the drill bit as it cuts into the rock formation [27]. This slurry, called a drilling fluid (often referred to as a drilling "mud" in the field), is an important component in the drilling process. The drilling fluid (1) lubricates the drill bit, (2) removes heat from the rock-drill bit interface, (3) transports rock cuttings away from the bit-rock interface, and (4) helps to prevent well blow-outs by keeping formation fluids from prematurely entering the well bore.

Typically, the drilling fluid slurry is either oil-based or water-based and contains particles such as calcium carbonate. By adjusting the concentration of particles and the particle type, the drill operator or "mud engineer" responsible for the drilling fluid can "tune" the drilling fluid's properties to better perform its tasks.

A closely related application of slurry tribology is a process called hydraulic fracturing. During hydraulic fracturing (often called "fracking"), fracturing fluid is pumped into fissures and cracks in the rock formation. The pressure of the fracturing fluid is so large, that it exerts enough force on the rock formation to fracture it and release pockets of gas that had been trapped within the rock. Much like drilling fluid slurries, fracking fluid slurries are comprised of a base fluid and loaded with particulates to enhance their performance.

Finally, after the petroleum fluids have been taken from the ground, sand and dirt in raw petroleum fluids create a slurry which can cause erosive wear to pipe surfaces as it is being transported long distances to refineries. This erosion is particularly severe at areas where the fluid changes directions or velocities sharply such as pipe elbows, tees and valves [19].

1.4 Traditional Multiphase Modeling Approaches

In the previous section, many interesting applications of slurry tribology were discussed. By modeling the behavior of slurry in those tribo-systems, it is possible to predict their tribological behavior prior to their implementation. As a result, money and time can be saved by having a “virtual laboratory” in which the effect of design and/or operational parameters on slurry behavior can be simulated. In this section approaches to model such multiphase particle-fluid (slurry systems) are detailed.

The basis of deterministic computational modeling is in choosing whether a medium can be modeled as (1) a continuum about which field data such as velocity is solved or (2) a collection of discrete entities which move in time and space representing the field’s characteristics. This choice is the primary distinction between Eulerian vs. Lagrangian modeling and has many consequences in the needed computational resources and the solution that is provided by the model. In this section, a discussion about modeling particle-fluid systems using Eulerian-Eulerian and Eulerian-Lagrangian approaches is presented. An argument is made that Eulerian-Lagrangian modeling is suitable to capture the primary physics involved in multiphase tribology.

1.4.1 Eulerian-Eulerian Methods

Eulerian methods assume the medium being modeled is a continuum and map the solution to a system of equations onto the space in which the medium resides. It is best explained by using the example of the lubricant inside of a bearing. This lubricant is

comprised of billions of atoms which are interacting with each other, the bodies (surfaces) of the bearing, and any other media such as air to which the lubricant may be exposed. If there are “enough” atoms in a given space (“enough” can be checked by comparing the mean free path to the characteristic length of the space), the behavior of this medium can be described as the combined behavior of all of these atoms. When this is done, the concept of stress and deformation can be applied to the medium as if it were one continuous unit – a continuum. Conservation of momentum can be applied to the continuum in the form of the Cauchy equation.

$$\rho \frac{DV}{DT} = \nabla \cdot \sigma + f \quad (\text{Eq. 1.1})$$

It is important to note that this equation is general, can be applied to liquids, solids, gases, and forms the foundation for Eulerian computational modeling such as CFD and finite element modeling (FEM). If it is assumed that a Newtonian fluid is the medium, constitutive relations for shear stress and velocity gradient can be applied to Eq. 1.1, conservation of mass can be included, and the Navier-Stokes equations emerge (Eq. 2.1, Eq.2.2).

If more than one phase is desired to be studied, such as a gas phase and a liquid phase, two liquids, or a fluid and a solid as is more relevant to this work, constitutive relations can be created for each phase and they can be solved together. It should be noted, that a unique equation for each phase is required and they are able to interact with each other through the source terms found in Eq. 1.1.

Thus, this outlines the Eulerian-Eulerian approach as the mathematics which describe two interpenetrating continua used to predict the behavior of two different phases.

1.5.5 Lagrangian Methods

The Lagrangian approach for modeling matter differs from the Eulerian approach in that the translation of the body in space and time are calculated, at least initially, instead of the internal stresses and deformations. A common choice using the Lagrangian method is to discretize at the size of the atoms themselves and impart physics-based “rules” on them (such as the Lennard-Jones potential) which dictate the forces on each atom. This choice has led to the field of molecular dynamics (MD) which has been highly successful in elucidating behavior of tribological interactions [28]. However, discretizing at the level of the atoms is not the only method and other choices can be made such as is the case with smoothed-particle hydrodynamics (SPH) [29]. Instead of applying the Cauchy equation, Newton’s second law (Eq. 1.2) is applied to the particles.

$$\mathbf{F} = m\ddot{\mathbf{x}} \quad \text{Eq.1.2}$$

In this way, the position of the discretized unit can be obtained by twice integrating the acceleration over time.

1.5.6 Eulerian-Lagrangian Methods

Eulerian-Lagrangian methods combine the Eulerian approach to model one phase and the Lagrangian approach to model another. For instance, if one were modeling a particle suspension [30, 31], it would be typical to model the suspending fluid with the Eulerian approach and the particles with the Lagrangian approach for reasons that will be discussed in the next section.

1.5 The Case for Eulerian-Lagrangian Modeling of Multiphase Tribological Phenomena

It is clear that there are substantial differences between Eulerian-Eulerian methods and Eulerian-Lagrangian methods. In this section some of the advantages and disadvantages for each modeling approach for particle-laden flows are discussed and an argument is provided that the Eulerian-Lagrangian modeling framework in this thesis is a powerful approach for modeling various types of particle flow and tribological phenomena. It should be noted that mere particle tracking is not what is being connoted when discussing Lagrangian approaches. Though particle tracking is useful to understand where particles move in a fluid, a robust particle solver provides more insight into particle behavior.

The Eulerian-Lagrangian method is preferred over the Eulerian-Eulerian method when information about particle locations is needed. This advantage means that the mapping of a unique wear event from a single particle can be obtained using the Eulerian-Lagrangian method while it cannot be obtained using the Eulerian-Eulerian method. Also, because the locations of unique particles are known, the particles can be

bound to represent structures themselves. This is the case in the bonded-particle method (BPM) that will be described later in this thesis. By knowing the unique locations of particles, it becomes more straight-forward to test some of hypotheses regarding wear events. Also, knowing the unique locations of particles means that the model can be used to understand colloid science in a straight-forward manner, which is a challenge with Eulerian-Eulerian approaches. However, modeling media as discrete entities, poses significant challenges in the amount of information needed to represent enough entities to comprise any substance of interest. The information needed for such modeling, is usually manifested in how much computer RAM a simulation will occupy. Additionally, the time needed to process this information may be prohibitive. Thus, historically the primary detraction of using the Eulerian-Lagrangian approach has been the computational expense. The advent of massively-parallelized supercomputers along with open parallelization protocols have helped to alleviate this burden substantially. It is believed that as computer speed increases, the Eulerian-Lagrangian approach will prove to be the clear winner for modeling particle-flow and tribological problems where fidelity is desired. Moreover, there has been much work in producing faster algorithms for Eulerian-Lagrangian codes which will also make Eulerian-Lagrangian modeling more attractive [31]. The arguments made in this section are summarized in Fig. 1.2. There is also a list of a few commercial and open source codes which can be used for each application.

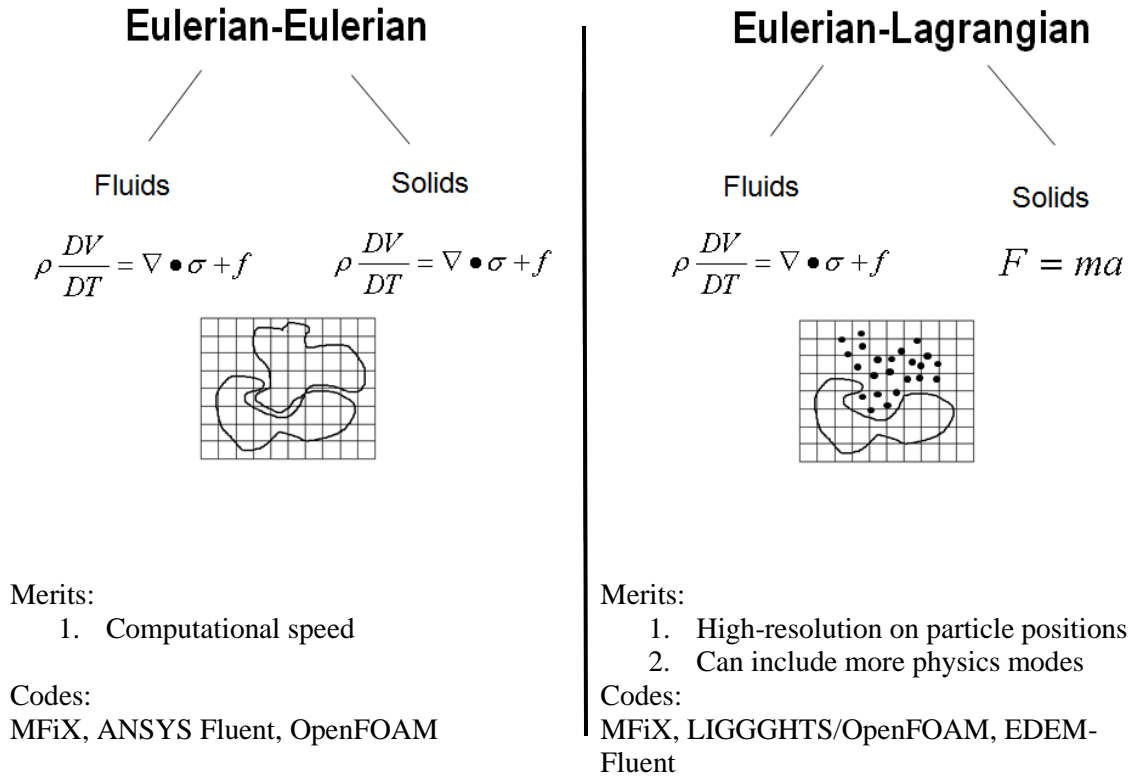


Fig. 1.2 The Eulerian-Eulerian vs. Eulerian Lagrangian modeling approach.

As such, this work seeks to provide a robust Eulerian-Lagrangian modeling framework which can serve as a foundation for modeling particle flows of a tribological nature. The Eulerian-Lagrangian framework was chosen because of its versatility and fidelity. By choosing this method, multiphase fluid-particle flows can be modeled to understand tribological phenomena. The work can also be extended to understand the behavior in biological and geological systems.

Chapter 2

Eulerian Phase Modeling

In this chapter, the methods used to model the Eulerian phase are described. A few case studies on the Eulerian phase are also provided. To model the Eulerian phase, an in-house computational fluid dynamics (CFD) code is developed. The Chorin projection method is used to numerically approximate the Navier-Stokes equations [32]. Beginning with the momentum equations, (2.1a), (2.1b), and (2.1c), an explicit Euler time-stepping algorithm is used to solve for the new velocity components, at each successive time-step. The variables u, v, w , and p represent the x, y, z components of the fluid velocity and the pressure, respectively.

$$\rho \left(\frac{\partial u}{\partial t} + u \frac{\partial u}{\partial x} + v \frac{\partial u}{\partial y} + w \frac{\partial u}{\partial z} \right) = -\frac{\partial p}{\partial x} + \eta \left(\frac{\partial^2 u}{\partial x^2} + \frac{\partial^2 u}{\partial y^2} + \frac{\partial^2 u}{\partial z^2} \right) + f_x \quad (2.1a)$$

$$\rho \left(\frac{\partial v}{\partial t} + u \frac{\partial v}{\partial x} + v \frac{\partial v}{\partial y} + w \frac{\partial v}{\partial z} \right) = -\frac{\partial p}{\partial y} + \eta \left(\frac{\partial^2 v}{\partial x^2} + \frac{\partial^2 v}{\partial y^2} + \frac{\partial^2 v}{\partial z^2} \right) + f_y \quad (2.1b)$$

$$\rho \left(\frac{\partial w}{\partial t} + u \frac{\partial w}{\partial x} + v \frac{\partial w}{\partial y} + w \frac{\partial w}{\partial z} \right) = -\frac{\partial p}{\partial z} + \eta \left(\frac{\partial^2 w}{\partial x^2} + \frac{\partial^2 w}{\partial y^2} + \frac{\partial^2 w}{\partial z^2} \right) + f_z \quad (2.1c)$$

$$\frac{\partial u}{\partial x} + \frac{\partial v}{\partial y} + \frac{\partial w}{\partial z} = 0 \quad (2.2)$$

Pressure-velocity coupling is achieved by satisfying the continuity equation (2.2).

2.1 Discretization of the Eulerian Phase

There are many different types of discretization used in computational fluid dynamics each with their own advantages and disadvantages.

In the finite difference method, the differential forms of the Navier-Stokes equations are discretized. This method is very common in fluid mechanics because of its accuracy on structured meshes. However, it fell out of practice in commercial codes largely due to challenges posed in modeling flow around general (non-Cartesian) geometries. This issue has been addressed elegantly with the immersed-boundary method which will be discussed later in this work. The finite volume method is widely used in CFD because of its ability to be implemented on unstructured, non-uniform meshes and its natural tendency to conserve mass. Though originally developed and widely used in computational solid mechanics, the finite element method has also been adapted to CFD [33]. The finite element method is appealing as this method has a very strong mathematical foundation. Also, once formulated, the finite element method can be extended to different shaped elements with little effort by changing the shape functions which represent the element. Moreover, finite elements give the user information about the flow field not only at the nodes but also at the flow within the element. Finally, spectral methods are used in CFD to obtain highly accurate solutions. In spectral methods Fourier transforms are used to approximate the solution of the Navier-Stokes equations by the sum of continuous equations.

In the initial stages of this work, much thought was given to the discretization technique as this choice would have consequences later in the modeling process. Both a finite volume and a finite difference CFD code were generated in the C++ computing language and compared to see which would be most suitable for this framework. Traditionally in CFD, the lid-driven cavity is used to evaluate solvers because the

solution of this configuration is highly dependent upon boundary conditions, convection, and diffusion. To model the lid-driven cavity, a no-slip, no flux boundary condition was applied to each boundary (Fig. 2.1).

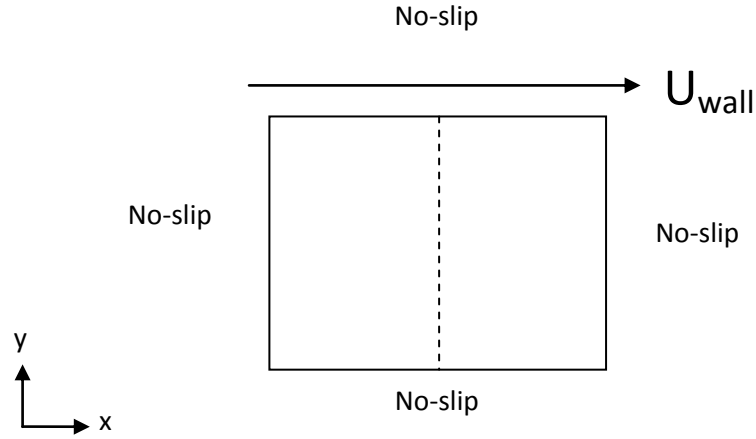


Fig. 2.1 Boundary conditions on the lid-driven cavity used to compare the finite difference and finite volume codes generated in this work. The dashed lined is the location for which the velocity was plotted in Fig. 2.2 and Fig. 2.3.

The top of the cavity was moved at a prescribed velocity, U_{wall} , to attain a prescribed Reynolds number given the density and viscosity of the fluid. In Fig. 2.2 a comparison of the finite volume method and the finite difference method solvers for a lid-driven cavity are provided for a Reynolds number of 100.

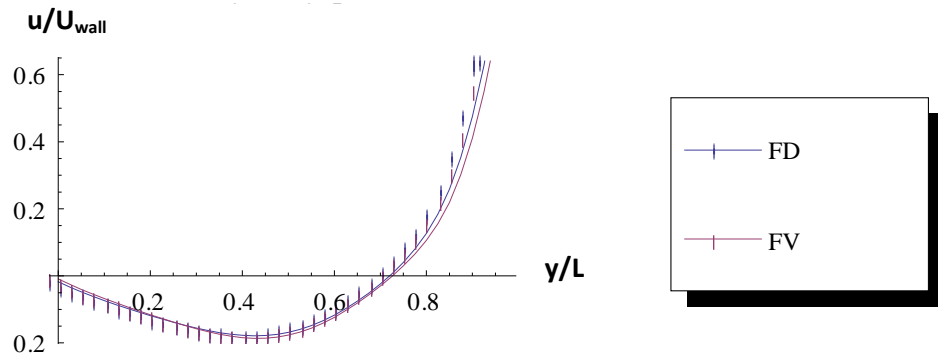


Fig. 2.2 a comparison of the finite difference (FD) and finite volume (FV) codes developed in this work at a Reynolds number of 100.

It can be seen in Fig. 2.2 that the results of the finite difference solver and the finite volume solver agree very well for a Reynolds number of 100. As a second test, the Reynolds number was increased to 1000 and the results are compared in Fig. 2.3.

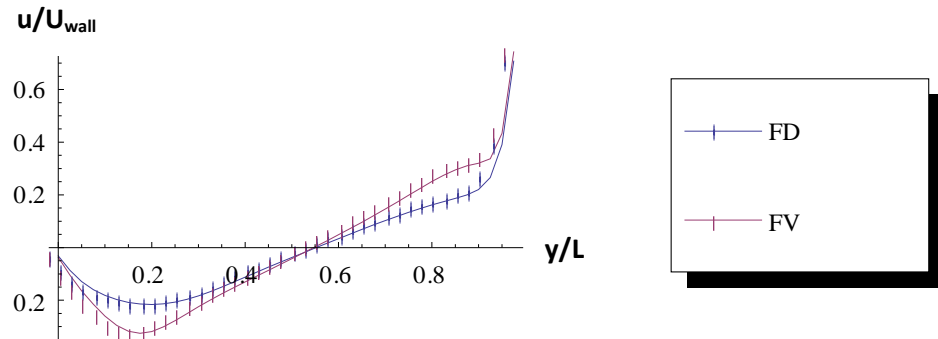


Fig. 2.3 a comparison of the finite difference (FD) and finite volume (FV) codes developed in this work at a Reynolds number of 1000.

At this larger Re, there is slightly less agreement between the two discretization techniques. However, both predict the same trends and the velocity vectors of the

solution (Fig. 2.4) display much qualitative agreement. It is believed that the subtle differences in the solution can be attributed to the differences in the discretization and smoothing techniques.

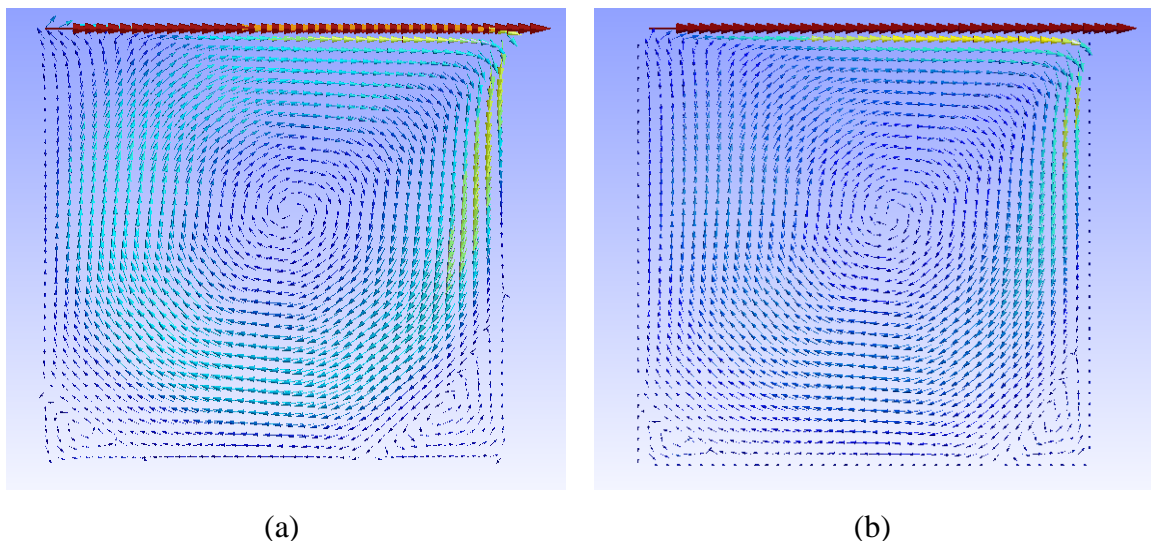


Fig. 2.4 Qualitative comparison of the finite volume (FV) and finite difference (FD) codes developed in this work at a Reynolds number of 1000. (a) finite volume solution (b) finite difference solution

Ultimately, the finite difference method was chosen to discretize the Navier-Stokes equations to model the Eulerian phase because of its prior success in modeling tribological applications [18, 34]. Some of the disadvantages of this method, such as the challenges associated with unstructured grids, were overcome by using the immersed boundary method. The details of the immersed boundary method will be discussed later in this work. However, this technique allows for the Eulerian phase to interact with items of a various shape. The donor-cell method was used and a blended first and second order derivative was used to discretize the spatial derivatives. The flow was solved on a

staggered grid with the u, v , and w velocity components being solved at the farthest respective x, y , and z boundary of each computational cell. The pressure was resolved at the center of each cell (Fig. 2.5).

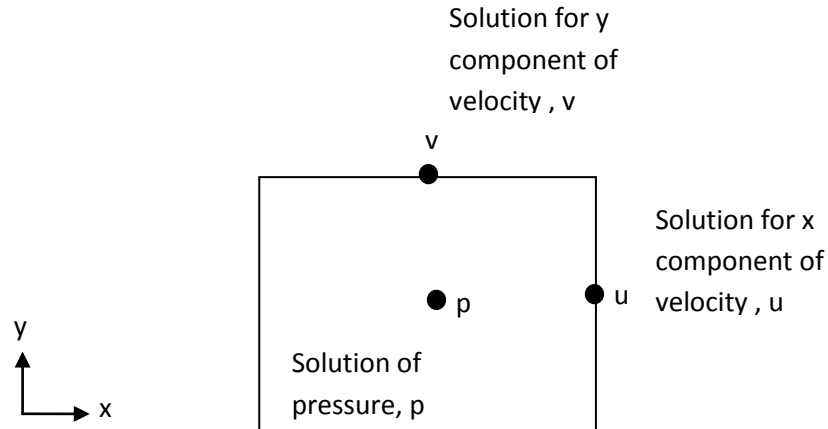


Fig. 2.5, Location of solution for velocity components and pressure in the computational cell of the staggered grid. Note, the velocity of the vector component w is not shown but it was also solved.

Temporally, a first-order Euler integration time-stepping algorithm was used which matches the time integration used in the Lagrangian portion of the model. The pressure solution was implicit while the velocity solution was explicit once a pressure field had been generated that satisfied continuity. The pressure at each time-step is solved through the successive over-relaxation (SOR) method.

2.2 The Eulerian Phase Time Step: The Courant-Friedrichs-Lewy (CFL) Condition

The Courant-Friedrichs-Lewy (CFL) condition is traditionally used to determine the maximum time-step for CFD solvers. This condition makes it such that the time-step is small enough to restrict information from propagating so fast that nodes, on which the solution is solved, go unrepresented (skipped). This was imposed by making sure that the time-step was less than the discretization length divided by the magnitude of the velocity in that direction (Eqn. 2.3) [35]. U_{max} , V_{max} , and W_{max} represent the maximum velocities in the three spatial directions.

$$\Delta t < \min\left(\frac{\Delta x}{|U_{max}|}, \frac{\Delta y}{|V_{max}|}, \frac{\Delta z}{|W_{max}|}\right) \quad \text{Eq. 2.3}$$

In practice, the Lagrangian phase also has limitations, which are usually stricter than the CFL condition in this case, and the minimum time-step may be dictated by that.

2.3 Eulerian Phase Case Studies

In this section, the results from several case studies using the Eulerian CFD code developed for this work are presented. In particular, the code is validated for its spatial accuracy and its temporal accuracy.

2.3.1 Spatial accuracy validation

To test the spatial accuracy of the CFD code, a Poiseuille flow was generated in a channel. The mesh was fairly course and consisted of $N_I = 80$, $N_J = 10$, and $N_K = 10$ nodes in the x,y, and z directions, respectively. The total dimensions of the mesh were 0.004 meters in the x direction and 0.0005 meters in y and the z direction. An image of the mesh is shown in the domain.

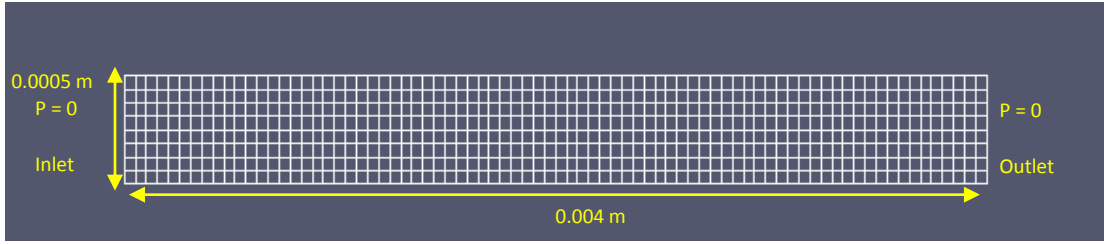


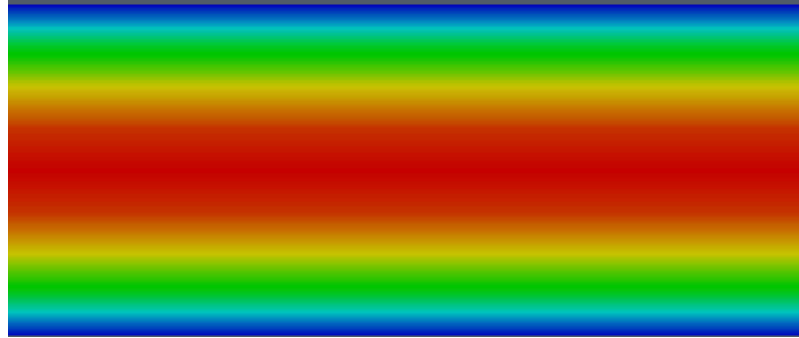
Fig. 2.6 Image of computational cells in CFD validation cases

The boundary conditions on the top and bottom of the domain were set to no slip, no flux. On the east and west sides an inlet/outlet boundary condition was defined.

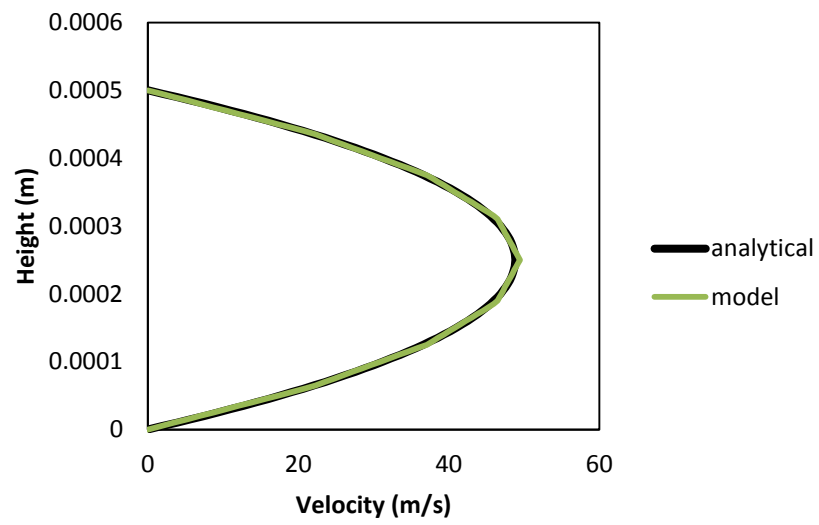
To validate the results from this configuration, the analytical solution of the Navier-Stokes equations for pressure driven channel flow with the same boundary conditions (Poiseuille flow) is also solved

$$u = -\frac{dp}{dx} \frac{h^2}{2\mu} \left(1 - \frac{y^2}{h^2} \right) \quad \text{Eq. 2.4}$$

In Fig. 2.7, a contour of the velocity magnitude and a quantitative comparison with Eq. 2.4 are displayed.



(a)



(b)

Fig. 2.7 Spatial validation of the Eulerian solver (a) contour of fluid velocity (b) plot of velocity magnitude across length of channel.

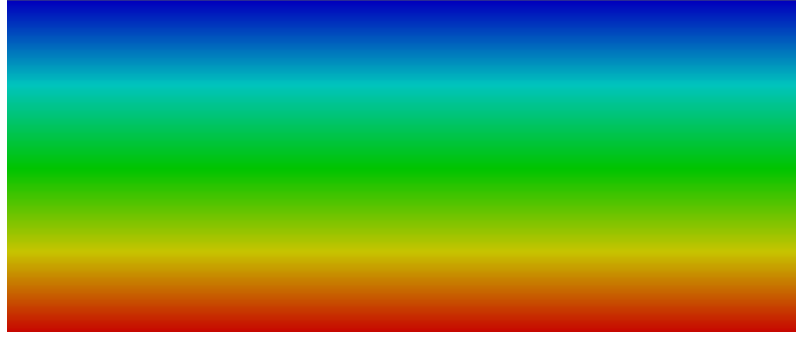
It can be seen in Fig. 2.7 that there is good spatial agreement between the solution produced from this framework and the analytical solution of the Navier-Stokes equations for channel flow.

2.3.1 Temporal accuracy validation

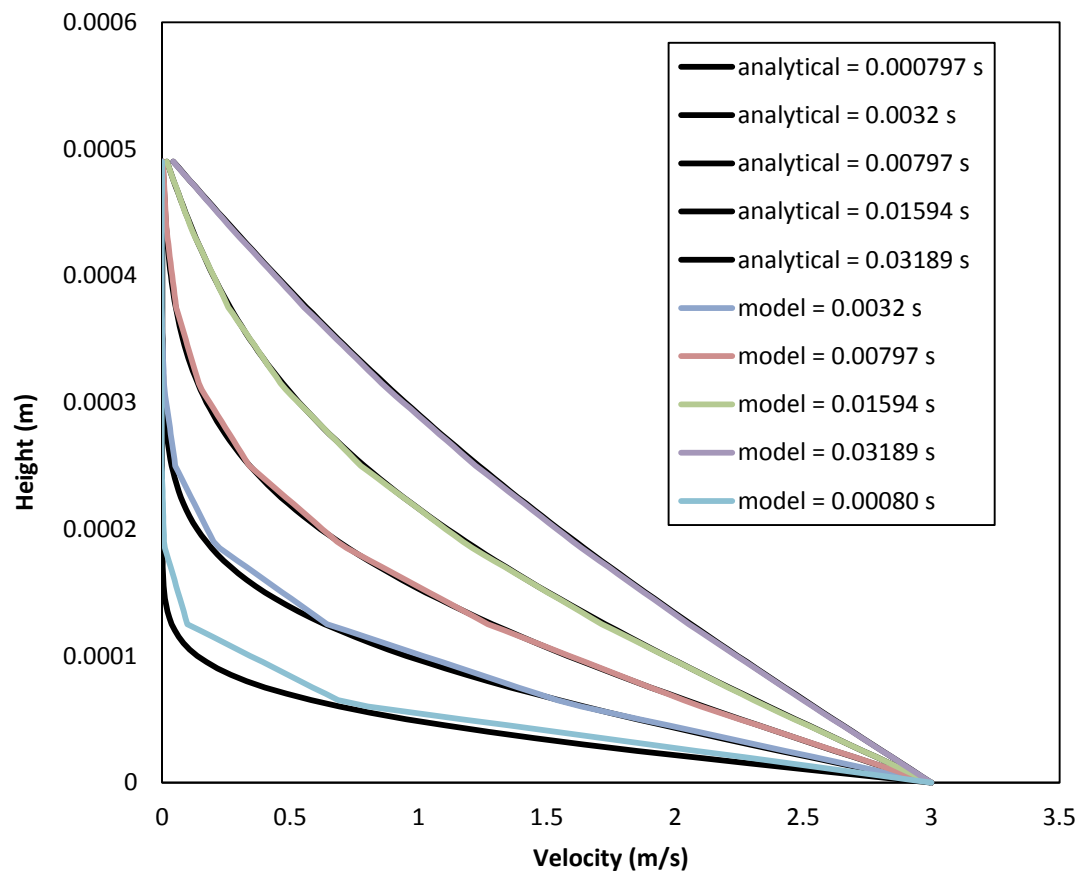
Next, the temporal accuracy of the current modeling framework was validated using the same computational setup. However, modifications were made such that the boundary conditions were set to be inlets and the pressure was set to zero gauge pressure on the east and west boundaries. Additionally, at time $t=0$ the bottom of the plate was prescribed a constant velocity of U_0 . The solution to this configuration was compared to the analytical solution for flow between plates with a suddenly-started boundary (Eq.2.5) [36].

$$\frac{u}{U_0} = \left(1 - \frac{y}{h}\right) - \frac{2}{\pi} \sum_{n=1}^{\infty} \frac{1}{n} \exp(-n^2 \pi^2 t^*) \sin \frac{n \pi y}{h} \quad \text{Eq. 2.5}$$

In Fig. 2.8, a contour plot of the fully developed flow field and a plot of the velocity at different times are provided.



(a)



(b)

Fig. 2.8 Temporal validation of the Eulerian solver (a) contour of fluid velocity (b) plot of velocity magnitude across length of channel at different times.

It can be seen in Fig. 2.8 that there is very good agreement between the analytical solution and the model as time progresses.

In this chapter, the computational fluid dynamics developed for this code was introduced. An explanation of the discretization technique and the staggered grid were described. Finally, the code was validated for its spatial and temporal accuracy by comparing it to analytical solutions of the Navier-Stokes equations.

Chapter 3

Lagrangian Phase Modeling

In this chapter, the methods used to model the Lagrangian phase are described.

A robust modeling technique is important for Eulerian-Lagrangian modeling of multiphase flows. The discrete element method (DEM) is used as the core particle model methodology for the applications described in this work. DEM is a Lagrangian technique in which the location of each particle is tracked. Its implementation is further described in the following text.

Traditionally, there are two different approaches to DEM modeling – hard-body and soft-body. The distinction between the two is primarily in how collisions are processed. In hard-body DEM, collisions between particles occur over one time-step and the conservation of kinetic energy and momentum (or a coefficient of restitution) are used to determine particle trajectories. In soft-body DEM, particle collisions generally occur over multiple simulation time-steps which allow for highly-refined physics to be applied during the collision of a particle with another particle or a surface. However, this advantage comes at a computational cost as hard-body DEM is generally more forgiving on the time-step considerations. Be that as it may, the soft-body DEM approach was chosen for this work as it is more suited for the high-resolution, physics-based particle-surface contact. Moreover, the soft-body DEM approach is better suited for multi-body collisions which increases the versatility of this code substantially.

In the soft-body discrete element method [37], the trajectory of each particle is determined by the cumulative effect of forces acting on it through Newton's second law of motion. Particles are influenced by their collisions with other particles, collisions with domain boundaries and other forces such as the drag of the fluid. The common spring-dashpot model, depicted in Fig. 3.1, is used to model particle-particle and particle-wall collisions.

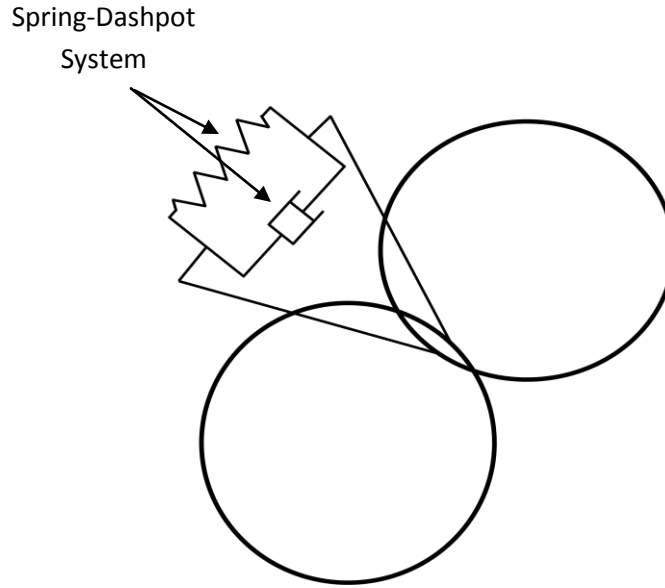


Fig. 3.1 The spring-dashpot model used in DEM particle collisions

Collisions occur when the distance between one particle and another particle or the domain boundary is less than one particle radius. The total force, $\mathbf{F}_{collision}$, imparted to a particle during a collision, described in Eq. 3.1 is a linear combination of two forces. The first is a repulsive force caused by the compression, \mathbf{U}_{spring} , of an idealized spring which occurs when the particles overlap. The second is a damping force proportional to the normal velocity, \mathbf{V}_n , between the particle and the object with which it is colliding. This damping force is introduced to capture the inelasticity of the collision.

$$\mathbf{F}_{collision} = K_{spring}\mathbf{U}_{spring} - \mathbf{V}_n\beta_{dashpot} \quad (\text{Eq. 3.1})$$

In Eq. 3.1 K_{spring} and $\beta_{dashpot}$, the spring and damping constants respectively, are specified depending on whether the collision is with other particles or with the boundaries. The numerical integration scheme used to update particle velocities and positions is the explicit Euler integration technique.

3.1 Collision Detection

The most computationally-expensive component in DEM is particle contact detection. The reason is that each particle must check with every other particle to determine if a collision is occurring. There are many algorithms which have been developed to increase the efficiency of particle detection in DEM. In this work, Verlet tables are employed to increase the computational efficiency of contact detection. With Verlet tables, each particle is given a list, or table, of particles with which it can collide at any given time-step. At a user defined interval, the Verlet table is updated. The kissing parameter of spherical particles describes the total number of non-deformed particles a single non-deformed particle can contact at any time. The kissing parameter for spherical particles is 12. Thus, a Verlet table of a length of 20 was chosen so that it would contain particles prior to contact. Though the Verlet table provides significant speed-ups in the solution, having to store more information per particle does affect the code's memory usage.

In this chapter, the discrete element method was introduced which is used to model the Lagrangian phase. This technique can be used to model tribological phenomena on its own and it can be used in conjunction with the Eulerian phase.

Chapter 4

Phase Interactions

In this chapter, the coupling between the Eulerian and Lagrangian phases is discussed. In the framework, there are four different types of phase interactions (1) particle-particle, (2) particle-fluid, (3) particle-surface, and (4) surface-fluid. There are several cases studies performed to test the performance of this coupling.

4.1 Particle-Particle Coupling

The primary particle-particle coupling employed pertains to particle collisions. This was thoroughly described Chapter 3 which discussed the development of the Lagrangian Phase. In this chapter, a case study is performed to test how physical concepts, such as the coefficient of restitution (COR) and heat transfer are incorporated into the model.

Coefficient of Restitution in Particle Collisions

The coefficient of restitution (COR) between two particles describes how elastic or inelastic the collision is between them. For a particle colliding with a stationary object, the COR can be calculated as a ratio of the pre-collision speed, V_2 , to the post-collision speed, V_1 , as defined by Eq. 4.1.

$$COR = \frac{V_2}{V_1} \quad (\text{Eq. 4.1})$$

A COR of 1 means that the collision is perfectly elastic. A COR of 0 means that the collisions is perfectly inelastic. The study of how COR affects the properties of particle

flows is an active area of research [38] and is important in characterizing the bulk behavior of granular flows. As such, the DEM modeling technique is well-suited to model this aspect of particle collisions. The damping parameter, β , can be solved with respect to the particle mass, m , and the spring constant, k and the COR. This relation is displayed in Eq. 4.2 [39].

$$\beta_n = \frac{-2\sqrt{mK_n \text{Log}(COR)}}{\sqrt{\pi^2 + \text{Log}(COR)^2}} \quad (\text{Eq. 4.2})$$

To verify the effects of COR on the DEM modeling framework, a series of computational drop tests were performed (Fig. 4.1). During these tests, one particle was held stationary preventing its motion from affecting the calculation. Another particle was initialized with a velocity toward the stationary particle. After the collision, the rebound velocity from the moving particle was output from the modeling framework. The COR was determined by observing the difference between pre- and post-collision velocities.

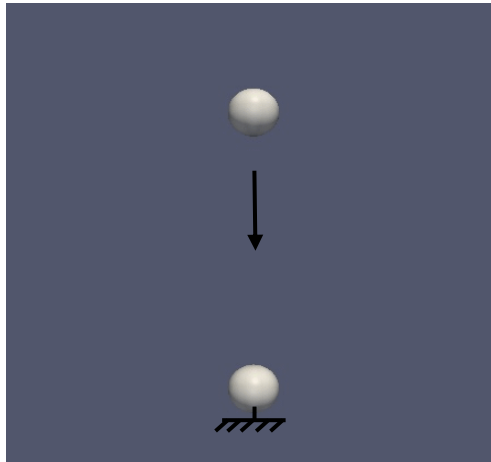


Fig 4.1. DEM study to validate the effects of COR on the modeling framework

The typical velocity profile from the drop tests can be seen in Fig. 4.2. Here it shows that the particle starts with a negative velocity as it enters the collision and has a positive velocity after the collision as expected. Also, in this figure the model's ability to predict COR based on collision velocity is presented. It is clear that the model does not display a dependence on the impact velocity however it is known that impact velocity can affect COR and such a modification can be incorporated into future versions of this code. Nevertheless, this study serves as a good verification of the COR input parameter for the framework. It should also be noted that although it appears from Fig. 4.2a that the change in particle velocity is nearly instantaneous, a few points on the graph show that the change in particle velocity does occur over time. As mentioned previously, this is one of the primary differences between the hard-body and soft-body approaches. This difference is particularly important for wear modeling in which the duration of particle surface collisions can affect the material removal.

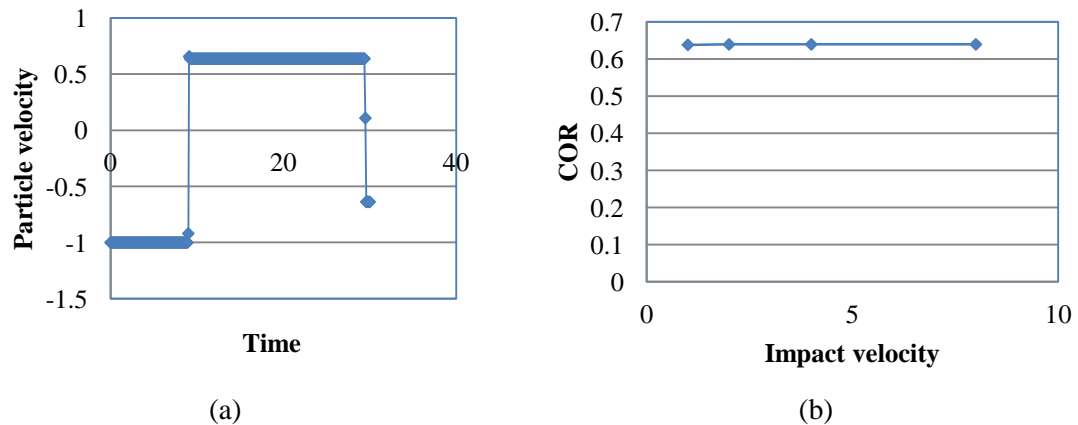


Fig 4.2 Results from DEM COR verification (a) Typical velocity profile of the top particle during the test (b) The COR results from the framework for varying input velocities

The framework's calculated COR was compared with the COR input in Eq. 4.2. From Table 4.1 it is apparent that there is very good agreement from this comparison. This study serves as a verification of the calculation of COR in the DEM modeling framework.

Table 4.1 The input COR compared to the framework's output COR

| Input COR | Output COR | % Error |
|------------------|-------------------|----------------|
| 1 | 1.000005 | 5E-06 |
| 0.8 | 0.80003375 | 4.22E-05 |
| 0.6 | 0.59974375 | 0.000427 |
| 0.4 | 0.3991975 | 0.002006 |
| 0.2 | 0.199545 | 0.002275 |
| 1.00E-06 | 4.91439E-05 | 48.14388 |

Heat Transfer between Particles

In this framework, the particles can also exchange heat with each other. This capability was incorporated so that the heat transfer studies between particles could be studied.

The heat equation (Eq. 4.3a) was applied on the particles in a similar manner to the computational framework LIGGGHTS. LIGGGHTS, which is LAMMPS Improved for General Granular and Granular Heat Transfer Simulations, is an open source computational model that was adapted from the MD framework, LAMMPS.

$$mc_p \frac{dT_{pi}}{dt} = \sum \dot{Q}_{pi-pj} + \dot{Q}_{pi} \quad \text{Eq. 4.3a}$$

$$\dot{Q}_{pi-pj} = \frac{4K_{pi}K_{pj}}{K_{pi} + K_{pj}} (A_{contact})^{0.5} \Delta T_{pi-pj} \quad \text{Eq. 4.3b}$$

Using this equation, discretizing the temporal component with finite differencing and then stepping forward in time with first-order Euler integration, it is possible to model heat transfer through particles as a function of time. To assess the functionality of this module, a case study was performed to test heat transfer with various collections of particles. The parameters used in this study are shown in Table 4.2.

Table 4.2. Parameters used in the particle-heat transfer simulations

| | |
|---|--------|
| radius (mm) | 0.5 |
| center-to-center distance (mm) | 0.9 |
| density (kg/m ³) | 7850 |
| thermal conductivity (W/(m K)) | 43 |
| specific heat (kJ/Kg-K) | 0.49 |
| temperature of hot particle (Kelvin) | 773.15 |
| temperature of other particles (Kelvin) | 273.15 |

In Fig. 4.3, an image is shown of five particles in contact. The color of the particles is contoured in accordance to their temperature.

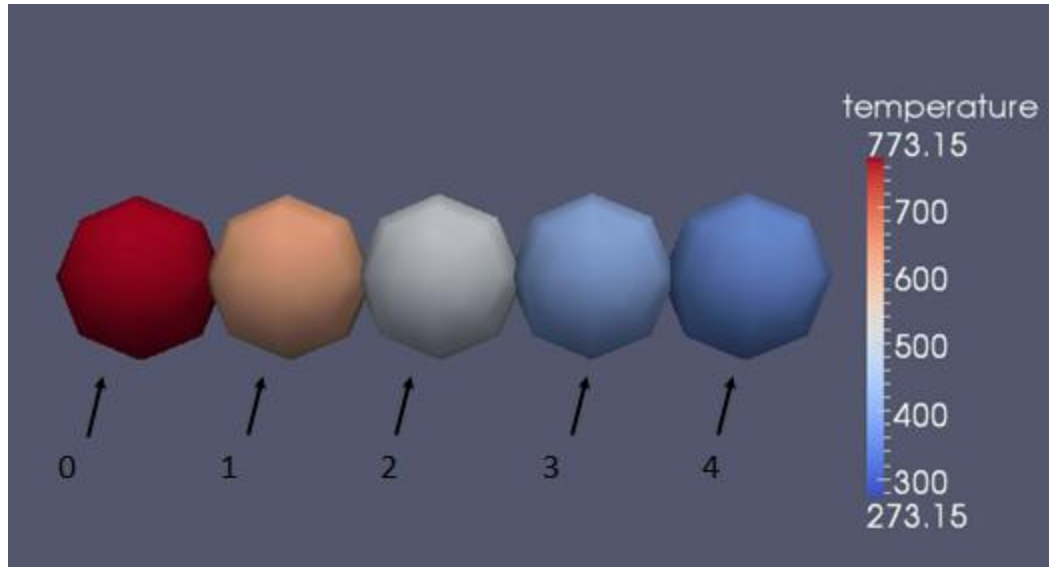
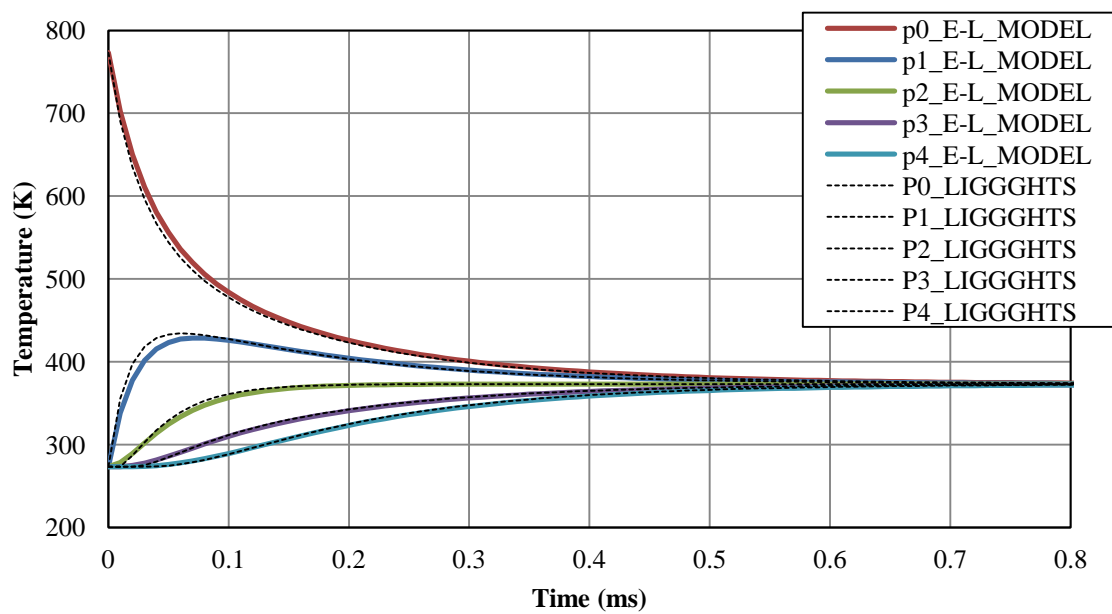
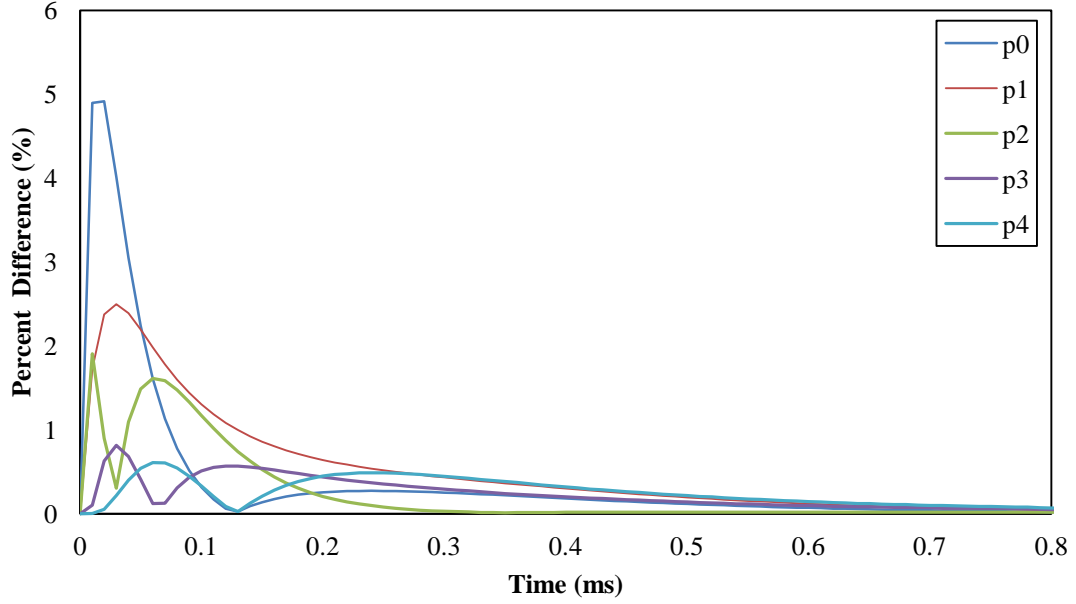


Fig. 4.3 Images of particles in contact used for a comparison with the LIGGGHTS modeling framework.

At the beginning of the simulation, one particle was set to 773.15 Kelvin. The other particles were initialized to 273.15 Kelvin. All of the particle temperatures were allowed to vary in accordance with Eq. 4.3. An identical configuration was generated in the LIGGGHTS software and transient behavior of the particle temperatures are displayed in Fig. 4.4.



(a)



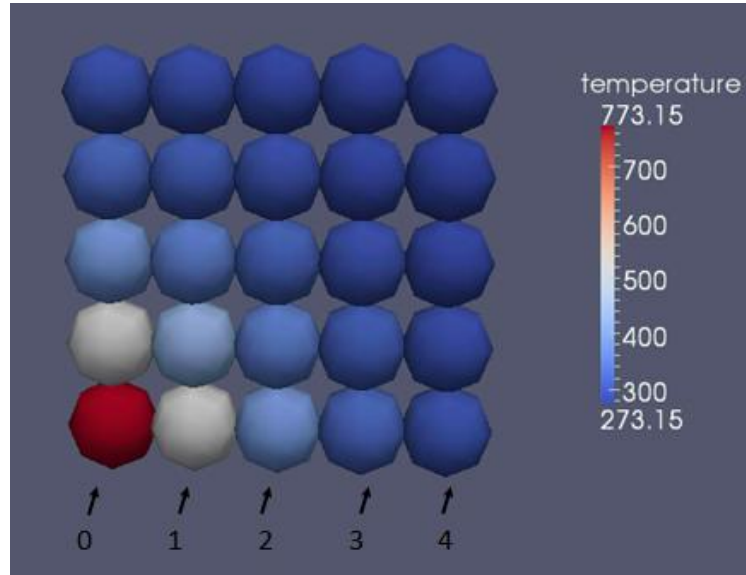
(b)

Fig. 4.4 A comparison of the Eulerian-Lagrangian model (E-L_MODEL) and LIGGGHTS (a) Prediction of particle temperatures (b) Percent difference in prediction

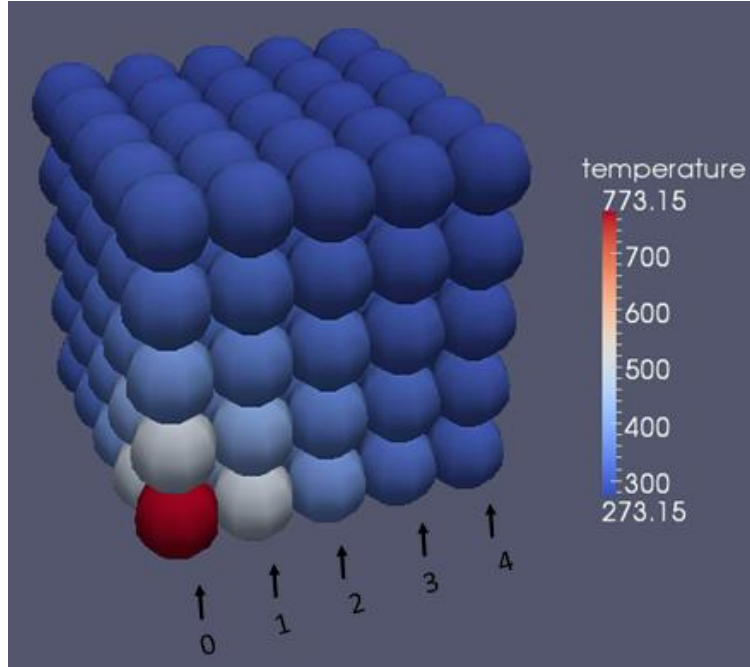
It can be seen in Fig. 4.4a that the temperature of the particles as a function of time as predicted by the current framework matches very closely to the predictions of the LIGGGHTS framework. In Fig. 4.4b, the percent difference between the two modeling frameworks is shown and it can be seen that the maximum difference is less than 5%. It is believed that this slight difference may be due to different time integration techniques between the frameworks. However, such excellent agreement serves as important verification of the current framework to predict heat transfer in particle-particle contacts.

In practice, particles in packed beds usually maintain contact with many particles with which they exchange heat. To ensure that heat transfer among particles with more

contacts than those shown in Fig. 4.5 could be solved in the current framework, another series of test cases was conducted with two-dimensional and three-dimensional particle arrays. At the beginning of these simulations, one particle was set to 773.15 Kelvin and this temperature was maintained for the duration of the simulations. The other particles were initialized at 273.15 Kelvin and their temperature was allowed to vary in accordance with Eq. 4.3.



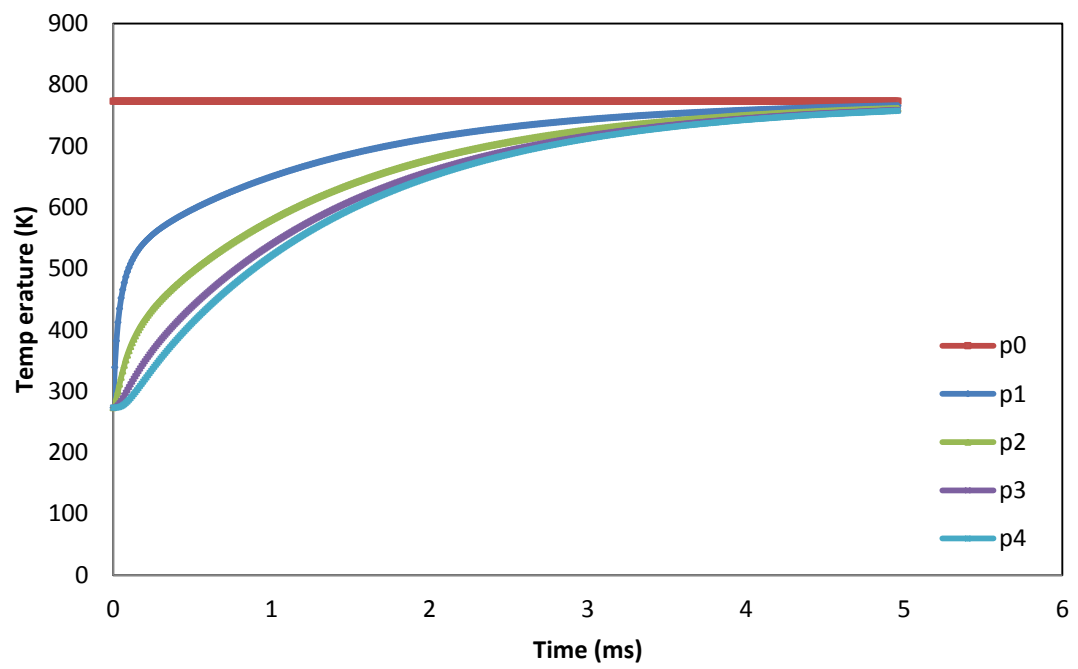
(a)



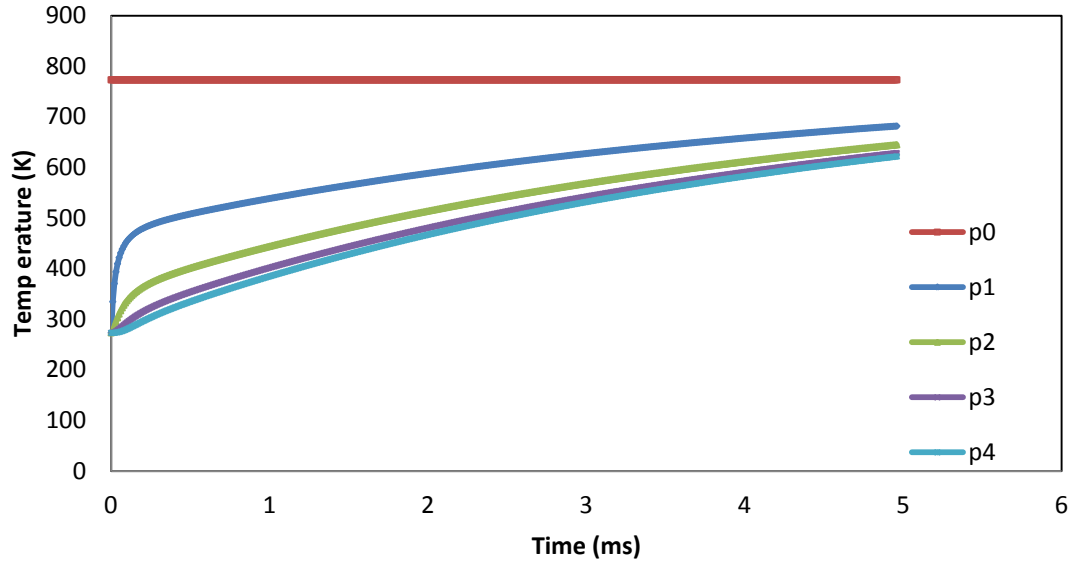
(b)

Fig. 4.5 Images of the particles for testing heat transfer with many contacts (a) two-dimensional array of particles (b) three-dimensional array of particles

In Fig. 4.5, it is clear that heat is transferred from the particle that is hot to the cooler particles. In Fig. 4.6, a quantitative comparison of particle temperatures vs. time is provided for 5 ms of simulation time. The particles plotted in Fig. 4.6 are labeled with arrows in Fig. 4.5.



(a)



(b)

Fig. 4.6 Quantitative comparison of particle temperatures (a) two-dimensional array of particles (b) three-dimensional array of particles

In Fig. 4.6, it can be seen that as the simulation progresses, the “cool” particles begin to approach the temperature of the “hot” particle as expected. Also, from the case where there are 25 particles (Fig. 4.6a) compared to the case where there are 125 particles (Fig. 4.6b) it can be seen that it takes significantly longer for the temperature of the particles to rise. This also agrees with intuition as the case with 125 particles has a larger thermal mass to which the heat of the “hot” particle must diffuse.

In this section, the particle-particle interactions were discussed as they relate to heat transfer. The results were verified by comparison with the LIGGGHTS computational framework. Additionally, heat transfer across particle beds with many contacts was investigated.

4.2 Particle-Fluid Coupling

The particle-fluid coupling is an essential component in this work. In many instances of tribological flows such as erosive wear, and chemical mechanical polishing (CMP) drag from the fluid is responsible for advecting particles. It is known that a particle inside of a fluid will experience various forces such as Saffman lift, Brownian, electro-static repulsion and van der Waals attraction forces from other particles. The framework is setup such that these forces can be added to the particles with little effort.

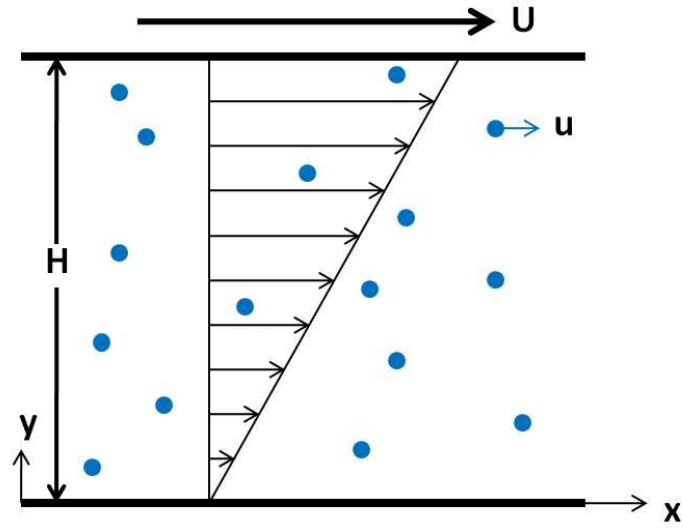
However, in the current deployment of the framework, only the drag force is calculated for the particle-fluid interaction. There are two methods of calculating drag. One method relies on Stokes drag and one method uses the Ergun equation. The difference between these two methods and their implementation is described below.

4.2.1 Fluid on Particle Stokes Drag

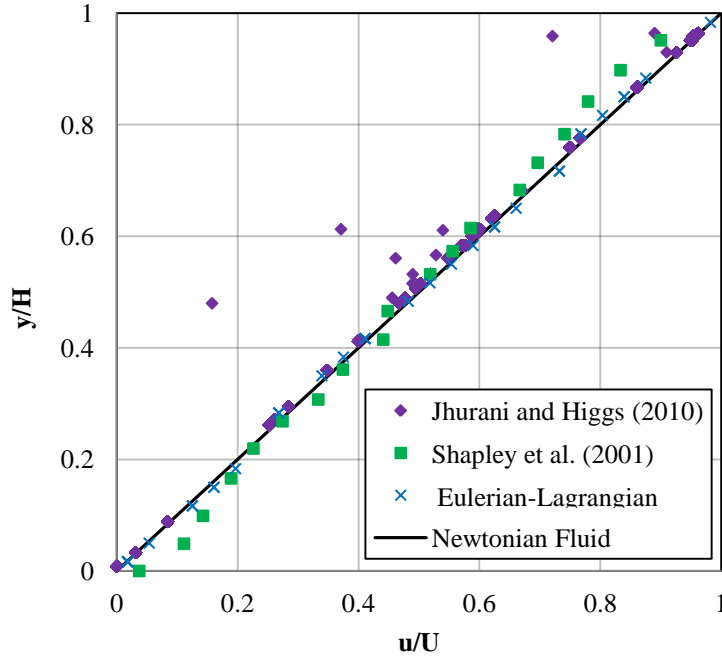
The first method used to calculate the drag on the particles is Stokes drag. Assuming spherical particles, a Stokes drag force is used to update particle velocities based on the fluid velocity field. Stokes drag is calculated from Eq.4.4 where $F_{drag,x}$, η , and r_p , represent the drag force in the x direction, the fluid viscosity, and the particle radius, respectively. The other variables: u_p , v_p , z , $u_{fluid}(x_p, y_p, z_p)$, define the particle velocity and the fluid velocity at the particle's center, (x_p, y_p, z_p) . Differences in the DEM particle positions and locations in the fluid mesh where a solution is obtained are accounted for by an averaging scheme to obtain the proper fluid velocity at the particle's center.

$$F_{drag,x} = 6\pi\eta r_p(u_{fluid}(x_p, y_p, z_p) - u_p) \quad (\text{Eq.4.4})$$

To validate this method, a shear cell was developed using the Eulerian phase. In this case, inlet-outlet boundary conditions were used on the left and right boundaries of the cell ($x = 0$ and $x = 1$) while the bottom and top of the cell ($y = 0$ and $y = H$) was set to a no slip, no flux boundary condition. The velocity at the top of the cell ($y = H$) was set to U .



(a)



(b)

Fig. 4.7 A shear cell developed to validate the particle-fluid coupling – images provided from Marinack, Mpagazehe, and Higgs 2012 [40]. (a) The shear cell domain (b) Results comparing the particle velocity vs. the position in the cell.

In Fig.4.7b, the results from the current framework (Eulerian-Lagrangian) are compared to other particle-fluid results in a similar geometry. It can be seen that the results from the current framework agree very well with the previously published modeling results of Jhurani and Higgs [41] and the experimental results of Shapley et al. [42].

4.2.2 Fluid on Particle Ergun Drag

There are several assumptions in Stokes drag that do not lend it to wide-scale usage for many particle-fluid tribo-systems – namely, spherical and solitary particles. In many tribo-systems, the particles are not round and are usually in a fluid which contains many

other particles. As such, efforts were made to include a different modeling technique into the framework to account for these issues. The Ergun equation (Eq. 4.5) was implemented into the framework which takes into account the particle shape and local-solid fraction. .

$$f = C_1 \frac{(1 - \varepsilon)^2}{\varepsilon} \frac{\eta(\Delta u)}{d_p^2} + C_2(1 - \varepsilon) \frac{\rho(\Delta u)|\Delta u|}{d_p} \quad \text{Eq. 4.5}$$

The Ergun equation is a semi-empirical correlation to predict the friction factor, f , of the flow through packed particle beds, where ε , d_p , η , and ρ represent the void-fraction, the particle diameter, the fluid viscosity, and the fluid density respectively. The constants C_1 and C_2 are the Ergun Constants and are usually set to 150 and 1.75 based upon experimental data and particle shape [43]. In the current work, the cell-averaged technique used by Li is employed [39] and viscous portion of the Ergun equation is used representing the Kozeny-Carman equation. By employing this version of the Ergun equation to calculate the friction on a packed bed filter, the pressure drop across the particle bed can be predicted.

To evaluate this particle-fluid coupling in the model, a packed bed of particles was initialized inside of a column of fluid. At the top of the fluid, a moving boundary was created to force fluid through the bed of particles. The velocity of the moving boundary was varied to represent different superficial velocities. Images of this domain are displayed in the Fig. 4.8.

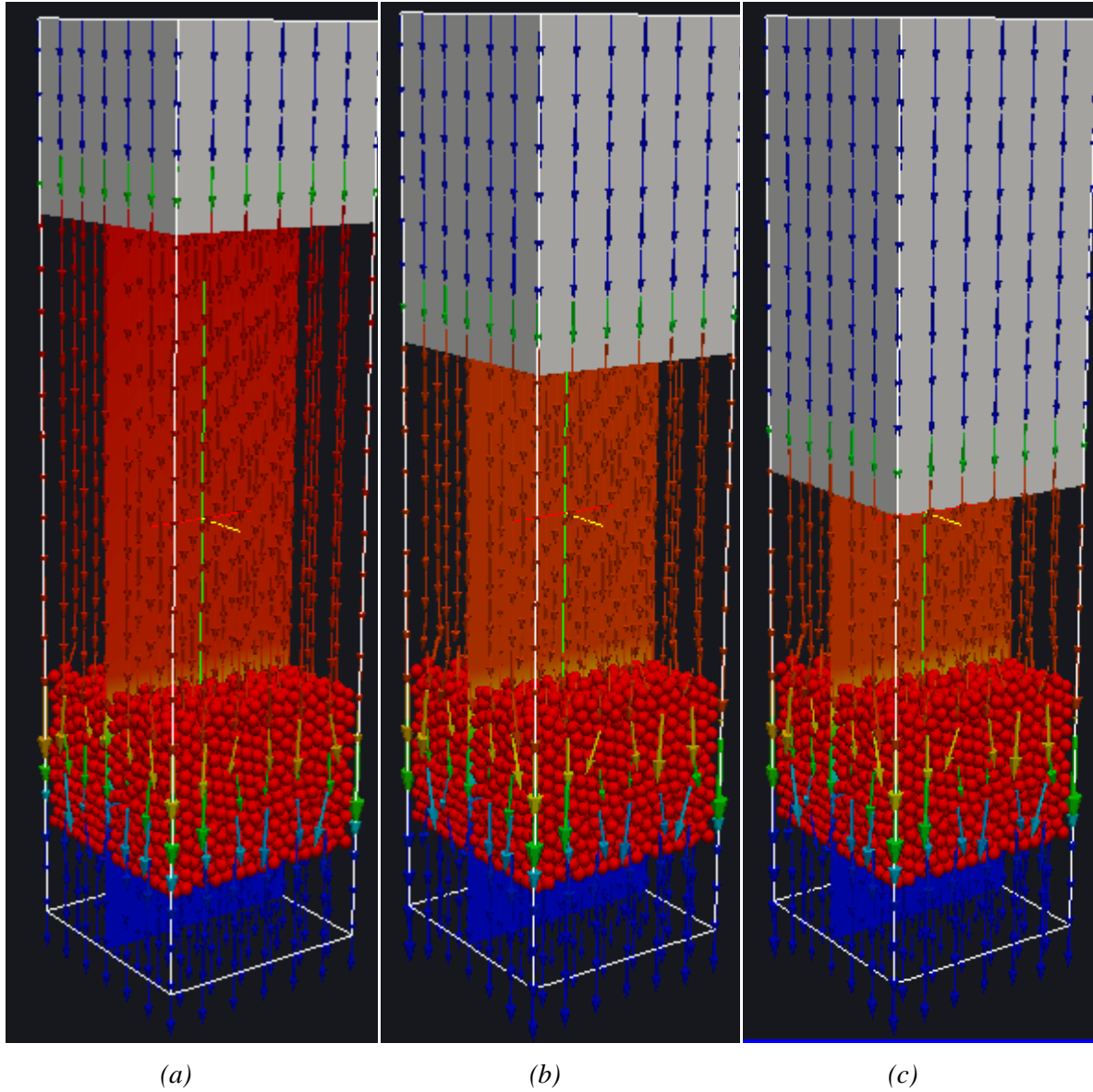


Fig. 4.8 Images of the three-dimensional filtration simulation at different times (a) $t=1$ second (b) $t = 2.5$ seconds (c) $t = 5$ seconds

In Fig. 4.9, the analytical Ergun equation and the results from the model are displayed. It can be seen that the results from the model and the analytical equation agree very well.

Such agreement is encouraging as the Ergun equation has proven to be quite good at predicting the results of experiments.

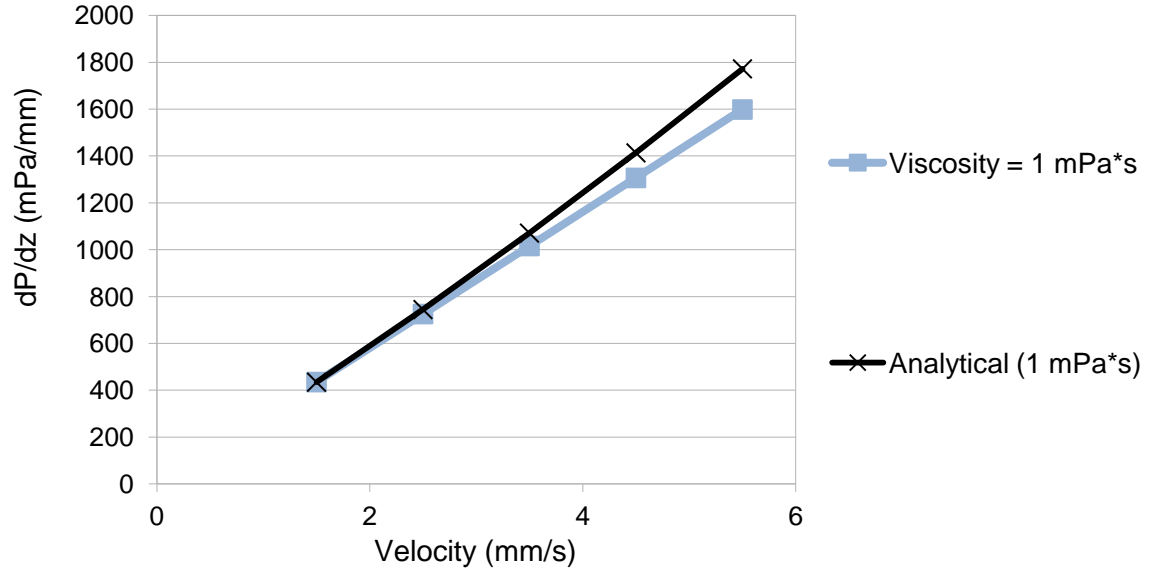


Fig. 4.9 Comparison of analytical equation and the computational framework in the prediction of the pressure drop across the particle bed.

4.3 Particle-on-Fluid Forces

In the current framework, two-way particle-fluid coupling is achieved by applying Newton's third law to account for the forces generated on the fluid. The Navier-Stokes equations (Eq. 2.1 and Eq. 2.2) are represented as forces per unit volume. As such, the source term, f , represents a force per unit volume on the differential fluid cell. Once the force on the particle is calculated (from the Stokes or Ergun equations) the force can then be imparted back onto the Eulerian phase. It is this coupling that allows the fluid to be affected by the particles and results in the pressure drop shown in Fig. 4.9.

4.4 Particle-Surface Coupling

In the modeling framework, there are two forms of particle-surface coupling. In both forms, a boundary is constructed with which the particle can interact. In this section, these two methods will be discussed.

In the first form of particle-surface coupling, the geometric plane with which the particle can interact is resolved mathematically. In most cases, this is straight forward as the plane is aligned with the Cartesian surface. Therefore, the position of the particle can be calculated in relation to its distance from the boundary in a collision technique that is similar to the particle-particle collisions described in Chapter 3.

Using this Cartesian surface formation works particularly well for colliding particles with pixilated volume units (voxels) as they are formed on a Cartesian grid in this framework. To do this, the voxel-space in which the particle is located is calculated. Once this is done, a series of boundaries are constructed based on the heights of the voxels and the collisions are resolved accordingly. In Fig. 4.10, an image is displayed of particles trapped between two voxelized surfaces. This image was produced by the current framework.

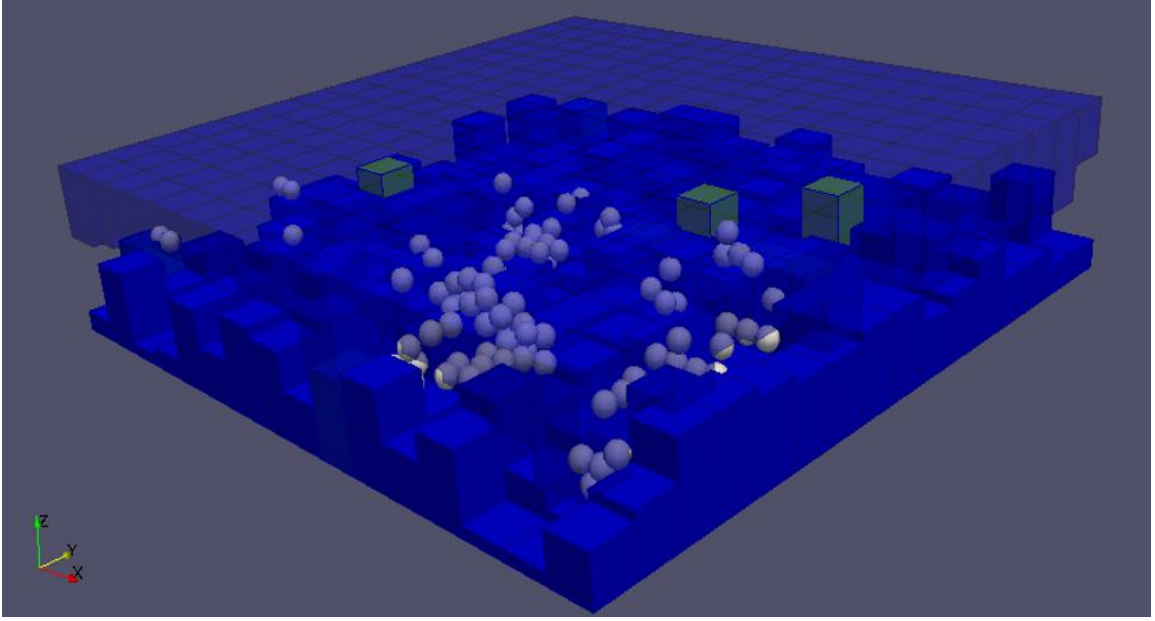


Fig. 4.10 Particles trapped between two contacting surfaces voxelized surfaces.

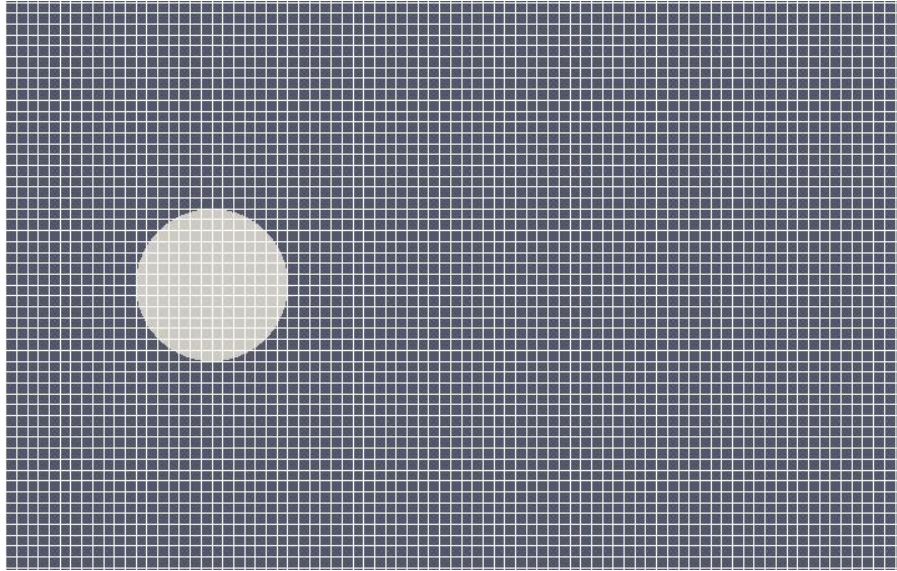
The second method used to resolve particle-surface collisions in this work allows for the resolution of particle collisions with surfaces that are not on a Cartesian grid. To accomplish this, a series of nodes on the surface are created and a repulsive function is defined to resolve particle-surface collisions on these objects.

4.5 Surface-Fluid Coupling

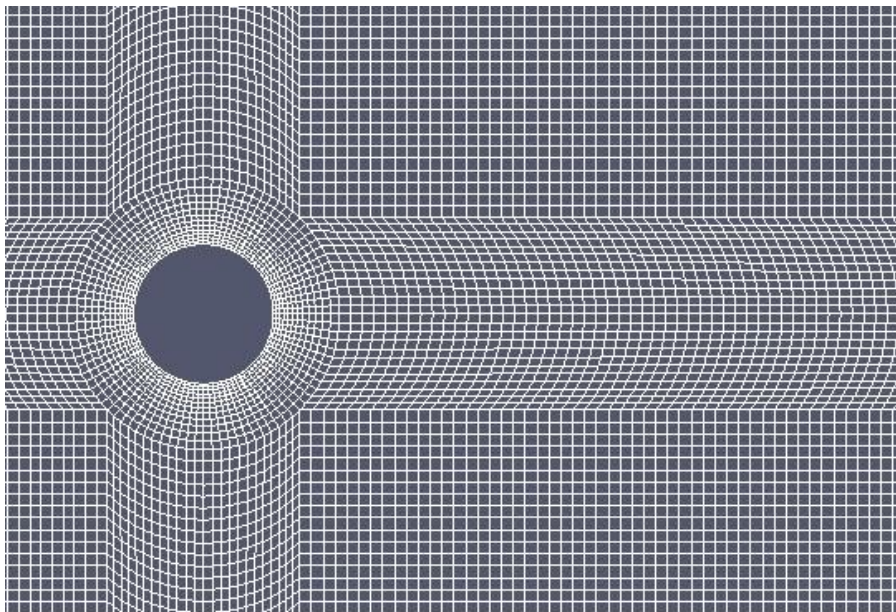
The last coupling type in this work is the surface-fluid coupling. Just like the particle-surface coupling, methods had to be employed to allow for surfaces which do not align to the Cartesian grid. Modeling the interaction of fluid with boundaries in CFD is traditionally done by several approaches. The first approach, and the most straightforward, is to use an unstructured grid using the finite volume method. This approach has

been widely used in CFD and has been popularized by many commercial CFD codes. Though straight-forward, a weakness of this approach is that to model moving boundaries, the domain has to be re-meshed for large translations or deformations of the immersed object. Moving boundaries are an important part of tribological applications and such a burden – frequent remeshing of the domain – would prove to be cumbersome. As an alternative, the immersed boundary method is employed. The immersed boundary method, introduced by Peskin [44], is a modeling technique in which the fluid is made to behave as if a boundary were present. To do this, the Navier-Stokes equations are modified in such a way that the forcing term is adjusted to force the velocity at the fluid-solid interface to assume a specified velocity. In practice, the no-slip boundary condition is typically applied and the forcing term in the Navier-Stokes equations is set to make the velocity at the fluid-solid interface equal to the velocity of the solid.

The immersed boundary method has been applied in the current work to model the flow past an immersed cylinder. For comparison, the OpenFOAM modeling framework is also used to model the same phenomenon using an unstructured mesh.



(a)

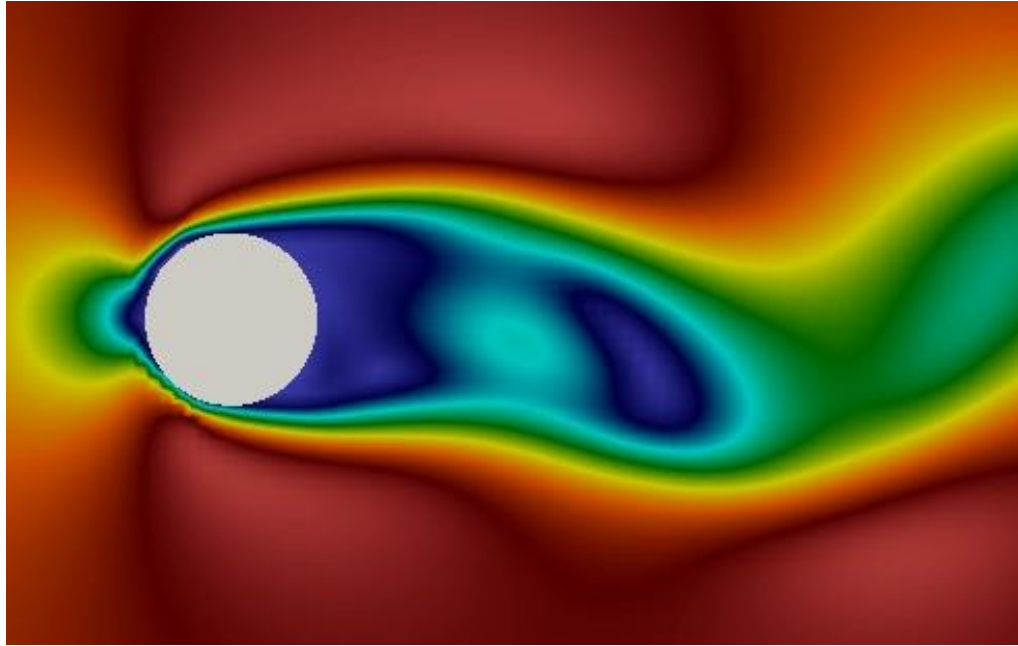


(b)

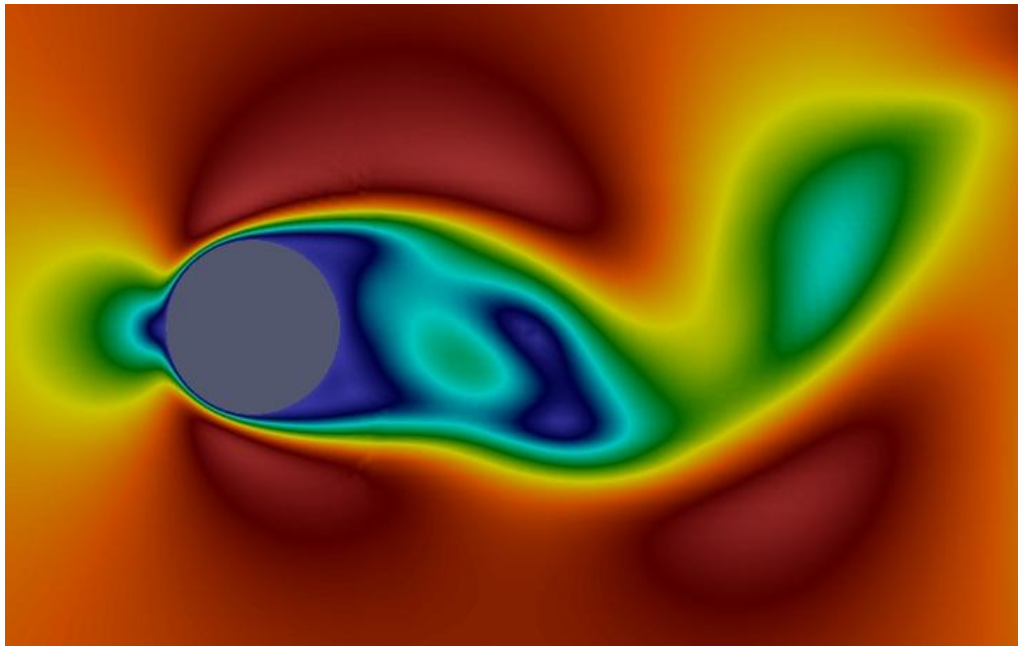
Fig. 4.11 Computational mesh used to study flow around a cylinder (a) the current Eulerian-Lagrangian modeling framework (b) OpenFOAM

In Fig. 4.11, it can be seen that the meshes for the two frameworks look significantly different. The mesh around the object using OpenFOAM has been tailored to

approximate the surface of the immersed cylinder. In the case of the current framework's mesh, it can be seen that a uniform Cartesian mesh is employed. For both the current model and OpenFOAM, approximately 70,000 fluid elements were used in the simulation. It should be noted that a high mesh density is typically more important close to the immersed object than it is away from the immersed object. In future revisions of the current framework, it may be ideal to construct a mesh grading so that grid spacing increases away from the immersed object. Such a change would help with computational efficiency for stationary immersed objects. However, more care would have to be taken for moving immersed objects if mesh grading were implemented. It should also be noted that OpenFOAM now includes a module for the immersed boundary method. The comparisons in this section are primarily to validate the current framework's ability to capture vortex shedding phenomena when compared to experiments. OpenFOAM's predictions are provided only for the purpose of comparing another computational framework to the one developed in this thesis. For the comparison, the unstructured mesh around the cylinder is used in OpenFOAM, as opposed to the immersed boundary method in OpenFOAM, because this technique is a widely popular method to model flow around complex geometries with CFD.



(a)



(b)

Fig. 4.12 Velocity magnitude around the cylinder as predicted by computational fluid dynamics (a) the current Eulerian-Lagrangian modeling framework (b) OpenFOAM

In Fig. 4.12, the velocity magnitude of flow past the cylinder is displayed for both the current Eulerian-Lagrangian modeling framework and OpenFOAM. It can be seen that the general structure of the flow looks similar for both modeling frameworks. However, the unstructured mesh in OpenFOAM does a better job at capturing the smooth boundary layer around the cylinder. This is believed to be the case because of the relatively refined mesh used around the cylinder as opposed to the coarse mesh in the current Eulerian-Lagrangian framework. Better grid refinement around the object would help to mitigate this issue.

For validation, the experimental results of Hammache and Gharib [45], Roshko [46], and Williamson [47], were used. Each author performed flow-past-cylinder experiments at various fluid inlet velocities and developed an empirical correlation which relates the vortex shedding period to the Reynolds number (Re).

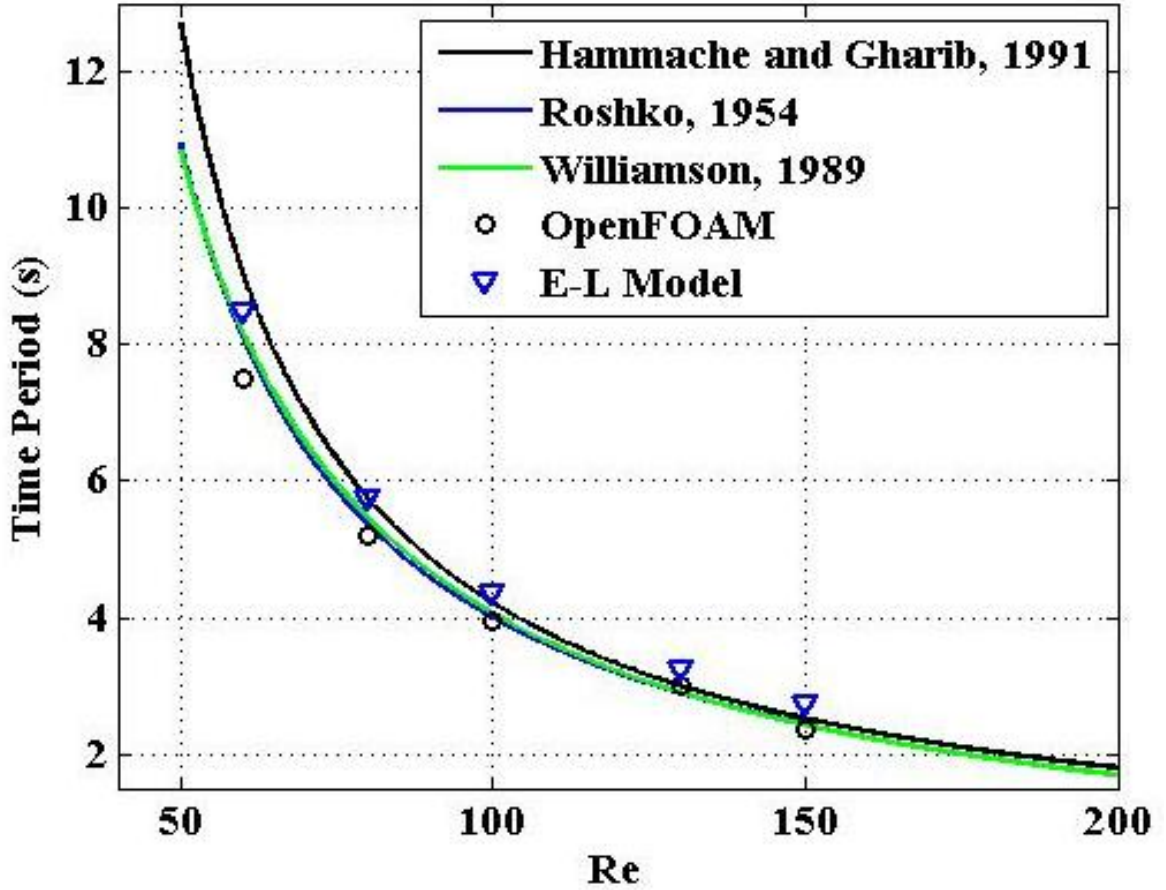


Fig. 4.13 A comparison of the current Eulerian-Lagrangian framework to experiments and OpenFOAM.

In Fig. 4.13, these experimental correlations (solid lines) are plotted against the results of the current Eulerian-Lagrangian modeling framework and OpenFOAM. It can be seen that there is very good agreement among the models and the experiments. It should also be noted that the blended derivative used to discretize the Navier-Stokes equations in the current Eulerian-Lagrangian modeling framework produced better results when the proportion of the second-order central difference was increased from 10% to 50%. The results from the 50% blended difference are displayed in Fig. 4.13.

As a final validation of the fluid-surface interaction, the length of the separation bubble of flow around the cylinder in the current Eulerian-Lagrangian model was compared to the experimental results of Nishioka and Sato [48]. Additionally, the results of OpenFOAM and Park et al. [49] are also plotted for reference to computational predictions.

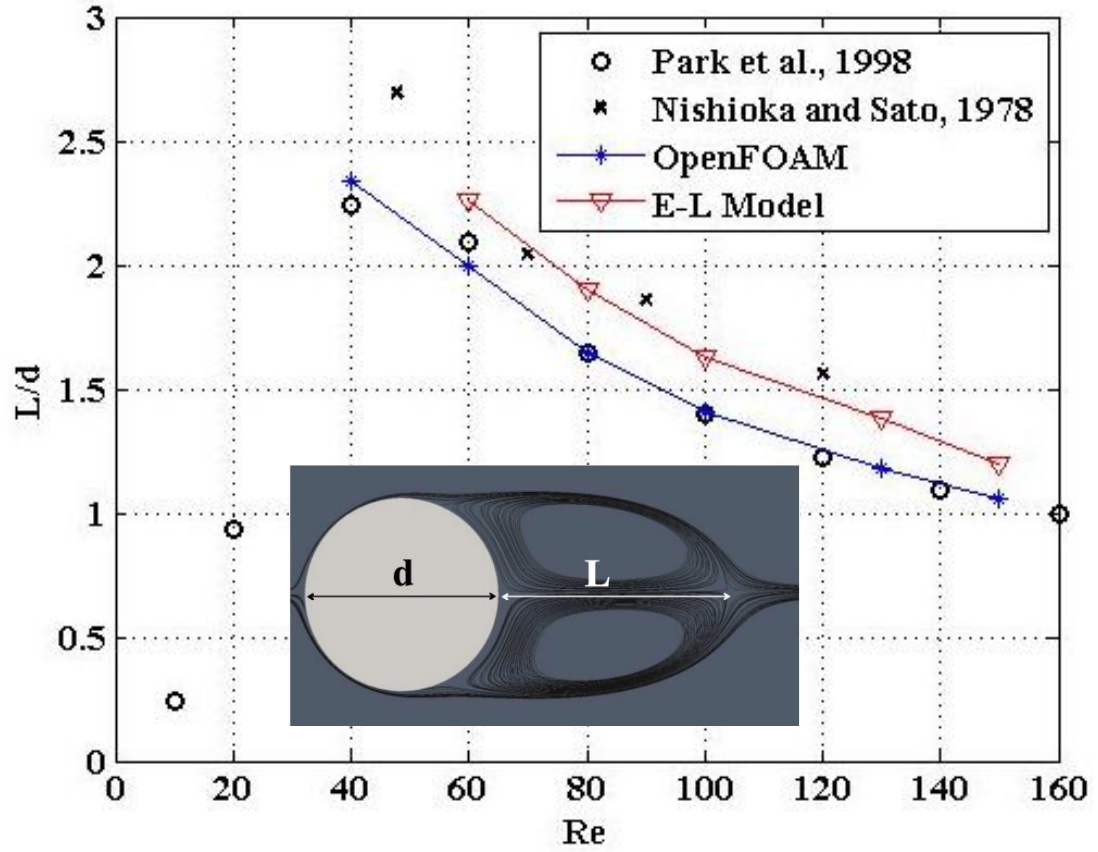


Fig. 4.14 A comparison of the separation bubble length prediction of the current Eulerian-Lagrangian framework to experiments and OpenFOAM.

In Fig. 4.14, it can be seen that the computational results of Park et al. [49] and OpenFOAM are in very good agreement. The results from the current Eulerian-Lagrangian model agree very well with the experimental results of Nishioka and Sato [48].

Chapter 5: Implementation: From Code to Software

In this chapter, the implementation of the modeling framework is described. First the code structure is listed and then the pre and post-processing methods are detailed.

5.1 Code Organization

This framework was built from scratch using the C++ computing language. The code is organized by the physics involved in the solution. These categories are (1) fluid dynamics “CFD”, (2) particle dynamics “PD”, and (3) solid dynamics “SOLIDS”. Finally, there is one directory in which the main loop is executed called “Base”. The directories are shown in Fig. 5.1.

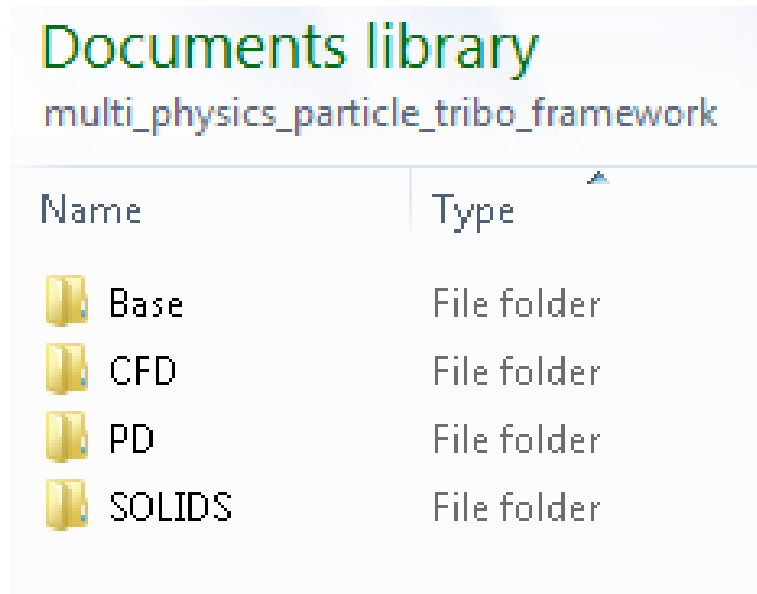
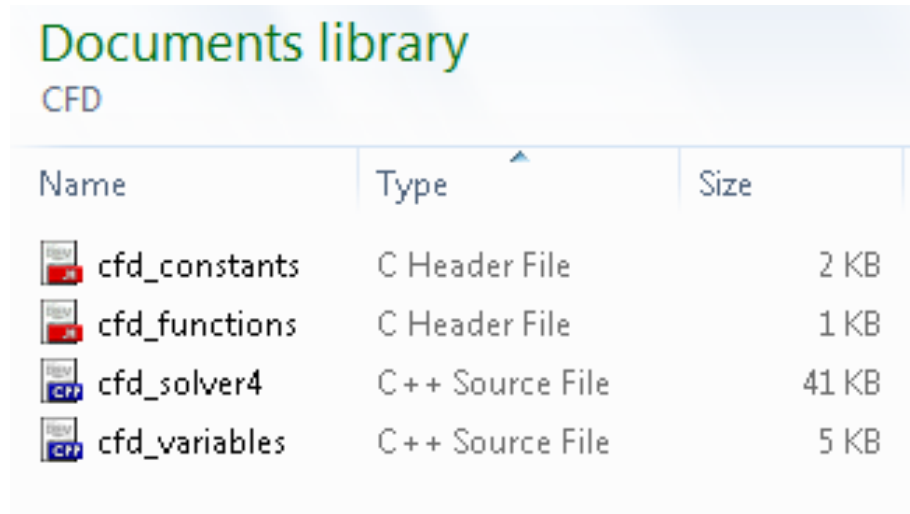


Fig. 5.1 The primary directories in the framework

In each of the physics directories (CFD, PD, SOLIDS) there are 4 files. One header file contains the constants, one header file contains the functions, one source file contains the

variables, and one source file is the actual solver. As an example, these are listed in Fig. 5.2 for the CFD directory. However, all of the other physics directories contain the same four files with the respective change in name.







| Name | Type | Size |
|---|-----------------|-------|
|  cfd_constants | C Header File | 2 KB |
|  cfd_functions | C Header File | 1 KB |
|  cfd_solver4 | C++ Source File | 41 KB |
|  cfd_variables | C++ Source File | 5 KB |

Fig. 5.2 Organization of files in the CFD sub-directory

Inside of the constants header file, all of the variables that remain constant in the code are listed. Some of these include the grid size spacing and the relaxation parameter for the iterative solvers. In the variable file, the variables that can vary during the simulation are listed. Some of these are the viscosity and density of the fluid. In the functions folder, each of the functions are declared. Finally, in the solver, all of the functions are written. The code was written in this manner to allow for easy navigation of the over 6500 lines of code. It was also written in this “easy-to-follow” manner so that end users would feel free adding new variables and modifying code. Linking the files is done at the compilation time using “extern” keyword to alert the compiler that the parameters are defined in the various sub-directories.

Inside of the “Base” folder, the code is executed and the functions from the sub-directories are called. When certain modeling techniques are disparate in their restrictions on the time-steps (such as the case for the CFD and the DEM) a variable is defined such that the user can run the DEM code multiple times for every time the CFD is run.

5.2 Parallelization

The code has been parallelized using the OpenMP application programming interface (API). As such, the code is suited to be run on shared-memory computers. Thus far it has been successfully run in parallel on the Pittsburgh Super Computer “Blacklight”. As an indication of the increase in computational efficiency experienced by running the code over multiple cores, a case study was performed in which the code was run on increasing numbers of cores. The results from this case study are show in Fig. 5.3.

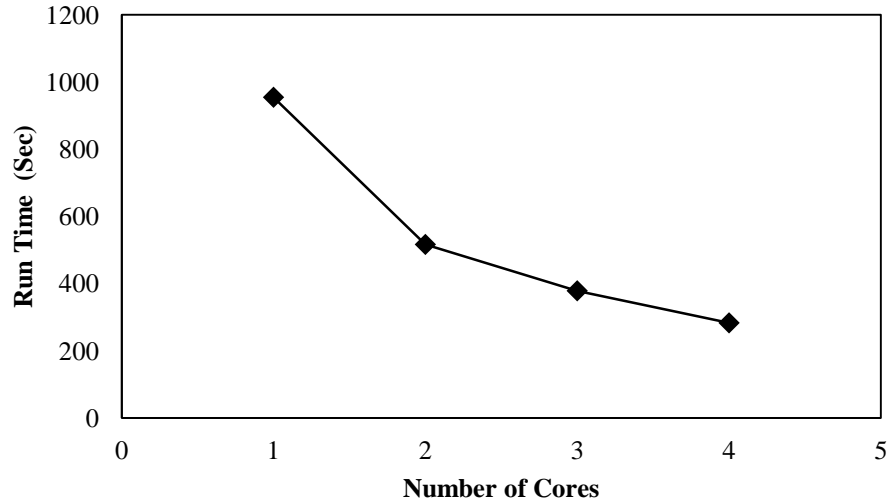


Fig. 5.3 Decreased computational time as a result of parallelization of the current framework

It can be seen in Fig. 5.3, that as the number of cores increases, the code takes less time to run.

5.3 Pre-Processing

Much like the open source codes OpenFOAM and MFiX, this framework does not have a dedicated pre-processing graphical user interface (GUI).

The flow field, fluid properties, particle positions, particle properties, boundaries, and solid objects immersed in the flow must all be initialized before the solvers can run. The pre-processing step is where this is handled. In the current framework, pre-processing is controlled by the user's direct modification of the source code. However, there are a few modules already in place which can assist with this such as random particle location generation and the ability to import particle positions from a file. In the pre-processing step, the boundary conditions are also specified.

5.4 Post-Processing

Outputs from the code are written in the Base directory. At the time of compilation, a series of directories are created to store the “.vtk” file outputs which can be visualized in Paraview. Paraview is an open source post-processing program developed by Sandia National Laboratory. It is well-suited to serve as a post-processor for the current Eulerian-Lagrangian framework as it can post-process the particle, fluids, and surfaces in the model. Moreover, any field data, such as temperature and pressure, can also be displayed in paraview. An image of an example output from the framework which has been displayed in Paraview is shown in Fig. 5.4.

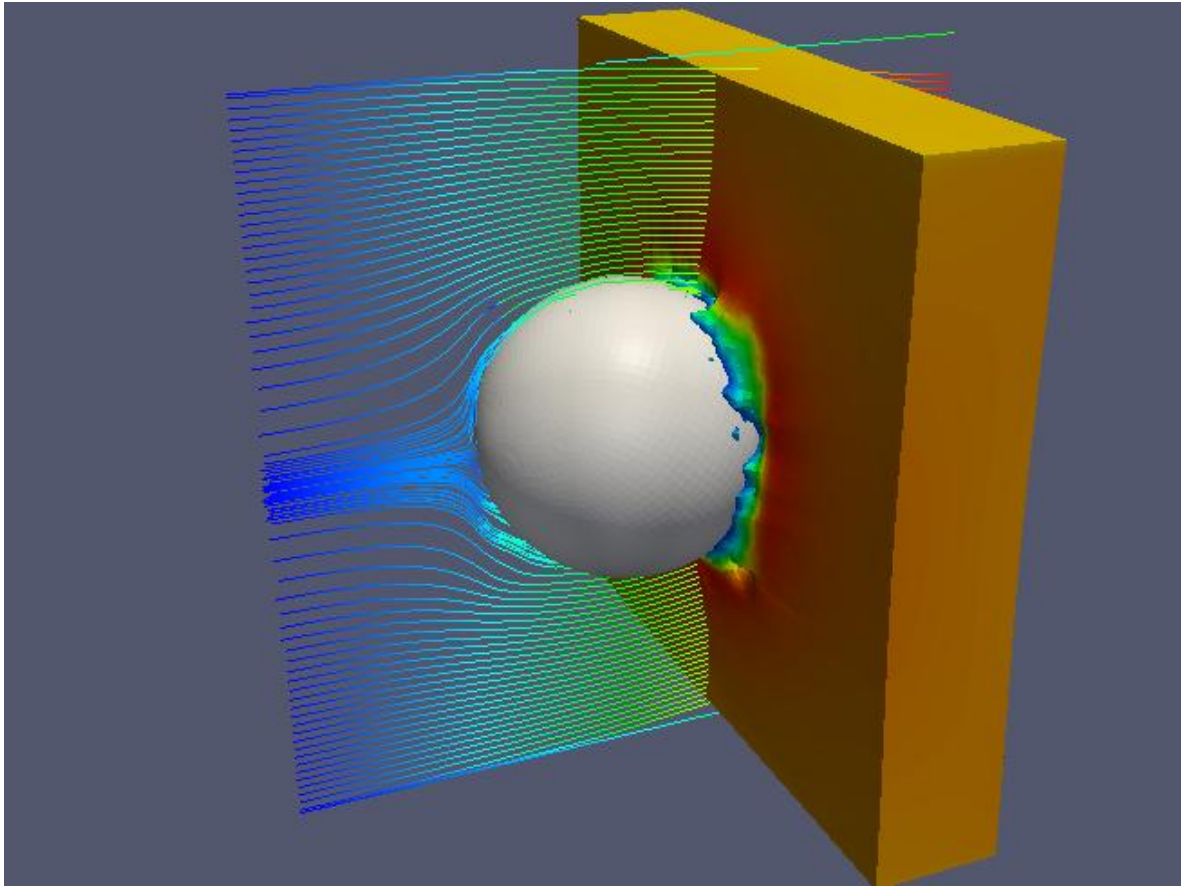
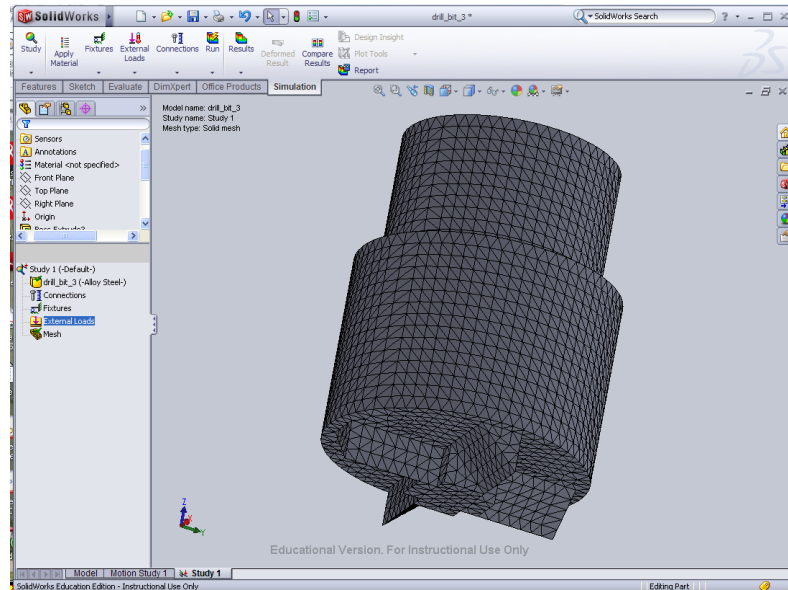


Fig. 5.4 An image generated in Paraview produced from the current framework showing the streamlines around an immersed particle.

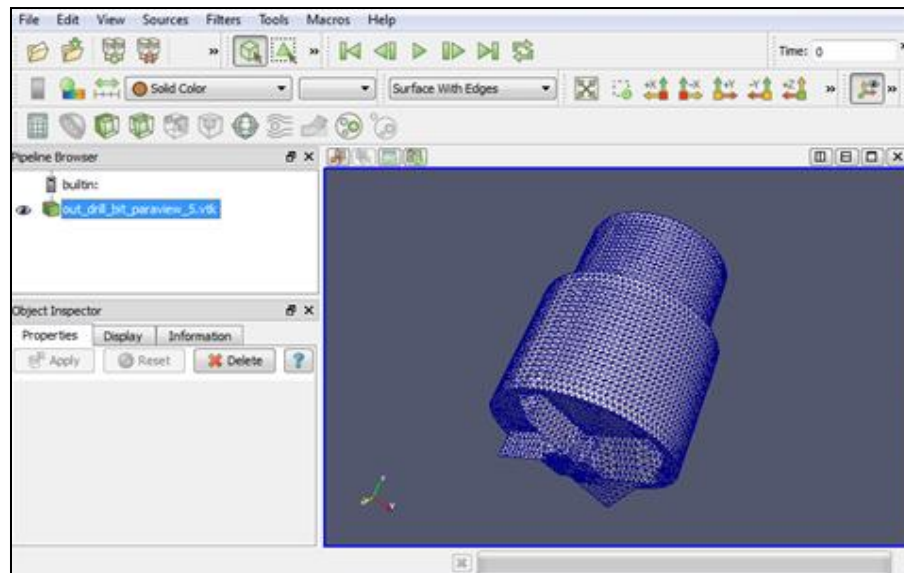
5.5 Importing Objects from Solidworks™

The functionality of this framework is greatly extended due to the ability to import general geometries from CAD models. CAD models can be meshed in SolidWorks™ and imported into the framework.

Once the CAD model has been imported from SolidWorks™ particle-solid coupling allows the CAD model to interact with the flow field. In Fig. 5.5a an image of the model, created and meshed in SolidWorks™, is displayed. In Fig. 5.5b, an image of the model after it has been imported into the current modeling framework and post-processed in paraview is displayed.



(a)



(b)

Fig. 5.5 Importing Solidworks CAD models into the current framework. (a) an image of a drill bit in SolidWorks. (b) The same drill bit post-processed in Paraview after having been imported by the current framework.

Chapter 6

Erosive Wear: Experimentation and Modeling

In this section, erosive wear is studied as a potential validation tool for the current modeling framework. Since the study of erosive wear has particular importance for next-generation space missions, the author carried out the experimental component of this work at the NASA Glenn Research Center. As such, erosive wear by lunar (i.e., moon-based) dust simulant and efforts to model it are presented in this section. In the appendix, additional details of the erosive wear experiments are provided.

6.1 Lunar Dust Erosive Wear Studies

Though there is much evidence for the deleterious effects of lunar dust abrasion on prior lunar missions, erosion is another wear mechanism of lunar dust that can cause significant damage to critical lunar hardware [50]. Spacecraft landing on the Moon typically fire retrograde rockets to de-orbit and reduce their velocity during descent. When close to the lunar surface, dust is entrained into the plumes of these retrograde rockets and accelerated by the exhaust gases. The low lunar gravity and the lack of a significant atmosphere to create drag, allow these lunar dust particles to travel long distances at high velocities. The fast-moving lunar dust particles have the potential to cause significant erosive wear to nearby structures. Evidence of this phenomenon was provided during the Apollo 12 lunar mission. The Apollo 12 lunar module landed approximately 155 meters from the Surveyor III Lunar Probe which had been sent to the Moon 31 months prior. The Apollo 12 astronauts returned various components of the

Surveyor III probe back to Earth including the complete television camera, the scoop from the surface mechanics sampler, sections of unpainted and painted aluminum tubes, and a television cable [51]. Shortly after the return of Apollo 12 to Earth, evidence that lunar dust particles had been accelerated by the Apollo 12 LM exhaust and caused erosive wear damage to the Surveyor III lunar probe was provided by several observations.

In 1970, Cour-Palais was one of the first to use the term “sand blast” to describe his observations on the effect of exhaust-blown lunar dust particles removing the uppermost layers of material on the Surveyor III camera that had been brought back to Earth [52]. Cour-Palais stated that there was a concentration of craters on the Surveyor III camera, which he presumed to be generated by the Apollo 12 LM landing. These craters were 10 to 100 times greater on the area of the Surveyor III camera that was facing the Apollo 12 LM landing site than the areas that were not. Cour-Palais also discussed the whitening effect of the lunar dust sandblasting on the Surveyor III camera’s paint. The paint of the Surveyor III camera had turned a tan color due to the UV exposure on the Moon in the 31 months prior to Apollo 12’s arrival. As compared to the other portions of the Surveyor III camera, the cratered areas which faced Apollo 12’s landing site were white in color which likely indicated that a fresh surface had been exposed by the lunar dust sandblasting. The whitening of the Surveyor III camera due to sandblasting was later corroborated by Jaffe in 1971 [53]. Jaffe went on to hypothesize the lunar dust particle impact velocities to be no less than 70 m/s given the lunar topography on which the Surveyor III probe and the Apollo 12 LM were situated. Then, in 1972 NASA released a comprehensive report on the analysis of Surveyor III materials returned by Apollo 12. In

this report, Brownlee et al. studied the impact craters, or pits, on the Surveyor III camera filters and concluded that the lunar dust particles were most likely traveling between 300 – 2000 m/s upon impact [54].

In 2011, material coupons from Surveyor III were analyzed by Immer et al. who used advances in surface metrology, developed in the 42 year span since Apollo 12, to provide a better understanding of the lunar dust particle erosion experienced by Surveyor III [50]. Immer et al. concluded that the pitting and scouring on the surface of the coupons was most likely caused by lunar dust accelerated by the exhaust plume of the Apollo 12 landing. They also stated that the erosive wear damage to Surveyor III may have been orders of magnitude worse if it were not for a unique set of circumstances, created by the lunar topography, which resulted in the majority of the lunar dust particles missing Surveyor III. In 2011, Clegg et al. simulated the erosive wear potential of lunar dust by conducting a series of erosive wear experiments using a sandblasting apparatus to erode materials with the lunar dust simulant JSC-1A [55]. Even at the moderate velocities of 30-85 m/s, Clegg et al. found that Kevlar and carbon fiber experienced substantial erosive wear damage. They concluded that Vectra fabric proved to resist erosive wear by the JSC-1A particles when compared to the other materials tested.

These studies on the erosive wear potential of lunar dust indicate that future missions to the Moon will need to consider carefully the effect that landings can have on nearby spacecraft and structures. Recent interest in this topic has been generated by the Google Lunar X-PRIZE (GLXP) in which teams compete to land robotic vehicles on the Moon. Efforts to preserve historic lunar landing sites of the Apollo missions from being eroded (sandblasted) by these teams will require an investigation into the erosive wear potential

of lunar dusts. The current work seeks to provide quantitative data on the potential effects that lunar dust erosive wear can cause on lunar systems. Erosive wear experiments were conducted on various candidate lunar construction materials using the JSC-1AF lunar simulant. The resulting mass loss was recorded as well as the changes in optical performance. In the following sections, the experimental methods employed and results of this study are presented.

6.2 Erosive Wear Experimental Methodology and Materials

The tests described in this work were carried out using the Dust Erosion Experimental Rig (DEER) in the Jet Erosion Laboratory at the NASA Glenn Research Center in Cleveland, Ohio, USA. The DEER aerosolized particles using a TOPAS[®] solid aerosol generator. The aerosolized stream of particles was then accelerated toward the specimen with compressed air. A schematic of the DEER and a photo of the device are displayed in Fig. 6.1.

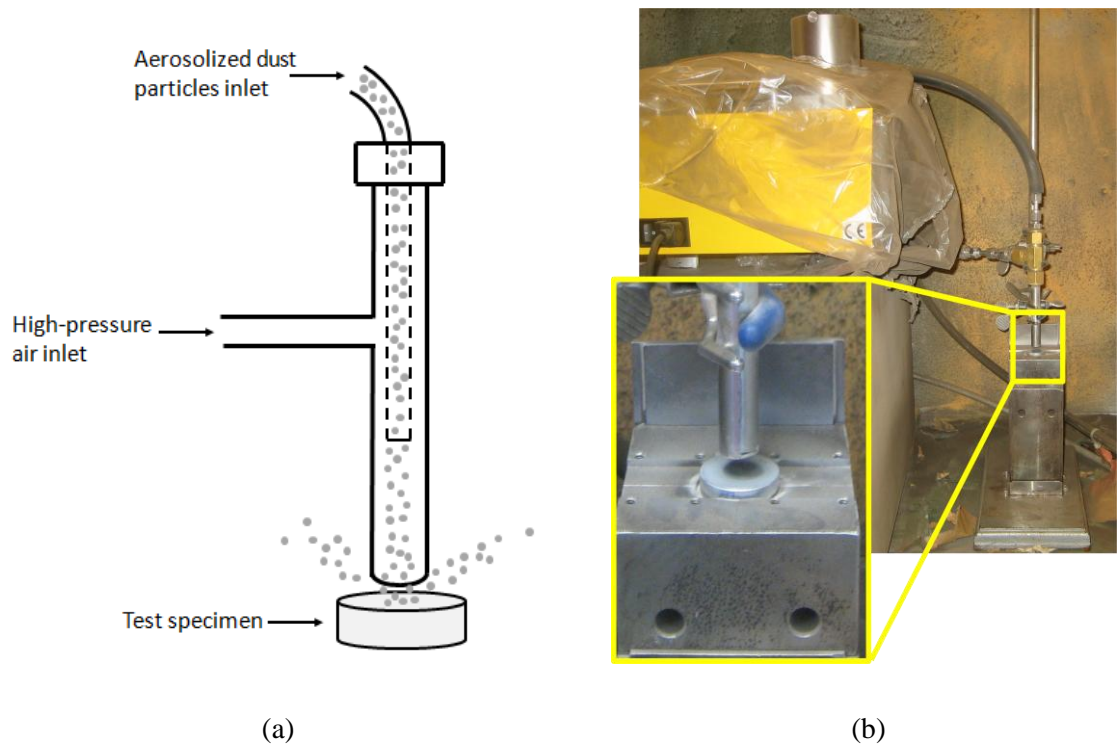


Fig. 6.1 Images of the Dust Erosion Experiment Rig (DEER) (a) schematic diagram (b) photograph of test hardware

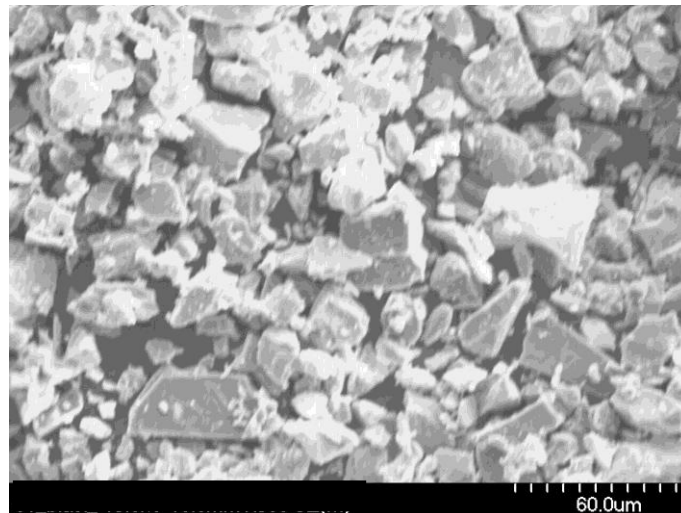
The mass flow rate of the erodent particles was set to 2 grams/minute. A dual-disk device was used to measure that the particle velocity was approximately 105 m/s. These conditions were maintained for all tests. The DEER was placed inside of a hood and proper personal protective equipment was worn throughout the test to prevent inhaling dust particulates.

6.2.1 *Erodent Particles*

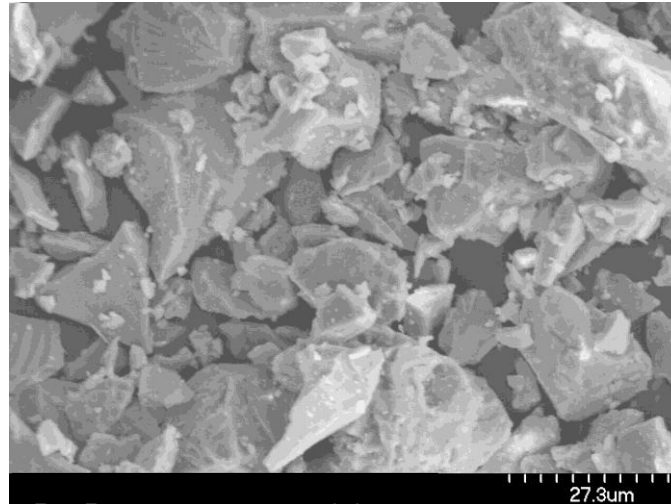
The tests in this study were conducted so that a better understanding of the effect of lunar dust erosive wear could be obtained. As such, using actual lunar dust in this test would

have been ideal. However, due to the scarcity of lunar samples that have been returned to Earth (381.7 kg returned by the manned U.S. Apollo missions and 321 g returned by robotic Soviet Luna missions [56]) a lunar dust simulant was used in this work.

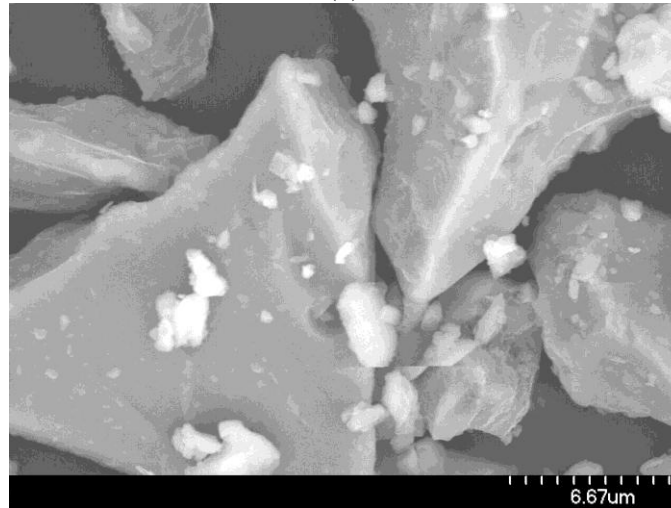
JSC-1 is a simulant developed by the NASA Johnson Space Flight Center to simulate the properties of lunar mare dust. The second iteration of this simulant is JSC-1A. JSC-1AF is the “fine” portion of the JSC-1A simulant and is the erodent used in this work. The average particle size of the JSC-1AF simulant is $24.89\text{ }\mu\text{m}$ as provided by the simulant’s manufacturer, Orbital Technologies Corporation (ORBITEC). A detailed list of the constituents of JSC-1AF can be found in Schrunck et al. [57] and from ORBITEC. In the current study, JSC-1AF was used as the particle erodent because of its similarity to lunar mare regolith, its availability, and its use in prior tribological studies of lunar dust behavior [58, 59]. SEM of the JSC-1AF particles used in the current work is displayed in Fig. 6.2 at different levels of magnification.



(a)



(b)



(c)

Fig. 6.2 Images of JSC-1AF at different magnifications (a) 500x magnification (b) 1100x magnification (c) 4500x magnification

Studies have shown that particle shape can have a significant effect on erosion [60, 61]. Fig. 6.2 displays the sharp and jagged shape of the JSC-1AF which can cause stress concentrations and exacerbate wear in both erosive and abrasive conditions. When produced, the JSC-1AF particles were manufactured in such a way as to develop these sharp features. The constant bombardment by micrometeorites on the Moon fractures lunar rock to create lunar dust particles with angular qualities. Because of the lack of

wind or rain on the Moon, as are present in the formation of Earth dusts, lunar dust particles are not smoothed and thus remain jagged [62].

6.2.2 Erosive Wear Test Specimens

For this study 1045 steel, 6061-T6 aluminum, and acrylic were used as test specimens. These materials were chosen because they are representative of potential materials in lunar craft [50], have been well characterized for lunar dust abrasion [58], or possess significantly different material properties, such as micro-hardness, which may provide insight into the factors dominating erosive wear. The specimens were cut into 1-inch diameter disks with a thickness of ¼-inch. Images of the test specimens are displayed in Fig. 6.3.

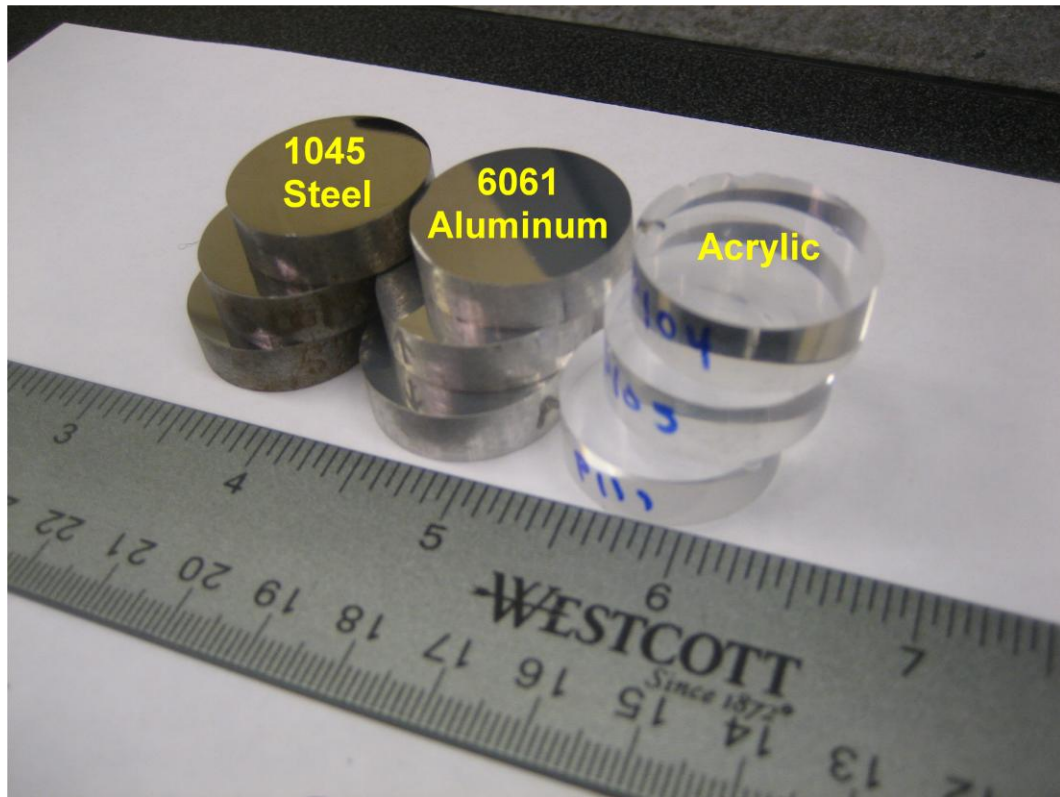


Fig. 6.3 Image of the 1045 steel, 6061-T6 aluminum, and acrylic test specimens

In Table 6.1, the mechanical properties of the specimens are presented. The data in Table 6.1 is provided from the vendor, McMaster Carr[®], except for the microhardness which was measured independently for each specimen using a Beuhler MicroMet Microhardness tester.

Table 6.1 Mechanical Properties of Test Specimens

| Specimen Material | Density (lb/in³) | Tensile Strength (psi) | Micro-Hardness (Hv) |
|--------------------------|------------------------------------|-------------------------------|----------------------------|
| 1045 Steel | 0.283 | 95,000 | 277.3 |
| 6061-T6 Aluminum | 0.098 | 40,000 | 112.0 |
| Acrylic | 0.043 | 9,625 | 22.4 |

In practice, materials for the construction of spacecraft, such as aluminum and sapphire, are typically separated from dust by layers such as paint or optical coatings [50, 63]. However, these layers are usually substantially thinner than the substrates. Thus, if the layers are eroded away, the underlying concern may be to understand how the substrate performs when exposed to erosive environments. Additionally, by understanding how the substrates respond, insight can be obtained and serve as a baseline for the effects of material coatings on surfaces which are exposed to erosive wear by lunar dust.

6.3 Erosive Wear Experimental Results and Discussion

In this section, the results for the various case studies are presented in which the change in mass is described. Each specimen was exposed to JSC-1AF particle impingement for four minutes and each test was repeated three times unless otherwise noted. A 90° (normal) impact angle was used for all tests. In Fig.6.4, images are displayed before and after being exposed to erosive wear by the JSC-1AF lunar simulant.

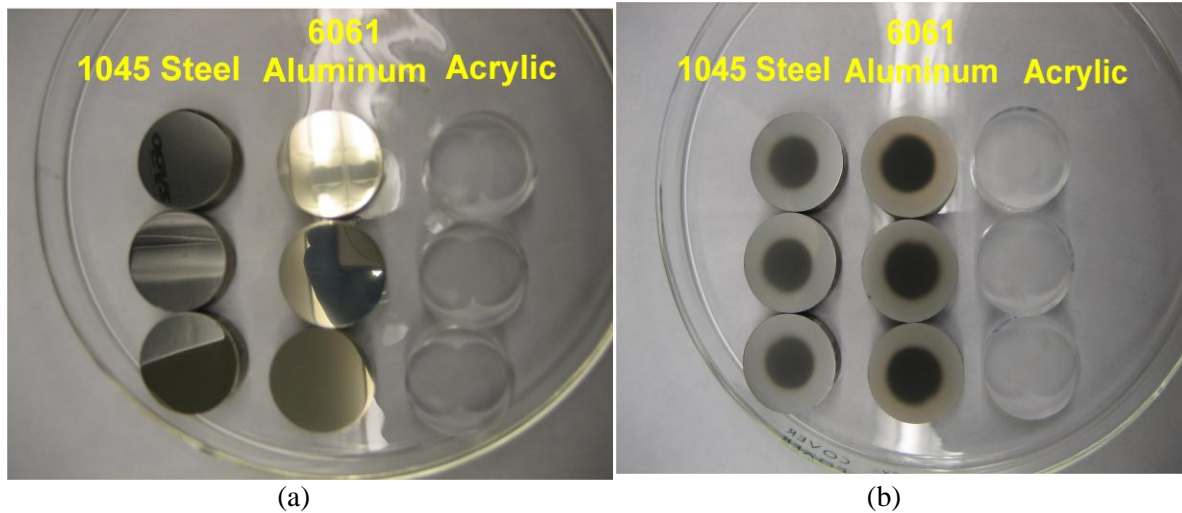


Fig. 6.4 Image of the material specimens before and after testing. (a) fresh specimens (b) eroded specimens

Even at moderate impact velocities, compared to what materials may be experience in lunar conditions, it is clear in Fig. 6.4 that the effects of erosive wear are observed. The dark circles on the steel and aluminum specimens in Fig. 6.4b are the regions of the specimens that were directly under the outlet nozzle of the DEER (Fig. 6.1).

To obtain a better understanding of the change in the surface morphology, SEM was performed on the specimens. In Fig. 6.5, the results of the SEM are displayed.

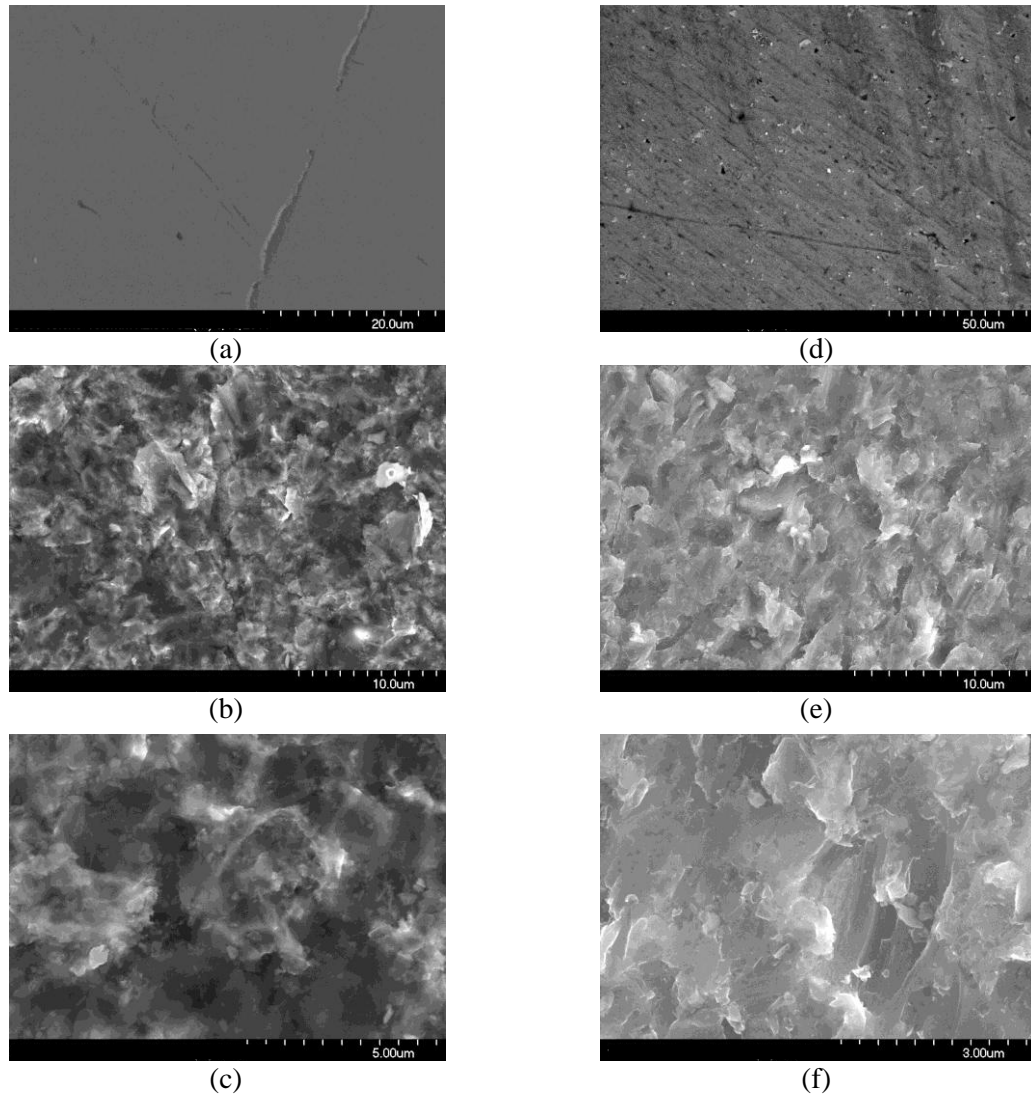


Fig. 6.5 SEM of metallic pieces. (a) pre-erosion steel (b) post-erosion steel (c) detail of post-erosion steel (d) pre-erosion aluminum (e) post-erosion aluminum (f) detail of post-erosion aluminum.

Fig. 6.5 is provided to indicate the changes of the surface at a small scale. Information from these images is used to help explain phenomena, such as changes in surface roughness, described in later sections. Though displayed at slightly different scales, when looking at the images in Fig. 6.5 it is clear that the erosive wear significantly modified the surface of both the steel and the aluminum specimens.

6.3.1 Erosive Wear Material Removal

As the fast-moving lunar dust particles strike the surface of an object, some of the particles may remove material causing erosive wear. To assess the potential damage to a structure by erosive wear, the change in mass of the specimen, after being exposed to erosive wear by JSC-1AF was, studied. Three test specimens of each material were exposed to erosive wear by JSC-1AF. The average change in mass for each material was recorded. The mass loss was normalized by the density of the material (Table 6.1) and the volume loss from each material is presented in Fig. 6.6.

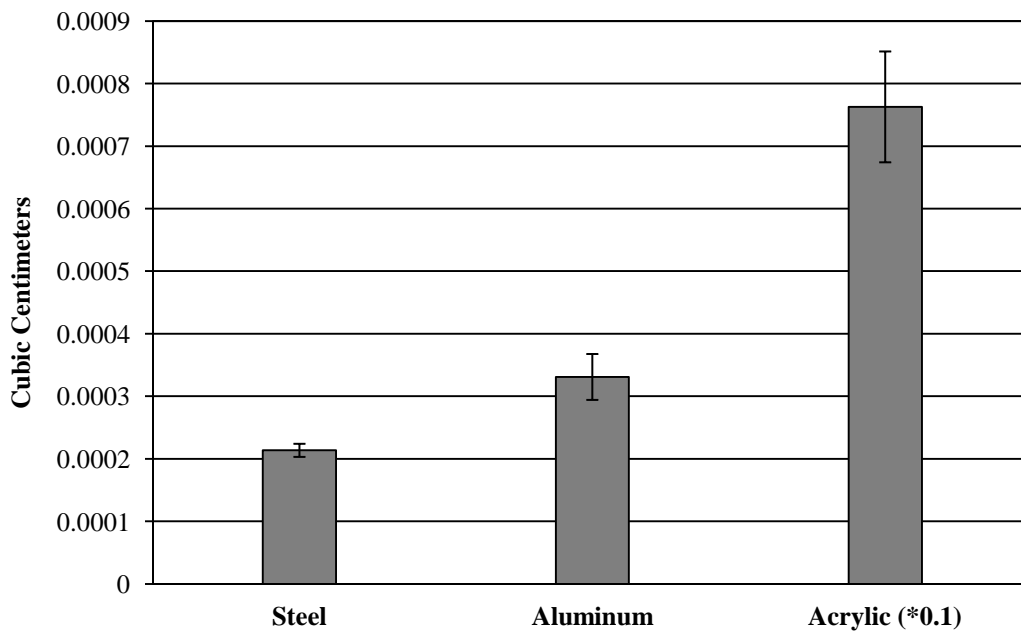


Fig. 6.6 Volume removed from each material after being exposed to erosive wear by the JSC-1AF lunar dust simulant.

It can be seen in Fig. 6.6 that the materials can be ranked from most resistant to erosive wear to least as; 1045 steel, 6061 aluminum, and acrylic. Due to the size of the specimen relative to the plume boundary, a small portion of the simulant may have travelled beyond the test specimen. Nevertheless, the results can be compared qualitatively and they exhibit a trend that matches the results from abrasive wear tests performed by Kobrick et al. [58].

As a final way of assessing the difference in mass loss between the steel and aluminum, optical profilometry, across the middle $\frac{3}{4}$ of the specimens, was performed to get a profile of the wear scar. The results of this analysis are displayed in Fig. 6.7.

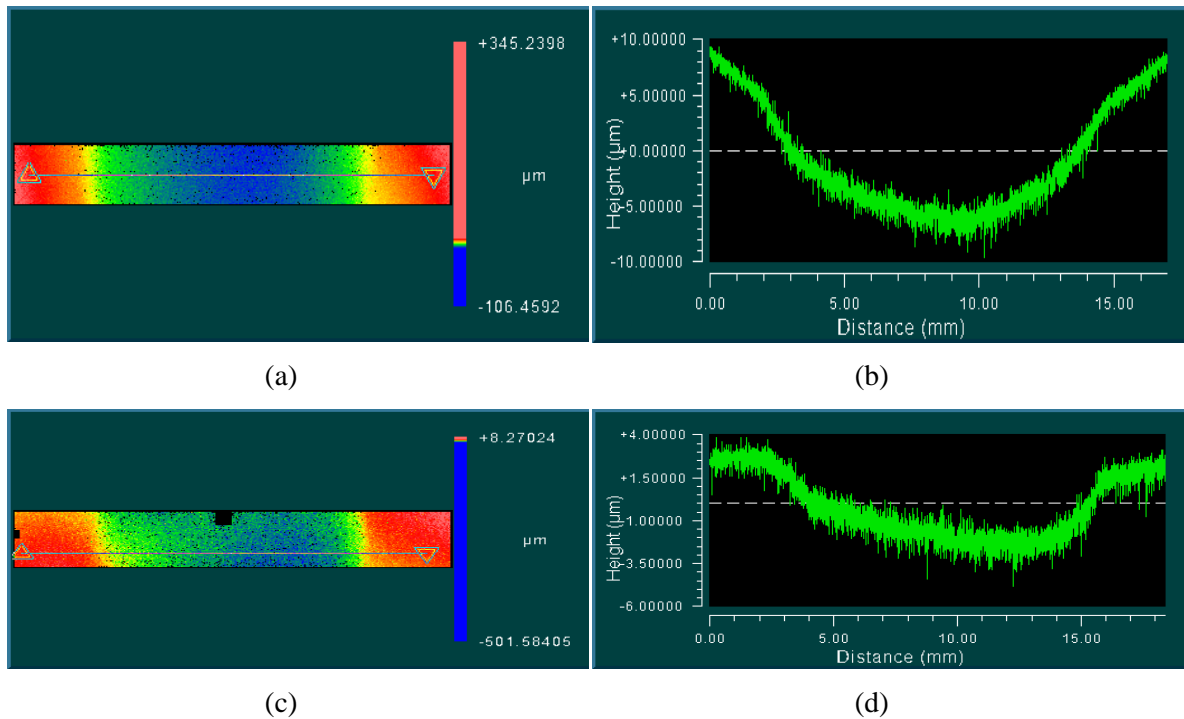


Fig. 6.7 Optical profilometry of wear scar on metal specimens (a) contour map of aluminum surface depth (b) profile across aluminum specimen (c) contour map of steel surface depth (d) profile across steel specimen

In Fig. 6.7, it is clear that the wear scar for the aluminum is deeper than that of the steel. This difference in the depth of the wear scar is additional confirmation of the increase material removal from the aluminum over that of the steel.

6.4 Erosive Wear Modeling

To model the erosive wear by the JSC-1AF lunar dust simulant, a special case study was conducted in which the impingement angle of the lunar dust simulant on the test specimens was altered. Instead of impacting the surface at only 90° , as was the case in the previous section, the impact angle was changed to 30° . The oblique impact angle created a larger area of erosive wear. As a result, larger aluminum pieces were used as test specimens in the DEER. For a fair comparison, these larger test pieces were tested at both 90° and 30° .

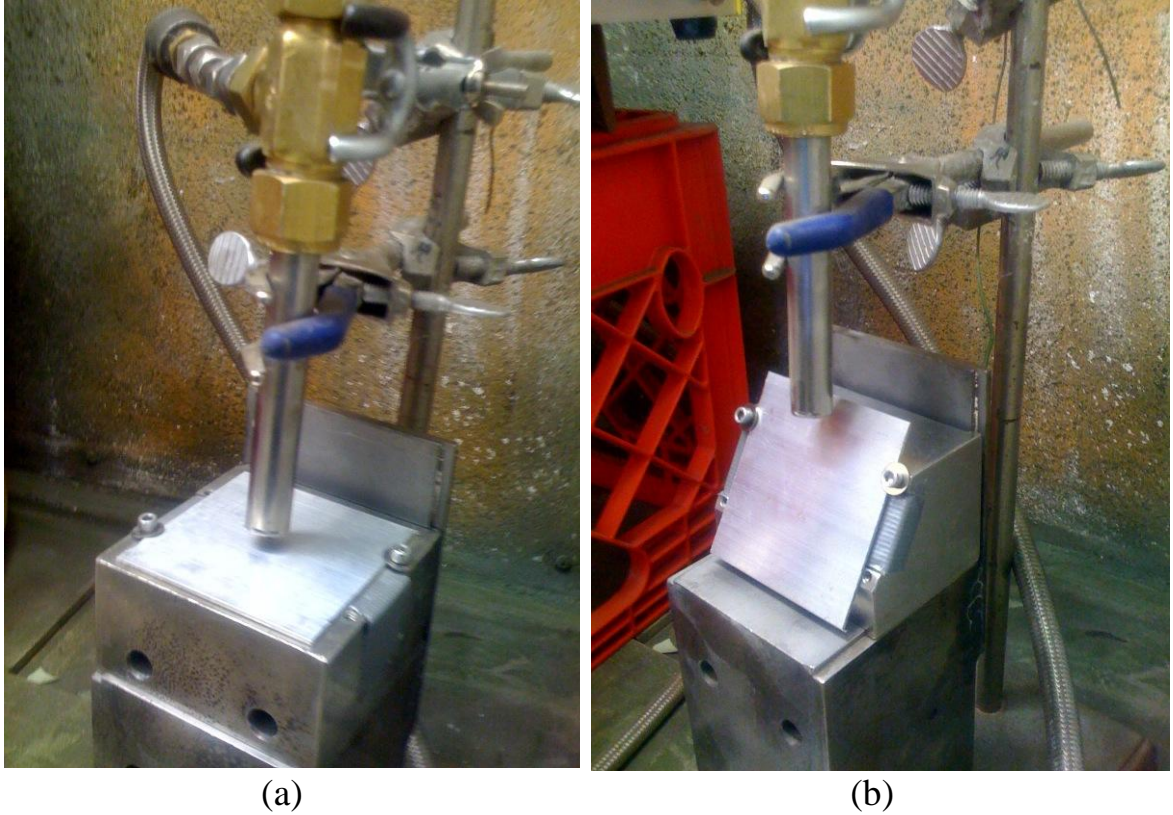


Fig. 6.8 Images of the DEER setup for different impact angles (a) normal impact angle (b) oblique impact angle

In Fig. 6.8, images of these larger test specimens can be seen for an impact angle of 90° and 30° .

After testing, it was clear that the post-erosion surface characteristics of the 30° impact were significantly different than those of the 90° impact. In Fig. 6.9, images of the eroded test specimens for a 90° angle and a 30° angle are displayed.

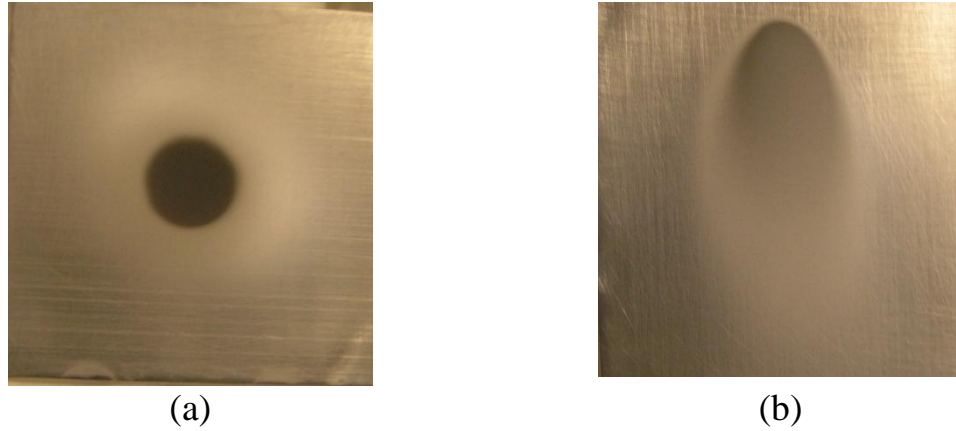


Fig. 6.9 Images of the test specimens post-erosion (a) 90° impact (b) 30° impact

In the 90° impact, the eroded area was circular in nature. The region on the specimen which was affected by the erosive wear but slightly outside of the main particle stream, commonly referred to as the “halo region”, was also circular in nature for the 90° impact. In the 30° impact, the eroded specimen displayed significantly different characteristics as the wear scar was oblique in nature. Also, the halo region was notably thinner around the region closest to the nozzle and became larger in areas away from it.

To model the erosive wear of particles striking a surface, the current framework was used. Particles were initialized in a column and traveled toward the surface during the simulation. Once particles impacted the surface, a wear formulation [64] was imparted to record the area where the particles would damage the surface. The damage a particle would do to the surface was based upon the particle’s indentation depth into the surface and the component of its velocity that was tangential to the surface. This relationship is displayed in Fig. 6.10.

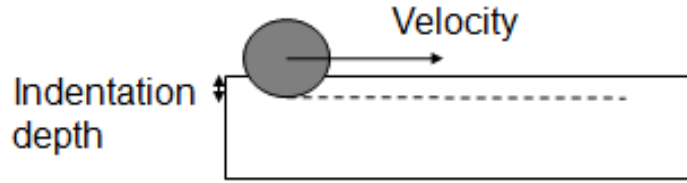


Fig. 6.10 Parameters used to calculate the material removal per particle in the erosive wear formulation

An image of the simulated particles striking the surface at a 30° impact angle is displayed in Fig. 6.11.

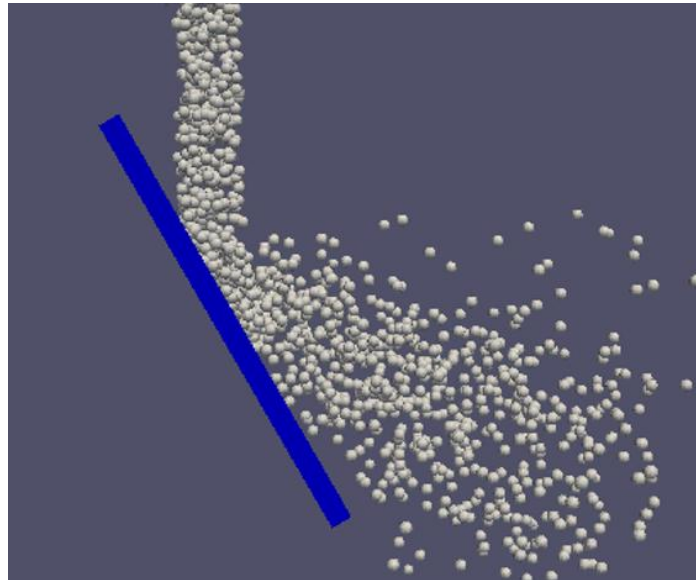


Fig. 6.11 Image of the simulated particles striking the surface at a 30° impact angle

To compare the results of this erosive wear simulation to the experiment, the surface of the computational test specimen was contoured by the degree of erosive wear experienced in that region. The results of this comparison are displayed in Fig. 6.12.

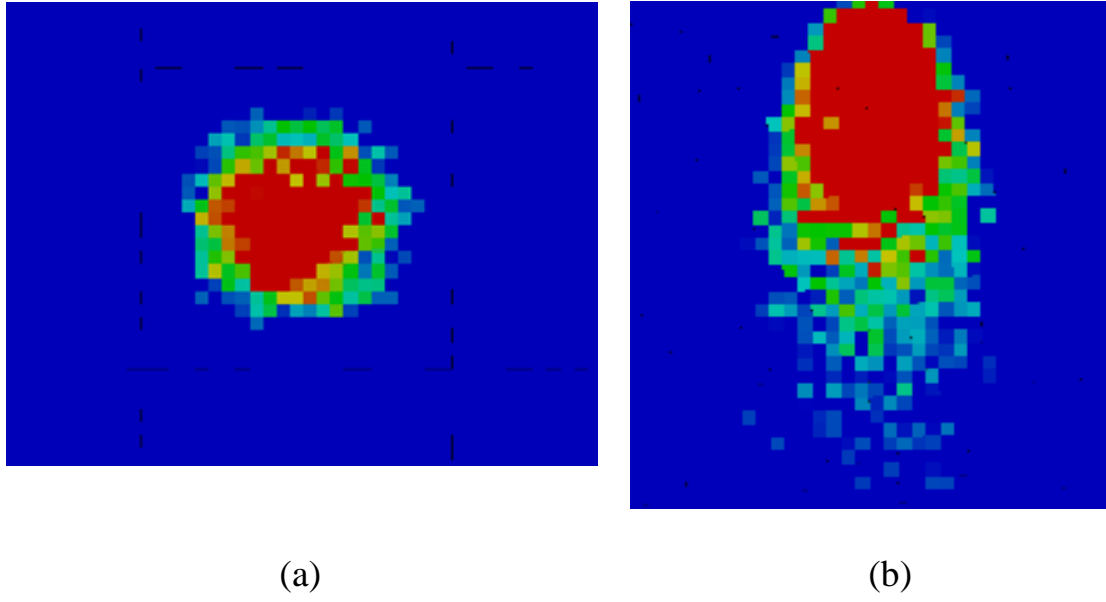


Fig. 6.12 Contour of wear scar generated from the computational framework (a) 90° impact angle (b) 30° impact angle

In Fig. 6.12, it can be seen that the results from the Eulerian-Lagrangian framework qualitatively match the results from the experiment shown in Fig. 6.9. For the 90° impact case, the halo region is concentric around the main wear scar just as is the case in the experiments. In the 30° impact case, the halo region is thin in the region closest to the nozzle and then fans out in other regions. This qualitative agreement suggests that the model is able to capture some of the physics which dictate the particle behavior in erosive wear scenarios.

For a quantitative comparison, the material properties of steel, aluminum, and acrylic were input into the Hertzian contact model to predict the indentation depth. The properties of silica were used in the DEM model to approximate the JSC-1AF lunar dust simulant. CFD was used to model the effect of the fluid (air) on the particles. The boundary conditions of the CFD domain are displayed in Fig. 6.13.

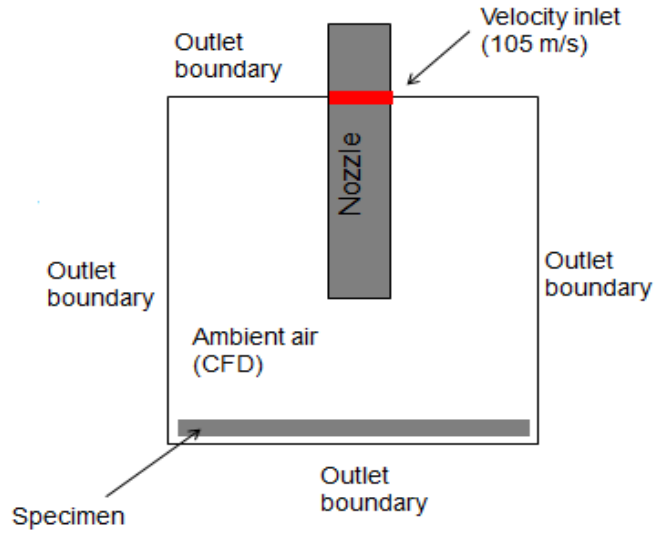


Fig. 6.13 CFD boundary conditions used in the erosive wear model

Though the mechanical properties of the materials, the particle sizes, and the velocities were set in accordance to the test conditions, the test domain and nozzle were reduced in size for the purpose of computational efficiency. The erosive wear predictions from the model for each test material were compared to the experiments at an impact angle of 90° . The results of this comparison are displayed in Fig. 6.14.

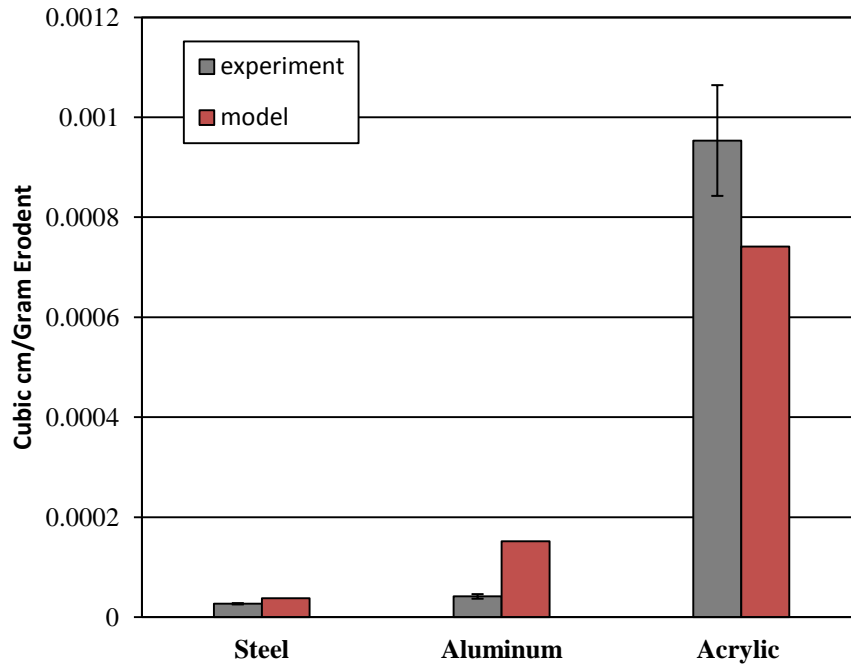


Fig. 6.14 A comparison of the model's prediction for erosive wear to the experiment

In Fig. 6.14, the results have been normalized by the amount of erodent striking the surface. It can be seen that there is very good agreement between the model's prediction of erosive wear and the experimental results. Such agreement suggests that the modeling framework can also be used for the quantitative prediction of erosive wear.

Chapter 7

Modeling Rotary Rock Drilling

During the drilling process, drill operators constantly adjust drilling parameters depending on a number of geo-tribological factors. The optimization of these parameters is typically based on trial-and-error field data from previous wells. As a step toward elucidating some of the underlying physics which affect the drilling process, the current work introduces a continuum-discrete approach which has the potential to predict rock wear rates. This model predicts how changes in rock strength, drilling fluid viscosity, drill bit angular velocity, and weight-on-bit affect the rate-of-penetration. Predictions from the model show qualitative agreement with experimental findings and field data.

7.1 Introduction to Rotary Drilling

To reduce drilling costs, petroleum companies seek to drill wells in the most efficient manner possible. Achieving this requires the optimization of various drilling parameters such as the drill bit type, the drilling fluid properties, the drill bit angular velocity and the weight-on-bit (WOB). However, correctly choosing these parameters depends on several key geological factors such as the type of formation being drilled and the formation pressure. The drill operators typically set these parameters based on data from the current well or data from wells drilled under similar conditions. In this work, a rotary drilling model is developed to elucidate some of the underlying physics which occur during well drilling. By integrating the effects of the drill bit, the drilling fluid, and the rock

formation into one computational framework, a tribological analysis of the drilling process can be performed. The current model shows promise at predicting the effect of various drilling parameters before the expensive drilling process has begun.

Various components of the rotary drilling process have been modeled by authors throughout the literature with some success. S. Kahraman found a strong correlation between the rate-of-penetration (ROP) in various formation types to the modulus ratio (the ratio of Young's modulus to the uniaxial compressive strength) [65]. Working from the assumption that the drill bit interacts with the rock primarily through a combination of cutting and frictional forces [66], Detournay et al. produced a rotary drilling model relating the specific energy to drilling strength [67]. Detournay et al. later published an update on this model which incorporates characteristics of the cutters and the ambient pressure in predicting the response of the drill bit. There have also been a collection of models which investigate the effect the drill string and drill bit vibrations will have on the rotary drilling process [68-70]. Efforts to model the complete rotary drilling process using continuum mechanics, as opposed to a discrete-continuum framework as is done in this work, have also been explored [71].

This current work is unique in that it introduces an integrated discrete-continuum framework to model the drilling process using discrete particle simulations. The overall objective of this work is to construct, test, and assess the framework's potential for studying rock drilling tribology in aqueous environments by employing the bonded-particle method (BPM) in concert with simple fluid mechanics. The model is based on first-principles and takes into account industry-relevant parameters to predict the time-evolving interaction of key drilling components. The model's prediction for the drill bit's

rate-of-penetration (ROP) is presented as these relevant drilling parameters are varied. The results from the model are shown to agree qualitatively with experimental findings and field data.

7.2 Rotary Drilling Modeling Methodology

The completion of deep and ultra-deep wells is the result of the interplay between a number of complex mechanical and chemical processes. However, most of the processes can be captured in the interaction between a few drilling components: the rock formation, the rock cuttings, the drill bit and the drilling fluid. In the current work individual models are presented for each of these components. They are then integrated into a computational model to simulate their effect on ROP.

7.2.1 Rock Particles and the Rock Formation

Data retrieved from drilling tests has revealed that the characteristics of the rock formation are an important factor in determining the ROP during drilling. The formation's mechanical strength[65, 72], porosity [73, 74], quartz content [73], anisotropy [73, 74], and degree of foliation[73] are some of the formation characteristics which can affect how efficiently it is drilled. In the current work, the rock formation is modeled as a network of discrete rock particles which have been bonded together to create the porous rock material. This technique, which is common in the geomechanics community, was chosen because it has the ability to naturally incorporate the aforementioned important factors influencing the drillability of rocks. The mechanical properties of the bonds connecting the particles which comprise the rock are altered to affect the macroscopic mechanical behavior of the rock. The spaces between bonded rock

particles represent rock porosity, and the density of the rock particles can be adjusted to approximate the density of the rock formation.

7.2.2 Modeling Rock Particles

Individual rock particles, which are bonded to create the rock formation, are modeled using the soft-body discrete element method (DEM) [37]. The trajectory of each particle is determined by the cumulative effect of forces acting on it through Newton's second law of motion. In the current model, particles are influenced by their collisions with other particles, collisions with domain boundaries and the viscous drag of the drilling fluid. The soft-body variation of DEM is used in which the majority of collisions occur over multiple time steps. The common spring-dashpot model, depicted in Fig. 3.1, is used to model particle-particle and particle-wall collisions. Currently only normal contact forces are considered, but shear forces can be incorporated using this same framework.

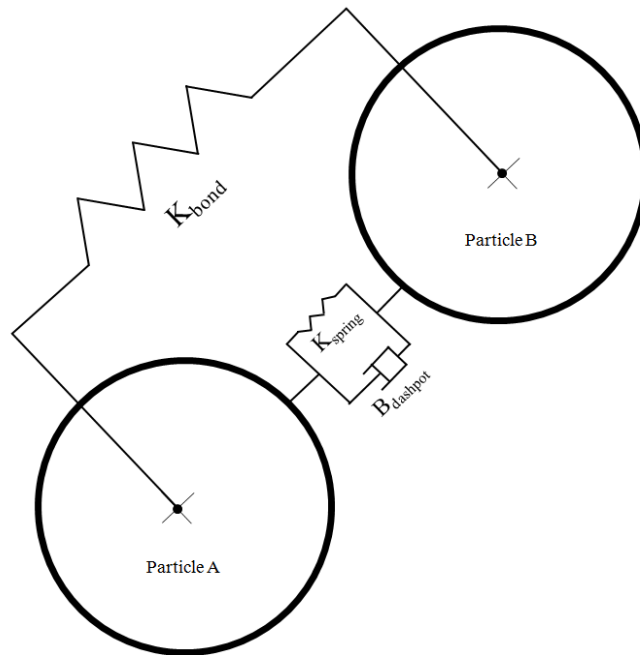


Fig. 7.1 The spring-dashpot model used in the discrete element method (DEM) for particle collisions along with the bond between particles used in the bonded-particle model (BPM).

Collisions occur when the distance between one particle and another particle or the domain boundary is less than one particle radius. The total force, $\mathbf{F}_{collison}$, imparted to a particle during a collision, described in Eq. (7.1), is a linear combination of two forces. The first is a repulsive force caused by the compression, \mathbf{U}_{spring} , of an idealized spring which occurs when the particles overlap. The second is a damping force proportional to the normal velocity, \mathbf{V}_n , between the particle and the object with which it is colliding. This damping force is introduced to capture the inelasticity of the collision.

$$\mathbf{F}_{collison} = K_{spring}\mathbf{U}_{spring} - \mathbf{V}_n B_{dashpot} \quad (\text{Eq. 7.1})$$

In Eq. (7.1) K_{spring} and $B_{dashpot}$, the spring and damping constants respectively, are specified depending on whether the collision is with other particles or with the boundaries. The numerical integration scheme used to update particle velocities and positions is the explicit Euler integration technique.

7.2.3 Modeling the Rock Formation

Modeling rock cutting is particularly difficult due to nonlinearities in the cutting process, the formation of and discontinuities introduced by cracks, and the anisotropic nature of some rocks. Thorough reviews of various proposed rock modeling and rock cutting methods have been conducted by several authors [75, 76] .

In the current work, a method is used based on the bonded-particle model (BPM) detailed by Potyondy and Cundall [77]. This approach, and variations of it, have been used in several other studies to model rock behavior [78-81]. In the BPM, DEM particles

are “cemented” together through the introduction of idealized mechanical bonds between particles. It is this collection of bonded particles that forms the rock. Applying loads to the rock, such as those imparted during tension/compression tests or rock cutting, stresses the bonds holding the particles together. Once the stress in these bonds rises to a predetermined ultimate strength, the bond is permanently broken, potentially generating a micro-crack in the material.

A challenge posed by this modeling technique is accurately specifying the micro-scale properties of particles and the bonds which hold them together, to produce the macro-scale mechanical behavior representative of the rock being modeled. Potyondy and Cundall [77] determined that macro-scale properties exhibited by rocks modeled in this way are sensitive to the DEM particle size, the distribution of DEM particle sizes, the ratio of normal stiffness to shear stiffness of the bonds cementing them together, the packing procedure used to generate initial particle locations and contacts, the ultimate strengths of the cement bonds, and several other properties. By thoughtfully selecting these parameters, and comparing the model to biaxial, triaxial and indirect tension (Brazilian) tests of actual rock, they were able to produce a BPM model which quantitatively matched the elastic modulus, E , Poisson ratio, ν , and unconfined compressive strength of Lac du Bonnet (LDB) granite. The model also qualitatively reproduced the behavior of the rock during failure in that internal cracking was exhibited before ultimate failure. However the model failed to predict the slope of the strength envelope and Brazilian test strength for the LDB granite. The authors suggested that creating small agglomerations of particles or “clumps” of particles may provide better agreement. In 2007, Cho et al. [78] developed such a clumped -particle rock model and

obtained excellent agreement with experimental findings for the failure envelope of both LDB granite and a weak synthetic rock material . Other methods to reconcile the micro-scale parameters to macro-scale rock testing are presented Wang and Tanon [80]. In their work, a numerical procedure is developed where the deviation between the behavior of the rock model and the behavior of the actual rock is minimized. To do so, an iterative sensitivity analysis is performed to find the optimum value of an objective function which is used to determine the effect micro-scale parameters have on the macro-scale rock behavior. Through this method, Wang and Tanon were able to obtain good agreement with experiments for rock deformability and rock strength properties. Finally, with specific relevance to the current work's focus on drilling, Rojek used a variant of the BPM to simulate the rock cutting process [79]. He found that the BPM was able to produce quantitative agreement with established analytical models in the prediction of the force required to cut rock. The success that these authors have had in using the BPM to model rock mechanics, make it an attractive technique for use in modeling the drilling process. Moreover, the BPM provides a natural mechanism to model the effect of rock cuttings and potentially rock porosity which are both significant aspects of well drilling.

In the current work's variation of the BPM, a collection of DEM particles are randomly seeded and allowed to settle under gravity into the domain (Fig. 2). Once the kinetic energy of these particles has dissipated, due to the damping effect of the dashpot described earlier, they are bonded together with linear springs. These bonds are more akin to the "contact bond" variation of the BPM than the "parallel bond" in that they only transmit normal forces between particle centers [77]. They do not transmit moments or

shear loads. A stiffness, K_{bond} , and an ultimate strength, F_{ult} , are specified for these bonds.

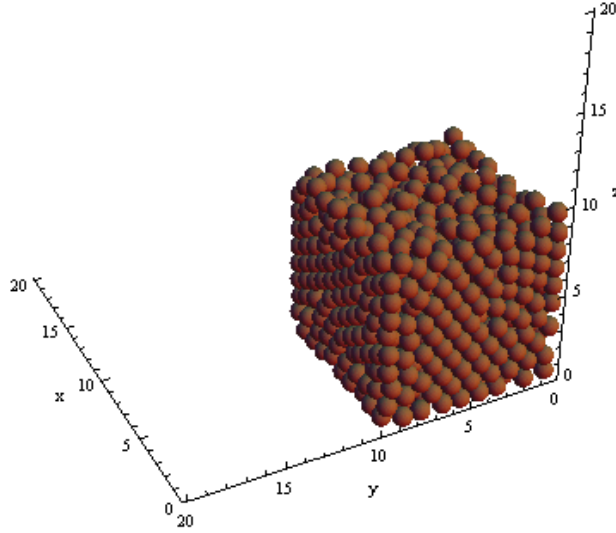


Fig. 7.2 Particles in the simulation domain creating the rock formation

External forces, such as those imparted by the drill bit, act on the rock particles to stress these bonds. The loads they exert have a magnitude equal to the product of the bond stiffness and bond extension, which are K_{bond} , and U_{bond} , respectively.

$$\mathbf{F}_{bond} = -K_{bond}\mathbf{U}_{bond} \quad (\text{Eq. 7.2})$$

When the force \mathbf{F}_{bond} , defined by Eq. (2), is greater than the specified ultimate force, F_{ult} , the bonds break potentially releasing rock particles, now rock “cuttings”, into the drilling fluid flow field. The negative sign in Eq. (7.2) is required depending on the local definition of extension or compression for U_{bond} . No attempt has been made to adjust the

micro-scale bond properties to match the mechanical behavior of known rock formations. While this task is important for a quantitative prediction of the drilling process, it will be performed in future developments since the goal of this work is to assess the ability of this framework to correctly capture the effect of various process parameters, in addition to the drilling fluid, on the overall drilling process. In the current work bond properties are selected and the effects of these properties, which determine the macro-scale rock parameters, are compared qualitatively.

For all particles, the domain boundaries are considered to be solid and rigid. The domain size is approximately 10 particle diameters in the x and y directions. This size was chosen to provide a sufficient number of particle bonds and to allow room for the drill bit. In the z direction, considerable distance, 75 particle diameters, is prescribed to allow space for rock cuttings to travel after being detached from the formation. To ensure that the rock formation does not undergo rigid body translation or rotation, the rock particles initially on the boundary are fixed in space for the duration of the simulation.

7.3 Modeling the Drill Bit

There are several different types of drill bits used in well drilling. Two of the most common rotary drill bits are roller cone bits and polycrystalline diamond compact (PDC) bits. The roller cone drill bit consists of rotating cones populated with teeth. The PDC bit is one structure on which cutters have been mounted. The modeling approach used in this work is intended to simulate the tribology of the PDC drill bit type. To model the drill bit, a collection of five special DEM particles are used. Four of these particles

represent the drill bit cutters and will be henceforth referred to as “cutter” particles. The fifth particle, out of plane from the other four, is important as it prevents rock cuttings from unrealistically travelling into space that would be occupied by the drill bit structure.



Fig.7.3 Drill bit particles compared to PDC drill bit (a) PDC drill bit [82] (*Copyright 2008, Society of Petroleum Engineers Inc. Reproduced with permission of SPE. Further reproduction prohibited without permission*) (b) Drill bit approximation using DEM particles.

7.3.1 Angular velocity of drill bit

As the drill bit rotates, force applied by the cutters acts to crush the rock into fragments. In the current model, the four cutter particles revolve at a specified angular velocity around a central drill bit axis. Their positions in the x-y plane are prescribed according to Eq. (3). Here, x_{cutter} , y_{cutter} , x_{bit} , y_{bit} represent the positions of the cutter particles and the drill bit center. At each simulation time step, the positions of these particles are updated.

$$x_{cutter} = x_{bit} + D_{bit} \frac{\cos(\omega_{bit} time)}{2} \quad (\text{Eq. 7.3a})$$

$$y_{cutter} = y_{bit} + D_{bit} \frac{\sin(\omega_{bit} time)}{2} \quad (\text{Eq. 7.3b})$$

The fifth drill bit particle, which is located on the central drill bit axis, is always positioned approximately one particle diameter above the average z position of the drill bit's four cutter particles. This particle occupies the volume that would normally be occupied by the drill bit structure in actual drilling.

7.3.2 Weight-on-bit

The weight-on-bit (WOB) is an important characteristic in drilling, since it is the thrust load applied to the drill bit. It results in a force pressing the rotating drill bit into the rock. To simulate this effect, each of the cutter particles have an equal force applied to them in the direction of cutting (i.e., the negative z direction). The total WOB is taken as the sum of these four loads on the cutter particles.

Though it is convenient to model the drill bit as a collection of particles, special attention needs to be given to the degrees of freedom of these particles in the z direction. Identical loads are applied to each of the cutter particles resulting in the reported WOB. However, the forces counteracting the WOB, such as contact with the rock formation, are not always equal. Therefore, the drill bit particles would have a tendency to move greatly out of plane. In reality, the drill bit structure itself would help to prevent this from happening as loads experienced by one of the cutters would be transferred through the drill bit structure to the other cutters. In the model, this effect is captured by introducing a set of

bonds between each cutter particle and the average z position of all four cutter particles. When a cutter particle is offset from the average z position of the cutter particles, it experiences a force in the z direction from these bonds proportional to its offset. This force can act to decrease the effective WOB for that cutter particle if it is at lower position than the average z position of all four cutter particles. It can also act to increase the effective WOB for that particle if it is at a higher z position than the average z position of all four cutter particles. However, if the particles are close to each other in the z direction, the offset from the average z position of all four particles is minimized and this force does not contribute to the cutting process. The average z position of the four cutter particles is an important parameter in the model and will be referred to as the “drill bit height” henceforth.

7.4 Modeling the Drilling Fluid

Drilling fluids are typically non-Newtonian suspensions composed of a base fluid, solid particles or clays, and several additives such as barite, gum polymers, and surfactants to increase the drilling fluid performance. The drilling fluid is critical to the drilling process. From the surface, it is pumped down the drill string and forced from outlets in the drill bit. Depending on the formation pressure and drilling fluid characteristics, some of it will invade the porous rock formation. In most cases, much of the drilling fluid travels back up the borehole in the annular region between the well walls and the drill pipe. As discussed thoroughly by Darley and Gray [27], the drilling fluid performs several key operations. However, one of the most important is its ability to carry rock cuttings away from the cutter interface and up the borehole. Drag from the drilling fluid and the pressure gradient it causes act to lift the rock cuttings so they do not impeded

drilling progress. The current model only investigates the effect of the drilling fluid's efficiency at performing this task of removing cuttings from the interface between the bit and the rock. Thus, only the flow of the drilling fluid returning to the surface is modeled. In this work, the drilling fluid is modeled by imposing a constant flow field in the domain in the direction opposite to drilling. This flow field represents the flow of the drilling fluid as it returns to the surface. The constant velocity of the flow field is termed W_{fluid} to indicate the velocity of the drilling fluid.

7.5 Modeling the Rock-Fluid Interaction

It is known that a particle immersed in a fluid can experience a number of forces such as drag, Saffman, Magnus, and hydrodynamic pressure forces [83, 84]. However, for simplicity, the fluid's effect on the rock and rock cuttings is modeled as only a drag force, which causes the rock cuttings to move based on fluid velocities at the particle center. Assuming spherical particles, a Stokes drag force is used to influence particle velocities based on the fluid velocity field. The authors acknowledge that assuming a Stokes drag relationship for this model may not be accurate for various rock cuttings sizes and shapes, drilling fluid viscosities, and the complex conditions which occur during oil drilling. However, as this work is intended to explore the feasibility of this model to capture the effect of industry-relevant rotary drilling parameters, the use of Stokes drag was chosen for simplicity. Its applicability must be examined in future works. As the flow field is imposed in the upward direction (opposite the direction of drilling), Stokes drag is only calculated in the z direction in accordance with Eq. 7.4. In Eq.7.4, F_{drag} , η , and a , represent the drag force in the z direction, the fluid viscosity, and the particle radius,

respectively. The other variables, w_{fluid} , and $w_{particle}$ define the fluid's velocity in the z direction and the particle's velocity in the z direction respectively.

$$F_{drag} = 6\pi\eta a(w_{fluid} - w_{particle}) \quad (\text{Eq. 7.4})$$

During actual drilling, the porous rock can act as a “sink” for the drilling fluid because it may absorb the drilling fluid before it can return to the surface. The absorption of the drilling fluid into the rock is unwanted because it will reduce the flow of drilling fluid carrying rock cuttings to the surface. In actual drilling, there are a number of engineering solutions which are employed to decrease the porosity of the wellbore. The first solution is that sand and clay are added to the drilling fluid so that as the drilling fluid flows past the rock, the sand and clay fill the pores in the rock decreasing the porosity of the wellbore walls. This helps to prevent the loss of drilling fluid into the rock. The second is that steel pipes are used to line the wellbore walls which effectively reduce the porosity of the wellbore to zero.

This interaction between the drilling fluid, the pores of the rock, the drill bit, and the steel pipes is very complex. The current model does not address many of these complexities. However, when the proper engineering solutions are in place (sand and clay clogging the pores of the rock and steel pipes used in the wellbore), the result is that drilling fluid returns to the surface and carries with it rock cuttings. In this work, it was assumed that those engineering solutions were working and the drilling fluid was serving its primary purpose to remove rock debris from the interface.

7.6 Units and Normalization

Modeling the drilling process for fossil fuels is inherently challenging due to the different scales involved. For instance, a wellbore may extend several kilometers into the surface of the earth while the actual rock crushing, caused by the drill bit, can occur over only a few millimeters. When modeling applications with such disparate scales, it is common to non-dimensionalize the results. In this section, the characteristic values used to non-dimensionalize the results from the model are described.

Because this work seeks to elucidate the effect of macroscopic drilling parameters, such as weight-on-bit, from the perspective of a collection of discrete grains which comprise the rock, it was determined that the length scale for this work would be the size of the rock grain. As such, the diameter of one grain was used to normalize all lengths to determine the non-dimensional length unit, L^* . No attempt to match the mechanical properties of the rock used in this study to a specifically known rock type was performed. Additionally, scaling all of the lengths by the size of a single rock grain makes it such that only relative sizes and distances are important in this work. However, to provide the reader with an idea of the scale of the scenario simulated, Table 7.1 lists typical grain sizes of sandstone and granite rocks which are two of the most commonly simulated rocks using the BPM. It can be seen in Table 7.1 that the grain sizes for these rocks range from approximately 0.1 mm to 1.8 mm in diameter.

Table 7.1 Typical grain sizes of sandstone and granite rocks

| Rock type | Grain size of rock (diameter) | Source |
|-----------------------|-------------------------------|------------------------------|
| Vosges sandstone | 0.1 mm – 0.4 mm | Rizo, 2010 [85] |
| Red sandstone | 0.3 mm – 0.8 mm | Yang et al., 2012 [86] |
| Westerly granite | 0.1 mm (average) | Hazzard and Young, 2000 [87] |
| Lac du Bonnet granite | 1.1 mm – 1.8 mm | Cho et al., 2007 [78] |

Besides the size of the rock grains, another length scale involved in rotary drilling is the size of the drill bit. For example, drill bits used in rotary drilling may range in diameter from 6.5 inches to 11 inches (165 mm to 279 mm) [88]. Though the size of the drill bit compared to the rock grains may affect the modeling of the drilling process, it was decided that for this study, the focus was to develop a model that can capture how changes in rock strength, drilling fluid viscosity, drill bit angular velocity, and weight-on-bit (WOB) affect the rate-of- penetration (ROP). The computational resources required to model the actual size ratio between the drill bit and the rock grain was prohibitive. As a result, further studies would need to be performed to understand the effect of this ratio in the prediction of quantitative rates-of-penetration.

The non-dimensional mass unit, m^* , was determined by normalizing all masses by the mass of one of the particles. The non-dimensional time unit, t^* , was determined by dividing the particle diameter by the velocity of the fluid leaving the wellbore. The characteristic values used to non-dimensionalize these basic units of length, mass, and time are summarized in Table 7.2. In Table 2, a is the diameter of a single particle, $m_{particle}$ is the mass of a single particle, and W_{fluid} is the fluid velocity in the domain.

Table 7.2 Characteristic values used for non-dimensionalization

| Dimension | Characteristic value |
|-----------|---|
| Length | $\bar{L} = 2a$ |
| Mass | $\bar{m} = m_{particle}$ |
| Time | $\bar{t} = \left(\frac{2a}{W_{fluid}} \right)$ |

As this modeling work was primarily considered a feasibility study, the magnitude of the parameters has not yet been reconciled with actual drilling data. Instead, a comparison of the relative effect of changes in these parameters is presented. The characteristic values, \bar{L} , \bar{m} , and \bar{t} presented in Table 2, are used to non-dimensionalize the quantities that will be of interest later in this paper. In the following sections, these non-dimensional terms, such as F_{ult}^* and ROP^* are also denoted with an asterisk, “ $*$ ” and are summarized in Table 7.3.

Table 7.3: Non-dimensionalization of terms

| Dimension | Non-dimensionalization |
|-----------|---|
| Length | $L^* = \frac{L}{\bar{L}}$ |
| Mass | $m^* = \frac{m}{\bar{m}}$ |
| Time | $t^* = \frac{t}{\bar{t}}$ |
| ROP | $ROP^* = \frac{ROP}{\bar{L}/\bar{t}}$ |
| WOB | $WOB^* = \frac{WOB}{\bar{m} \frac{\bar{L}}{\bar{t}^2}}$ |
| F_{ult} | $F_{ult}^* = \frac{F_{ult}}{\bar{m} \frac{\bar{L}}{\bar{t}^2}}$ |
| ω | $\omega^* = \frac{\omega}{\frac{1}{\bar{t}}}$ |
| η | $\eta^* = \frac{\eta}{\frac{\bar{m}}{\bar{L}\bar{t}}}$ |

It should be noted that the lack of experimental validation for the rock material make the current version of this model valuable for qualitative comparison. As a result, efforts to non-dimensionalize the experimental results from the validation graphs in this work, just

to compare them to the non-dimensional results from the current model, will not be beneficial.

Finally, there were two criteria for determining the computational time step for this model. The first was that the time step was a fraction of the period of an un-damped single degree-of-freedom (DOF) oscillator formed by the mass-spring system of the particle. A similar criterion has been used as a stability condition in DEM modeling in the previous works [35, 89]. The second was that for a given particle velocity, a particle did not travel more than a small fraction of a particle radius within a single time step. The latter was enforced to prevent artificially large forces between particles due to the time discretization.

7.7 Rotary Rock Drilling Results and Discussion

In this section the results of the model are presented along with various comparisons to experimental and field data. Independent case studies were performed to assess the effect of formation strength, weight-on-bit (WOB), drilling fluid viscosity, and drill bit angular velocity on the drilling process. All code was developed in-house and written in the C++ computing language. Simulations were run on a PSSC Labs PowerWulf computing cluster. Each simulation required approximately 5 hours of real time to complete. As it is an important metric in drilling, ROP was used to evaluate the effect of the parameters varied during each case study.

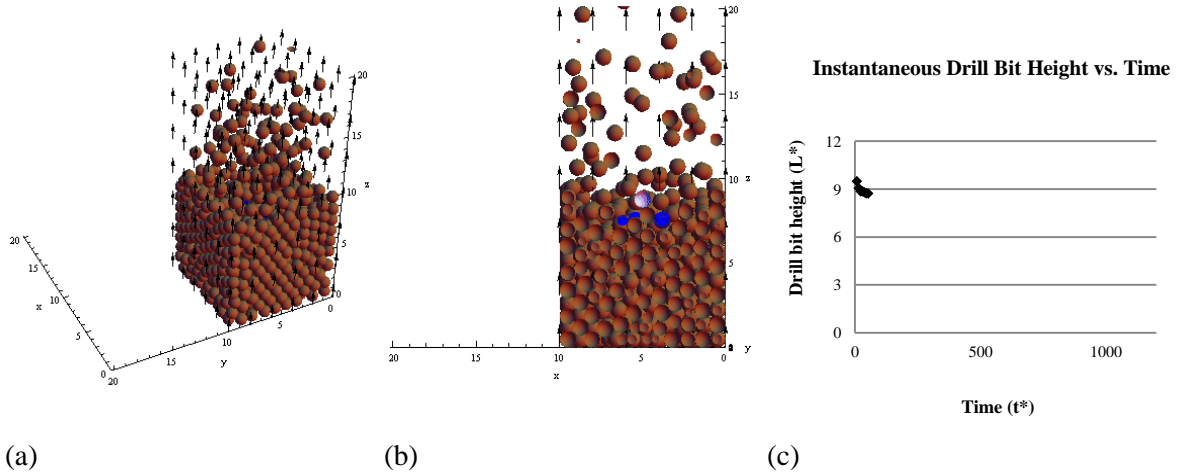


Fig. 7.4.1 Snapshot of simulation at $t^* = 52.5$. (a) Trimetric view of simulation domain. (b) Cross-section view of simulation to show detail of rock cutting. (c) Graph of instantaneous drill bit height vs. time data.

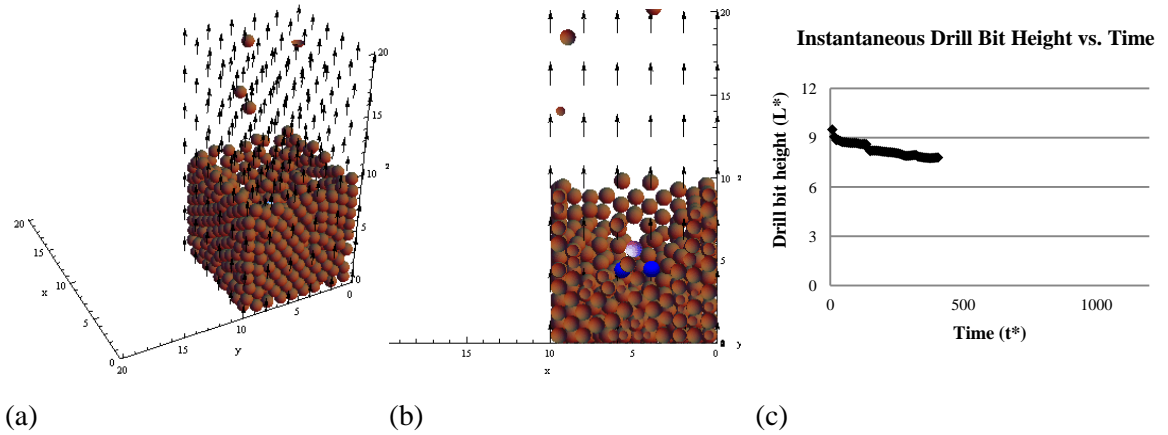


Fig. 7.4.2 Snapshot of simulation at $t^* = 405$. (a) Trimetric view of simulation domain. (b) Cross-section view of simulation to show detail of rock cutting. (c) Graph of instantaneous drill bit height vs. time data.

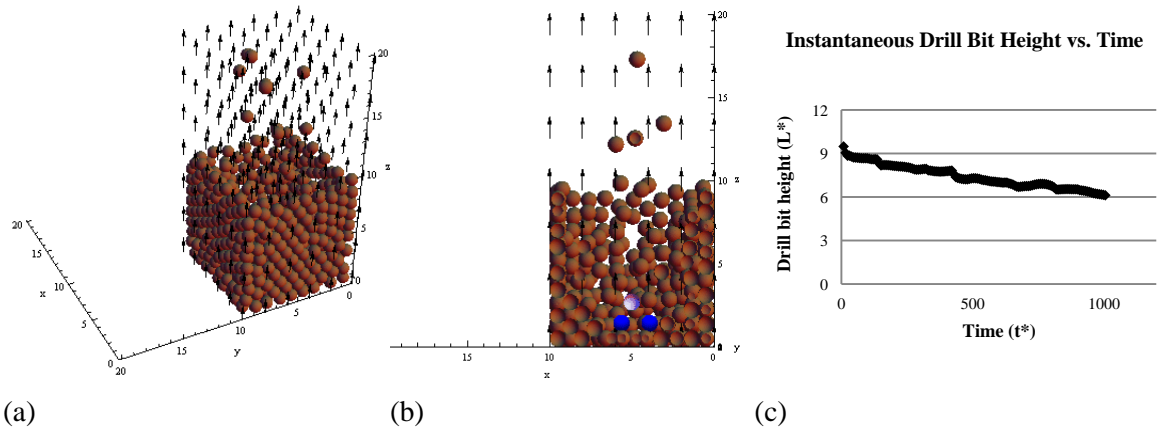


Fig. 7.4.3 Snapshot of simulation at $t^* = 1005$. (a) Trimetric view of simulation domain. (b) Cross-section view of simulation to show detail of rock cutting. (c) Graph of instantaneous drill bit height vs. time data.

7.7.1 The Effect of Rock Formation Material on Rate-of-Penetration

To vary the formation material, the ultimate strengths (which are evaluated as force in the DEM framework) of the bonds which comprise the rock, F_{ult} , are adjusted. To obtain the ROP, the height of the drill bit, taken as the average height of the four cutter particles, is recorded as the simulation evolves. Using linear regression, a relationship between the drill bit height and simulation time was established. The slope of this line was then taken as the drill bit's average ROP. In Fig. 5, the drill bit height vs. time is plotted for various values of F_{ult} . It can be seen that the trajectory of the drill bit is affected by changes in the rock formation. As these bond strengths are increased, the ROP is decreased.

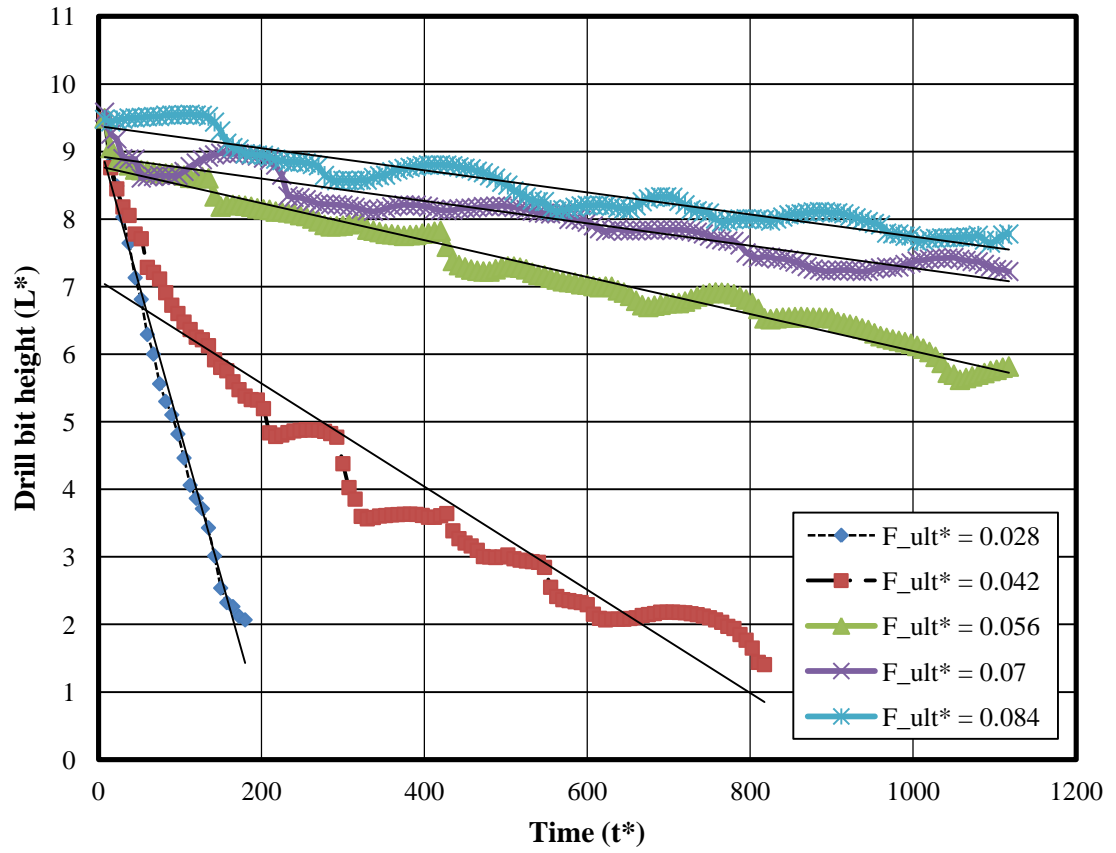


Fig 7.5 The drill bit height vs. time for various bond ultimate strengths, F_{ult}

This phenomenon can be seen more clearly in Fig. 7.6a where the ROP is examined. In Fig. 7.6 the magnitude of the slopes of the lines in Fig. 7.5 (ROP) are plotted against the ultimate strength F_{ult} . It can be seen that for increasing values of F_{ult} , the drill bit cuts the rock much slower. This is because the bonds in the rock become harder for the drill bit to break with increasing F_{ult} .

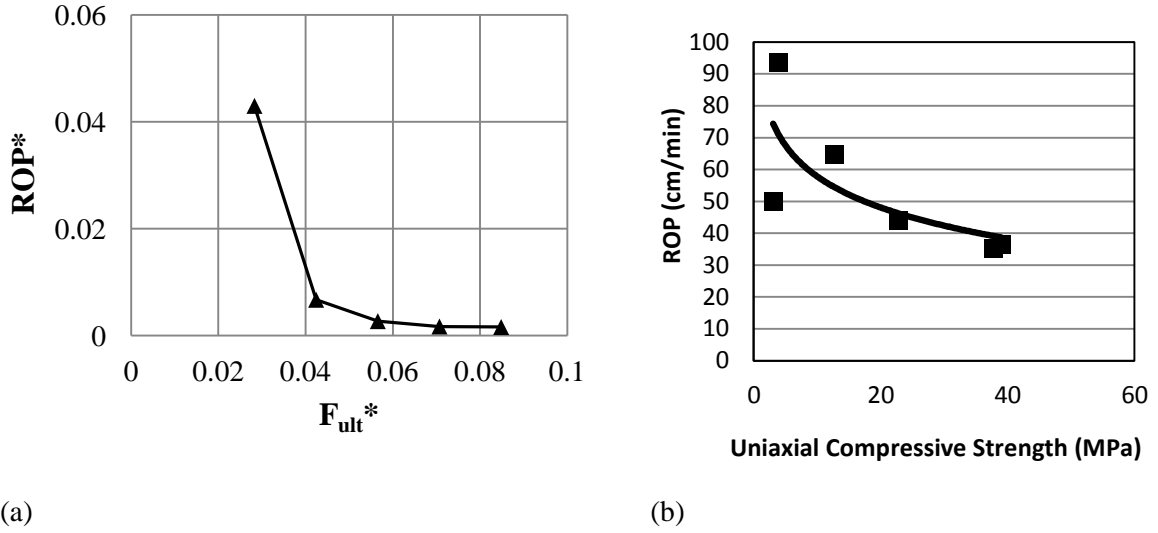


Fig 7.6 Comparison with experimental data for the effect of rock properties on rate-of-penetration (ROP) (a) results from the current model (b) results from drilling experiments reproduced from Howarth, 1987 [90]

Howarth conducted rotary drilling experiments to determine the ROP for various rock formations [90]. The uniaxial compressive strength for the formations was also determined and both quantities are presented in Fig. 7. 6b. It can be seen in Fig. 6b that as the uniaxial compressive strength of the rock increases, the ROP decreases. Though the current work does not reconcile the macro-scale uniaxial compressive strength of the rock to the bond strengths studied, it is reasonable to assume that as the ultimate strength of the bonds increases, the uniaxial compressive strength also increases. The results of Howarth depict a variation in ROP in a similar fashion to that predicted by the current model. Such qualitative agreement suggests that the model is able to capture the effect of changing rock properties. It is believed that a refinement of the bonding properties of the rock formation would result in quantitative agreement between the experimental and modeling results, as well.

7.7.2 The Effect of Weight-on-Bit on Rate-of-Penetration

The WOB is the load at which the drill bit is forced into the rock formation. It affects how much energy is applied to the rock during cutting. The current model was used to assess how the WOB affects the cutting process. To do so, increasing weight was applied to the cutter particles. The average ROP was determined for these cases and is presented in Fig. 7.7.

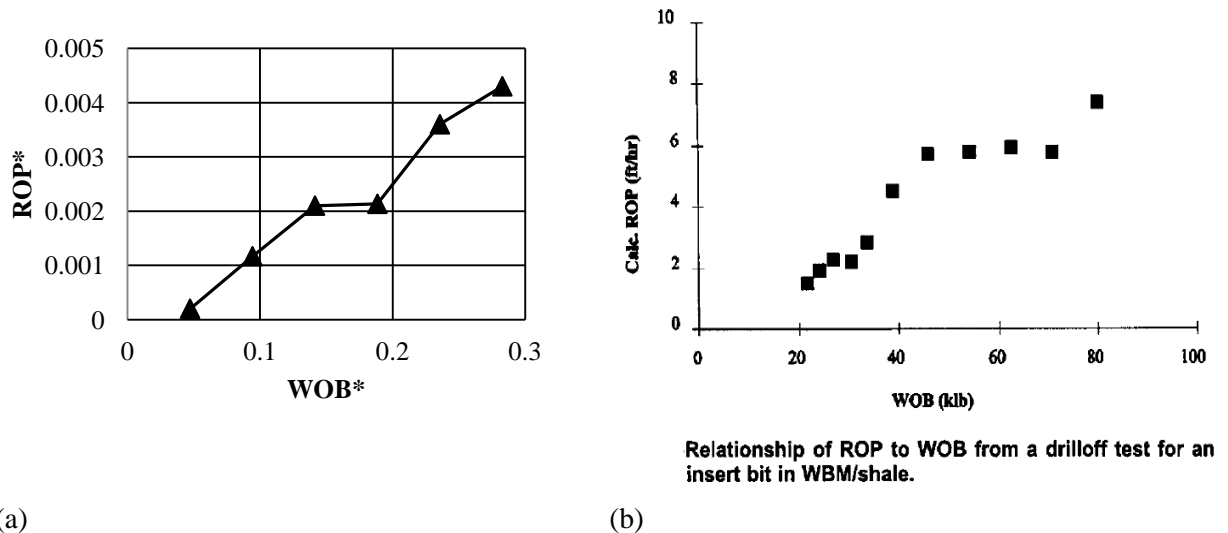


Fig 7.7 Comparison with experimental data for the effect of weight-on-bit (WOB) on rate-of-penetration (ROP) (a) results from the current model (b) field data from M.J. Fear, 1999 [91] (Copyright 1999, Society of Petroleum Engineers Inc. Reproduced with permission of SPE. Further reproduction prohibited without permission)

Increases in WOB result in more load applied to the particles which comprise the rock. This increase in load stresses the rock bonds causing them to break. When the bonds break, the rock particles are released and become rock cuttings (debris) which are

transported out of the cutting interface by the drilling fluid. These results are compared to the results of drilling data presented by Fear [91]. In Fig. 7b field drilling data is presented showing the ROP vs. WOB. It can be seen in Fig. 7b that increases in WOB cause increases in the ROP for well drilling. The experimental results of Miller and Ball also depict an increase in ROP vs. WOB [92]. Qualitatively, the current model shows the same trend—higher WOB leads to higher ROP. In Fig. 8 the drill bit height vs. time is presented for the extreme cases of $WOB^* = 0.047$ and $WOB^* = 0.283$. It can be seen here that the relatively high WOB^* of 0.283 produces a clear drill bit penetration. In contrast, the relatively low WOB^* of 0.047, is not able to penetrate the surface. The undulating motion of this curve is caused by the drill bit raising and lowering as it rotates on the surface of the rock formation. A minimum WOB threshold to initiate penetration has been found in experimental drilling as well [88].

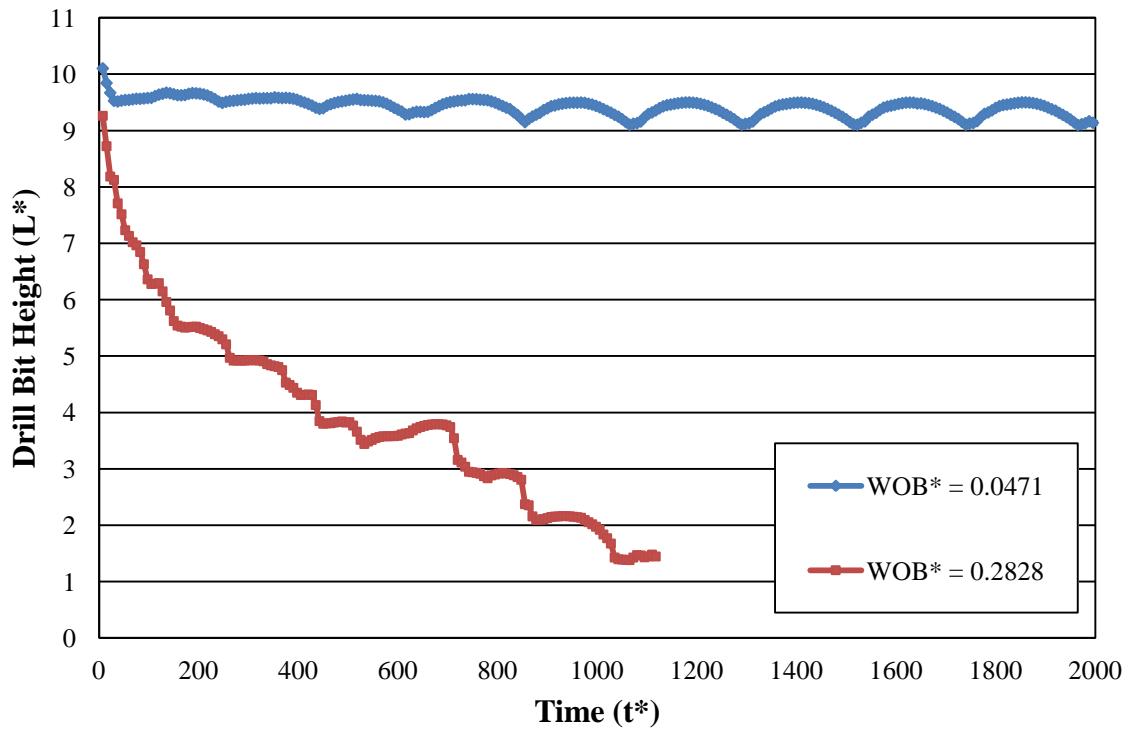


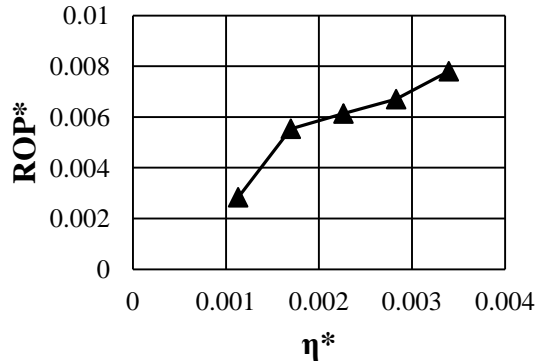
Fig. 7.8 Drill bit height vs. time displaying the effect of low weight-on-bit (WOB)

7.7.3 The Effect of Drilling Fluid Viscosity on Rate-of-Penetration

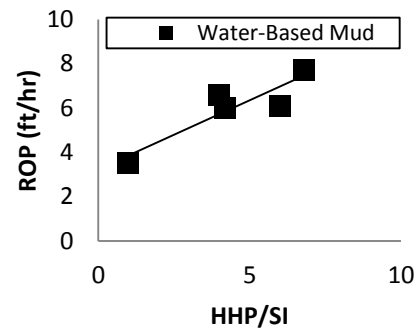
Though many drilling fluids are non-Newtonian, the current model assumes that the drilling fluid is Newtonian in that its effective viscosity is maintained constant for each simulation to assess the effect of varying this parameter independently. Figure 9a shows the model's prediction of the effect of varying viscosity on ROP, where increases in viscosity result in increases in ROP.

This is believed to occur because increases in viscosity result in higher drag forces on the rock cuttings. Higher drag on the rock cuttings means that the drilling fluid can more easily remove them from the cutting interface. Since there is greater effectiveness of the

drilling fluid at cleaning the interface between the drill bit and rock, there are fewer rock cuttings to potentially impede the path of the drill bit. Because the effect of the drilling fluid to remove rock in actually rotary drilling is minimal, the viscosity in the model was kept low enough and the bond strength between particles was kept high enough, so that the drilling fluid itself did not significantly detach particles from the rock. It still required that the drill bit work to detach rock particles. However, once the particles were detached, the forces from the drilling fluid could remove the particles from the interface.



(a)



(b)

Fig. 7.9 (a) Rate-of-penetration (ROP*) vs. drilling fluid viscosity, η^* (b) For Comparison, field data on the HHP/SI reproduced from M.J. Fear, 1999 [91]

For comparison, drilling field data reported by Fear [91] is provided in Fig. 9b. Because drilling fluids are typically non-Newtonian, a comparison of ROP vs. drilling fluid viscosity is difficult. However, the most closely related input parameter during drilling, which was found in the literature by the authors, is the hydraulic horse power per square inch (HHP/SI). This describes how much power is being used to circulate the drilling

fluid through the system and is typically related to the effectiveness of transporting rock cuttings. Though there are other drilling fluid parameters that will affect the HHP/SI, frictional losses of the drilling fluid as it flows in the annular region between the borehole walls and the drill pipe contribute to the resultant HHP/SI. Therefore, the results of varying the model drilling fluid's viscosity are compared to varying HHP/SI in actual drilling. It can be seen in Fig. 9b that as the HHP/SI increases so does the ROP. Though the viscosity was varied in the current model (Fig. 9a), phenomenologically the model's prediction and the results presented by Fear in Fig. 9b agree. Both are an indication that as the drilling fluid becomes more proficient at cleaning the bit/rock interface, the ROP will increase. To better understand the model's prediction of increased cuttings transport with higher fluid viscosities, the average number of particles transported from the wellbore to the surface for a given time interval, t^* , was investigated. This quantity, referred to as the cuttings ejection rate (CER) was calculated for various drilling fluid viscosities.

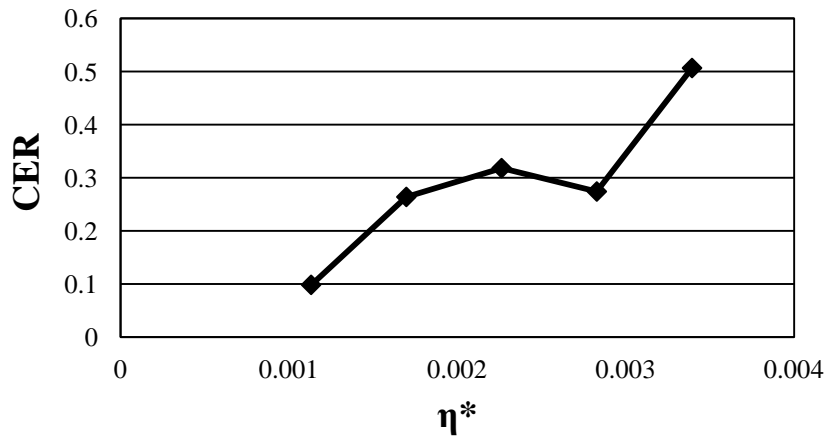
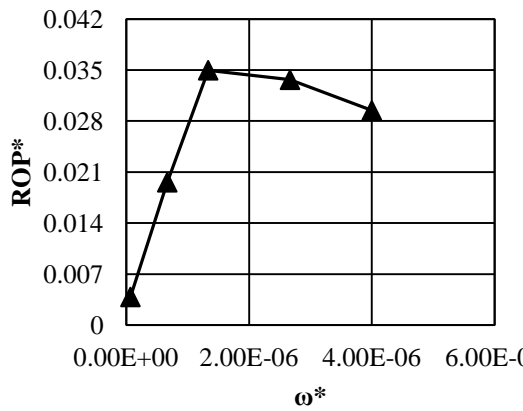


Fig. 7.10 The average number of rock cuttings leaving wellbore per unit time vs. viscosity

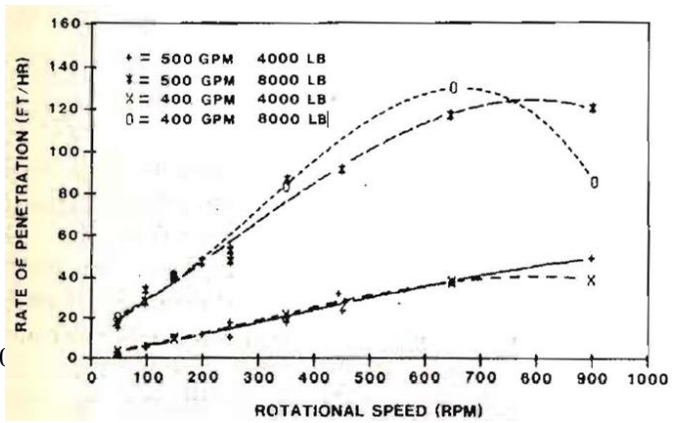
In Fig. 7.10 the effect of varying viscosity can be seen on the CER. The overall trend is that as drilling fluid viscosity increases, so does the average number of particles leaving the wellbore for a given time interval t^* (CER). This is an indication that increases in fluid viscosity generally results in better cuttings transport. However, the highly nonlinear nature of this curve warrants further investigation in future work.

7.7.4 The Effect of Drill Bit Angular Velocity on Rate-of-Penetration

The rotation of the drill bit acts to crush the rock during the drilling process. From the surface, the torque on the bit is prescribed resulting in a drill bit angular velocity which affects the ROP. In the current model, the angular velocity of the drill bit was adjusted to determine its effect on the drilling process. To do so, the angular velocity, ω , was varied in accordance with Eq. (3). This resulted in changes of the speed of revolution of the four cutter particles around the central drill bit axis. The results of this study can be seen in Fig. 11.



(a)



(b)

Fig 7.11. (a) Rate-of-penetration (ROP*) vs. angular velocity, ω^* (b) For comparison, drilling test data from A.D. Black, 1986 [88] (*Copyright 1986, Society of Petroleum Engineers Inc. Reproduced with permission of SPE. Further reproduction prohibited without permission*)

Initially the model predicts that the ROP will increase with increasing angular velocity. However, a point is reached around $\omega^* = 1.33 \times 10^{-6}$ where increasing angular velocity results in decreased ROP. This trend is in agreement with several of the PDC drilling tests performed by Black [88] presented in Fig. 11b. Black suggested that the reason for the decrease in ROP at high angular velocity could be because of inadequate bit cleaning. It has also been reported that drilling at high angular velocities can result in a decrease in torque due to a phenomenon called “bit-bounce” [70, 88]. During bit-bounce, the drill bit makes intermittent contact with the rock formation. To better understand the phenomenon responsible for the current model’s prediction, the drill bit height was plotted for several angular velocities and is presented in Fig. 12.

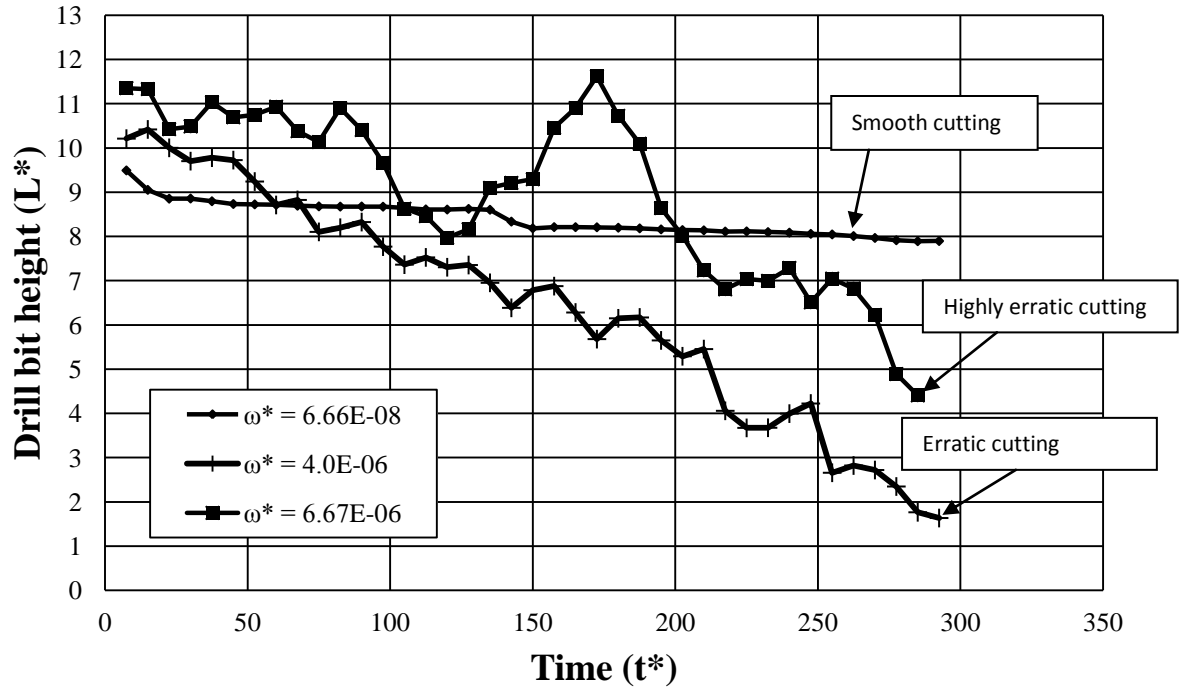


Fig. 7.12 Drill bit height vs. time displaying the effect of angular velocity

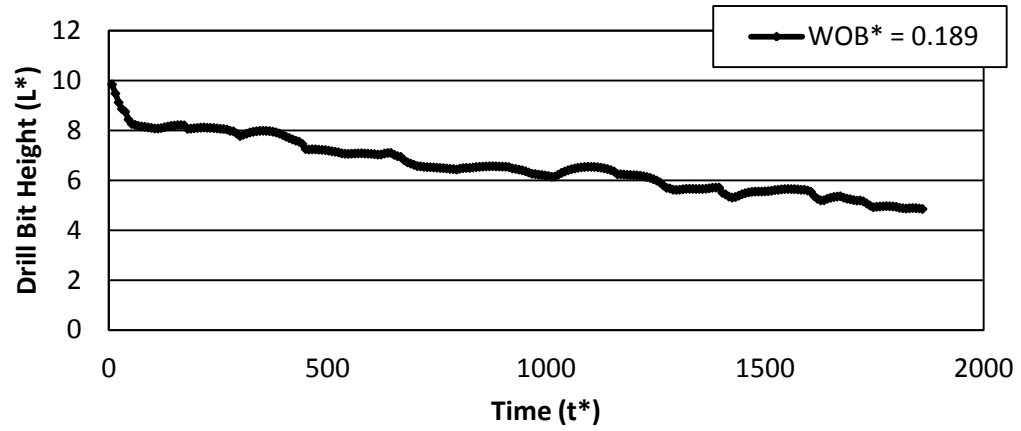
As shown in Figs. 11 and 12, the current model predicts smooth cutting for low angular velocities characterized by high ROP. However for larger angular velocities, the drill bit does appear to “bounce” as is characterized by the erratic up-and-down motion. Experimental evidence suggests that higher angular velocities can reduce the stick-slip phenomenon and lead to smoother drilling under certain conditions. However, it is also known that as angular velocity of the drill bit increases, excitations can develop in the drill string leading to bit-bounce. The difference between these outcomes is a function of the drill string dynamics and the rock properties [69]. The erratic motion predicted by the current model agrees with the latter observation that increased angular velocity leads to increased bit-bounce. In the current model, at the high angular velocity of 6.67×10^{-6} , the drilling becomes more erratic and the bit-bounce is predicted. The current model’s sensitivity to the factors which contribute to bit-bounce is important because of the effect

these factors have on ROP and the fact that bit-bounce has been shown to lead to premature bit wear [68].

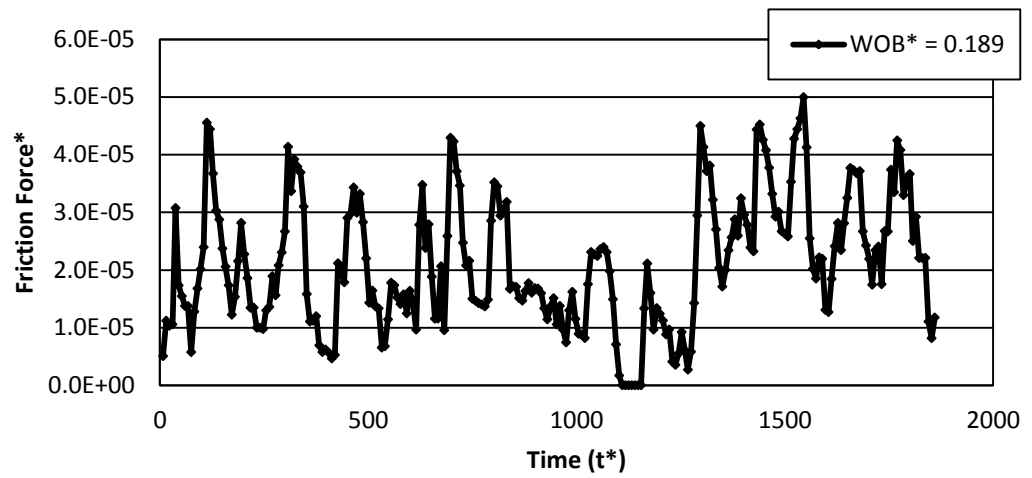
7.7.5 Estimating the Friction between the Drill Bit and the Rock Formation

During drilling, a torque must be supplied to the drill bit to overcome the resistance to its motion. The resistance is caused by a number of phenomena such as the shear stress imparted on the bit by the drilling fluid and the force of the drill bit contacting the rock. In this work, the force of resistance due to the contact of the drill bit with the rock is considered to be a global friction force at the bit-rock interface.

To calculate this friction force, the force on the cutter particles, from contact with the rock, is decomposed into a normal and tangential component to the drill's circumference. The tangential forces which act opposite to the drill bit's direction of motion are considered to be friction forces. These friction forces were studied for two different WOBs. The trajectory of the drill bit for these WOBs is presented in Fig. 13 and Fig. 14.

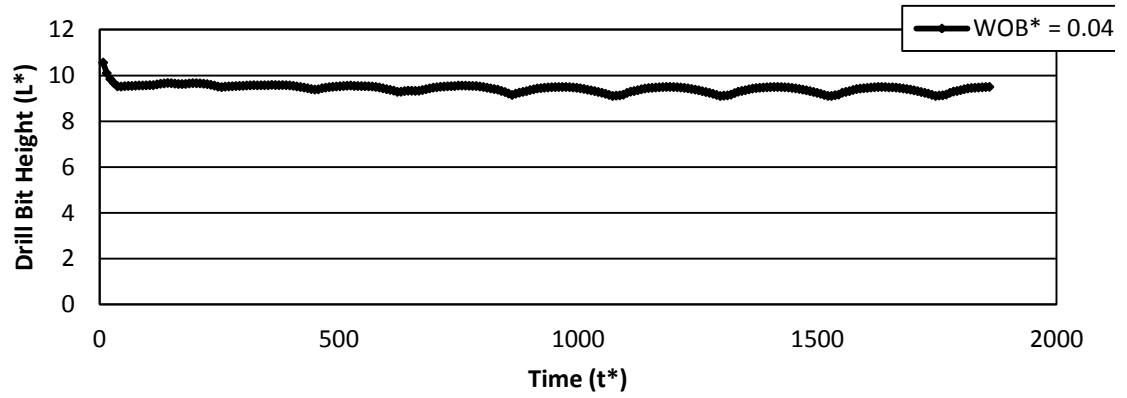


(a)

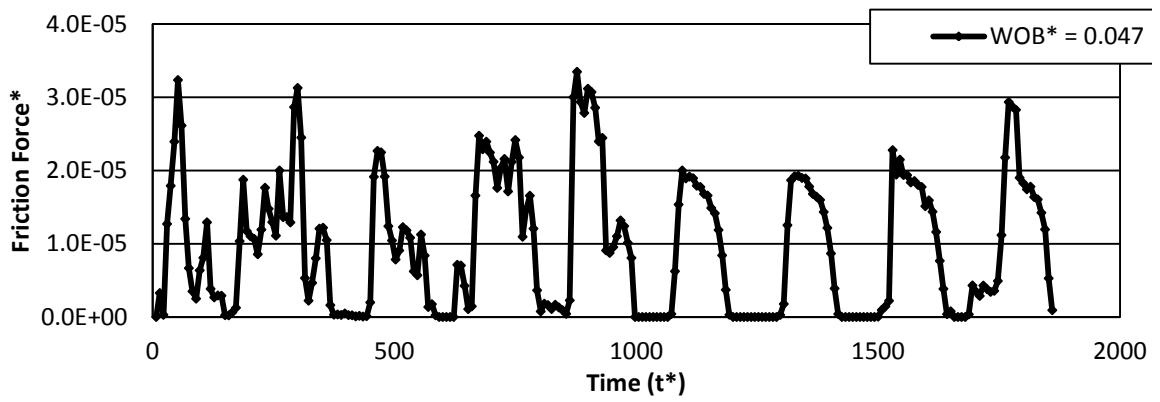


(b)

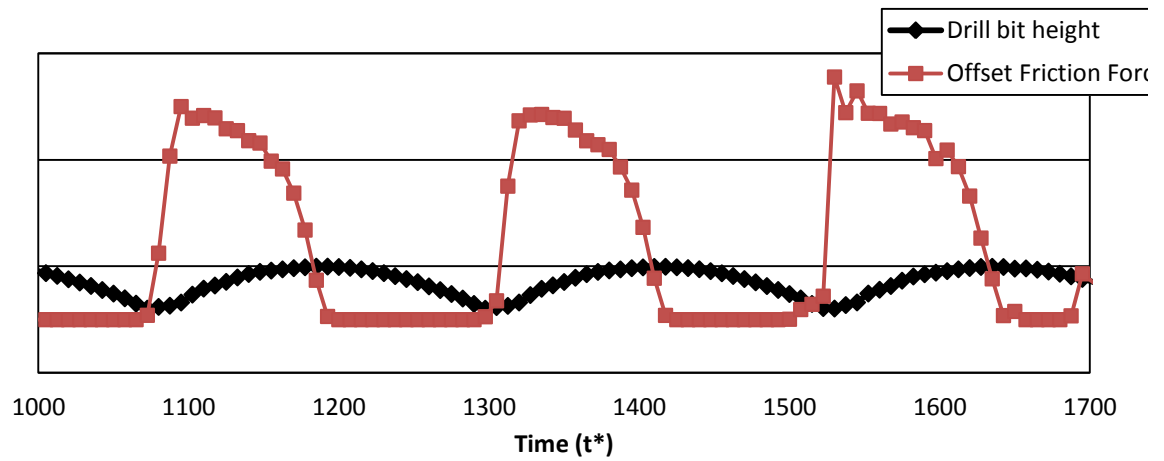
Fig 7.13 (a) Drill bit height vs. time for weight-on-bit (WOB^*) at 0.189 (b) Friction forces experienced by drill bit for WOB^* at 0.189



(a)



(b)



(c)

Fig 7.14 (a) Drill bit height vs. time for weight-on-bit (WOB^*) at 0.047 (b) Friction forces experienced by drill bit for WOB^* at 0.047 (c) Detail view of drill bit height

with the friction forces superimposed.

It can be seen in Fig. 7.13 that as the drill bit cuts the rock with a WOB* of 0.189, the drill bit experiences friction forces. However, in Fig. 7.14 the WOB* is only 0.047. As discussed in section 3.2, this WOB* is too low to effectively cut the rock and the drill bit undulates on the surface. The friction forces displayed in Fig. 14b correspond with this phenomenon. In Fig. 7.14c the friction force has been scaled and offset so that it can be viewed with the drill bit height. As the drill bit rotates on the surface below the weight threshold necessary to initiate cutting, it rises and falls due to the surface roughness. In this scenario, the bit acts similar to a stylus tip on a surface profilometer, which uses very low loads to trace out the profile of a surface rather than causing surface damage. When the cutter particles rotate over a low-spot on the rock, the WOB forces the bit downward. During this time, there is no friction on the bit because it is falling to the surface. As the drill bit rotates, it moves over high rock particles, akin to macro-asperities, on the rock. During this time the drill bit collides with the rock particles causing a sharp increase in the friction. The contact force from colliding with high-spots on the rock imparts an upward force and a friction force on the drill bit. The drill bit accelerates upward because the WOB is too low to overcome this reaction. After rotating past these high points, the contact force from the rock and the friction drop to zero and the drill bit begins to fall again.

The differences in the friction vs. time curves between a drill bit that is effectively drilling into the rock (Fig. 7.13b) and a drill bit that is not effectively drilling into the

rock (Fig. 7.14b,7.14c) is clear. Thus the friction vs. time curves could be used to assess the effectiveness of the drilling.

Chapter 8

Conclusions and Future Work

In this thesis, a physics-based, Eulerian-Lagrangian computational modeling framework to predict particle flow and tribological phenomena was presented. The Eulerian, CFD solver was introduced and validated for its spatial and temporal accuracy with analytical solutions for fluid flow. Two different spatial discretization schemes for the CFD were studied and their comparison was presented in Chapter 2. Similarly to the Eulerian phase, a lengthy discussion of the Lagrangian, DEM solver was presented in Chapter 3. The implementation of Verlet tables to increase computational efficiency was detailed.

Chapter 4 was dedicated to discussing the particle-particle, particle-fluid, particle-surface, and surface-fluid interactions which are captured by the framework. Stokes drag and Ergun drag were implemented in the framework to provide solutions for different flow conditions. Additionally, the framework was shown to capture the effect of particle heat transfer which is important in heated, packed particle beds. The problems of erosive wear modeling and rotary rock drilling were chosen as test cases for which the framework to model.

8.1 Conclusion and Future Erosive Wear Modeling

In this section, the erosive wear potential of lunar dust simulant was investigated so that the susceptibility of lunar hardware to erosive wear damage on the Moon could be better understood. The change in mass, was recorded after they were subjected to JSC-1AF particle impingement. The results from this study suggest that lunar dust, traveling even

at moderate velocities, may significantly alter the surfaces of the materials tested. Though small, the material removal may be important for thin films which coat surfaces or for foils. For lenses and mirrors on the Moon, the degradation in optical performance observed in this work would be significant to future lunar missions.

An erosive wear model was developed which was able to predict the effect of oblique impacts during erosive wear. It was seen that qualitative agreement between the model and the experiments was obtained for the shape and characteristics of the erosive wear scar. Quantitative agreement was also obtained between the model and the experiments for the material removal of the three tested specimen materials.

In future studies, conducting these tests in a vacuum may provide a better approximation of lunar conditions due to fluid structures in this test, such as vortices or stagnation points at the test specimen, which may have affected particle trajectories. Additionally, the use of a high-speed camera to estimate particle velocities is preferred over a dual-disk device because of it will allow for more precise characterization of particle velocities. During a similar study investigating Martian regolith dust impingement, it was found by Sengupta et al. that the thermal performance of materials may be affected by exhaust-blown particulates [63]. Therefore, the effects of erosive wear on lunar thermal systems, such as radiators, would benefit from investigation as well. The modeling of this phenomenon could benefit from a rarefied gas formulation to better predict conditions on the lunar surface.

8.2 Conclusion and Future Work Rotary Rock Drilling

A computational model, sensitive to the variation of industry-relevant parameters in rotary drilling, has been developed and presented. The model uses the discrete element method (DEM) to simulate the rock formation and drill bit. The bonded-particle model (BPM) is used to aggregate DEM particles in the rock formation. A simple uniform fluid flow is imposed on the domain to simulate the effect of the drilling fluid carrying rock cuttings away from the bit-rock interface.

Case studies were performed to understand the effect of varying the rock formation strength, the weight-on-bit (WOB), the drilling fluid viscosity and the angular velocity of the drill bit. Decreasing the formation strength and increasing WOB each had a positive effect on the ROP. Increasing the drilling fluid viscosity increased its effectiveness in removing rock debris from the bit-rock interface, which ultimately increased the ROP. The angular velocity had both a beneficial and detrimental effect on ROP. Increasing the angular velocity of the drill bit, for low angular velocities, was shown to increase the ROP. However, after a critical angular velocity was reached, the cutting became erratic, and the ROP decreased. The model predicted that bit-bouncing, indicated by intermittent contact between the drill bit and the rock, occurred at high angular velocities.

Additionally, the friction experienced by the drill bit was calculated. It was seen that the difference between a well-performing drill bit and a poorly-performing drill bit could be evaluated by observing the friction of the drill bit with the rock. As a result it was concluded that the drill bit's friction vs. time curve could be used to assess the drilling effectiveness.

Though the model does show the ability to produce qualitatively reasonable predictions, further efforts would need to be made before it can be deployed to provide quantitative predictions for rotary drilling. Realistic material properties for the rock and the drill bit are important aspects which would need to be included. Also, the effect that the extreme heat and pressures encountered during rotary drilling would have on these material properties would need to be incorporated as well. Though the current model uses a collection of four particles to represent the drill bit, a more representative drill bit would be required to capture some of the complex interactions between the drill bit and the rock formation. Finally, efforts would need to be made to better simulate the dynamic action of the complex drilling fluid.

Nonetheless, given the model's qualitative agreement with experiments and field data from other drilling studies, it is believed that the modeling framework developed in this work shows promise in being a technique for predicting drilling performance on rock materials in multiphase environments.

8.3 Closing Remarks

The current Eulerian-Lagrangian model's agreement with experimental data suggests that it will be well suited as a platform for modeling multiphase interactions. The ability to view and modify all components of the source code makes the current framework more attractive than typical commercial codes, such as ANSYS Fluent, in which such access is not provided to the user. Though open source codes, such as MFIX and OpenFOAM, do allow the user to view and modify the source code, the current Eulerian-Lagrangian modeling framework may be preferred for modeling particle tribology systems as the

wear, contact, and particle dynamics modules were integral in the creation of the current framework. Though they were once inchoate, the aforementioned commercial codes do possess the advantage of having years of scrutiny, testing, and development by scientists, researchers, and engineers. It is suggested that the current framework could also benefit from such prolonged attention. However, the results from the current framework which have been discussed in this thesis show great promise for the current framework's continued development and usage for modeling multiphysics phenomena.

APPENDIX

The following works describe modeling and experimentation which were highly-relevant in the development of the Eulerian-Lagrangian modeling framework described in this thesis.

Appendix 1: A 3D, Transient Model to Predict Interfacial Phenomena during CMP using Computational Fluid Dynamics

A version of the following work was published in the Journal of Engineering Tribology, .vol. 227, p. 777-786 (doi: 10.1177/1350650112466769). This work was produced using the Eulerian-Lagrangian modeling framework developed in this thesis.

Interfacial phenomena between the wafer and the polishing pad during chemical mechanical polishing (CMP) are an area of great interest as they affect post-CMP wafer topographies. Traditionally, the Reynolds equation has been used to predict the fluid pressure between the wafer and the polishing pad. However, by using computational fluid dynamics (CFD) it is possible to predict the fluid pressure and obtain insight into the fluid motion at the leading edge and trailing edge of the wafer. Additionally, CFD allows for the added ability to increase the resolution of the fluid physics to the asperity scale. In this work, a model is developed to predict phenomena related to mixed lubrication CMP using CFD. Contact mechanics between the wafer and the pad are resolved through a Winkler elastic foundation formulation. The wafer is mounted on a ball joint which allows free rotation to occur. Friction between the wafer and the polishing pad causes the wafer to assume a position which produces a sub-ambient pressure distribution similar to that obtained from experiments. The effects of different table speeds on the interfacial fluid pressure as predicted by the CFD are presented. Portions of this appendix were reported in the Journal of Engineering Tribology [93].

1.0 Introduction

Chemical mechanical polishing (CMP) is a manufacturing technique widely used in the semi-conductor industry. Its purpose is to achieve planarity between the interstitial layers of copper and silicon dioxide as integrated circuits (ICs) are fabricated. During CMP, the wafer, on which the IC is fabricated, is pressed into a rotating polishing pad. A slurry, containing abrasive nanoparticles, is entrained between the wafer and pad. The particles in the slurry wear away excess material resulting in planarization. Despite its widespread usage, CMP is known to, at times, impart defects on the IC's caused by non-uniform wear rates over the wafer surface. These defects, such as dishing and erosion, can result in unwanted electrical opens which ultimately cause malfunctioning computer chips. Therefore, on-going efforts over the past few decades have been dedicated to better understanding the CMP process in order to reduce such defects [15, 17, 94].

During CMP, the dominating phenomena which determine the effectiveness of polishing occur at the slurry-flooded interface between the wafer and the pad. The contact pressure in this region is of particular concern because loads applied to the wafer are transmitted to the particles in the slurry leading to abrasive wear [34, 95]. Consequently, many CMP models [16, 96] are based on a Prestonian model for material removal, equation (1), which is dependent upon the applied pressure to the wafer.

$$MRR = KPV \quad (1)$$

In equation (1) MRR is the material removal rate, K is the Preston wear constant, P is the pressure applied to the wafer. V is the relative velocity between the wafer and the pad.

Though equation (1) depends on the applied pressure, the true nature of the contact between the particles, pad, and wafer is also dependent upon the interfacial fluid pressure of the slurry. Because of mixed lubrication during CMP, positive slurry pressures can help to support the external load applied to the wafer, thus reducing the load on the particles, while negative slurry pressure may result in a net increase in load on the particles and the MRR.

There are several theories as to the nature of the interfacial fluid pressure of the slurry during CMP. In 2000, Shan et al. demonstrated experimentally that under certain conditions, the interfacial pressure of the fluid can be sub-ambient [97]. Under these conditions, the fluid pressure acts to pull the wafer towards the pad instead of separating the two surfaces. Shan et al. developed a theory about this phenomenon which attributed the sub-ambient pressure to the diverging geometry in the interface caused by friction-induced surface deformations. As an alternative explanation for the sub-ambient pressure, in 2005 Higgs et al. developed a model which attributed the sub-ambient pressure to a diverging geometry caused by wafer rotations about the wafer carrier [98]. In contrast, Park et al. predicted that the interfacial fluid pressure can be super-ambient, and work against the supplied wafer backpressure [99].

Given the multitude of experimental findings, and theories to support them, it is clear that higher-fidelity modeling techniques will be necessary to help elucidate more of the physics which contribute to wafer-pad interactions. Traditionally, the Reynolds equation, equation (2), has been used in CMP modeling to predict the slurry pressures [97-99].

$$\frac{\partial}{\partial x} \left(h^3 \frac{\partial p}{\partial x} \right) + \frac{\partial}{\partial y} \left(h^3 \frac{\partial p}{\partial y} \right) = 12\eta U \frac{dh}{dx} \quad (2)$$

Though researchers have had success using it, the Reynolds equation is inherently limited in its applicability and thus may not be suitable to predict certain emergent phenomena associated with CMP. To derive the Reynolds equation, from the more general Navier-Stokes equations, there are several assumptions which must be made [100]:

- 1) Body forces are negligible.
- 2) Pressure is constant through the lubricant film.
- 3) No slip at the bounding surfaces.
- 4) The lubricant flow is laminar (low Reynolds number).
- 5) Inertial and surface tension forces are negligible compared with viscous forces.
- 6) Shear stress and velocity gradients are only significant across the lubricant film.

To overcome the potential limitations posed by these assumptions, Terrell and Higgs developed a CMP model which uses the 3D transient Navier-Stokes equations to predict the behavior of the slurry [18, 101]. However, in their model, the fluid's only purpose was to provide drag forces to advect slurry particles. In the current work, this approach is extended. CFD is explored as a tool to predict interfacial pressures in the mixed lubrication environment between the wafer and the pad. Moreover, the mechanics are developed from this model to predict wafer tilt-angles, caused by the interfacial phenomena, which are a result of friction between the wafer and the pad.

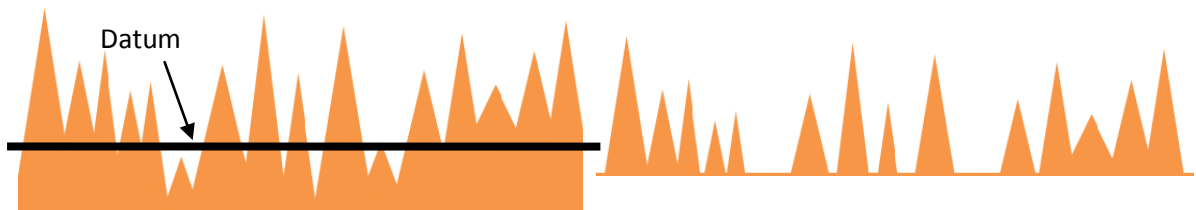
2.0 Modeling Methodology

To predict the interfacial phenomena under the wafer, individual models were created for each of the fundamental CMP components – namely (1) the polishing pad, (2) the wafer,

and (3) the slurry. In this section the methods to create these models are detailed as well as the techniques used to couple the physics between each of these components.

2.1 Pad and Wafer Contact Mechanics

To model the polishing pad and wafer, surfaces were defined and discretized using pixilated volume units called voxels [101]. The pad was modeled as a $50\text{ }\mu\text{m} \times 50\text{ }\mu\text{m}$ square surface that was 31 voxel-asperities in length and 31-voxel-asperites in width. The height of each pad voxel-asperity was initialized based on a random Gaussian distribution. To conserve computational resources, a threshold height was established as a datum for the pad surface. The heights of all asperities were referenced from this datum and any asperity which was below the datum was assigned a very small height ($0.001\text{ }\mu\text{m}$). Though it would have made sense to prescribe asperity heights below the datum as $0.000\text{ }\mu\text{m}$, the value of $0.001\text{ }\mu\text{m}$ was used instead to prevent numerical uncertainties. The resulting final surface roughness was $4.34\text{ }\mu\text{m}$ and the final mean voxel-asperity height was $5.31\text{ }\mu\text{m}$. It should be noted that imposing the datum in the model to conserve computational resources did not affect the contact mechanics of the wafer-pad system as only a small fraction of the tallest voxel-asperities of the pad contact the wafer. Images to describe the voxel-asperity height datum, the final resulting discretized surface, and a histogram of the final voxel-asperity heights are provided in Fig. 1.



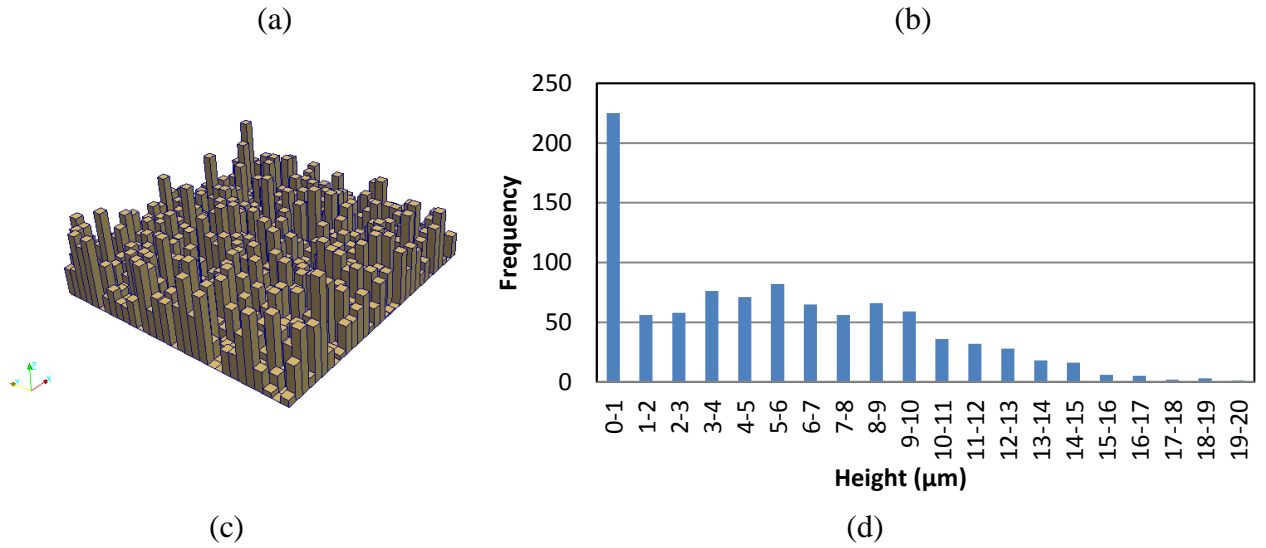


Fig. 1 Description of pad topography. (a) schematic of voxel-asperity heights before imposing datum (b) schematic of voxel-asperity heights after imposing datum (c) Image of the voxelized pad surface used in model showing the discrete heights (d) Histogram of the pad's voxel-asperity heights used in model

The voxels in the polishing pad were translated at a constant velocity to represent the motion of the pad under the wafer during the polishing process. Relative to the pad, the surface of the wafer is quite smooth. As a result, the wafer is modeled with zero roughness.

The contact mechanics between the wafer and the pad are resolved using the Winkler elastic foundation model which has been used in CMP modeling in the past [98, 101]. In the Winkler elastic foundation, the surface of the pad is modeled as a collection of independent springs which support the contact load between the wafer and the polishing pad. These voxel-asperities serve as the springs used in the Winkler elastic foundation. The spring constants used in this work were not reconciled with typical mechanical properties for the wafer and pad surfaces but were instead adjusted until the mean gap height was comparable to published CMP models. The mean gap in the current work was

approximately 9.69 microns and the ratio of real contact area to nominal contact area was approximately 0.02. A schematic of the wafer-pad system modeled with the Winkler elastic foundation can be found in Fig. 2.

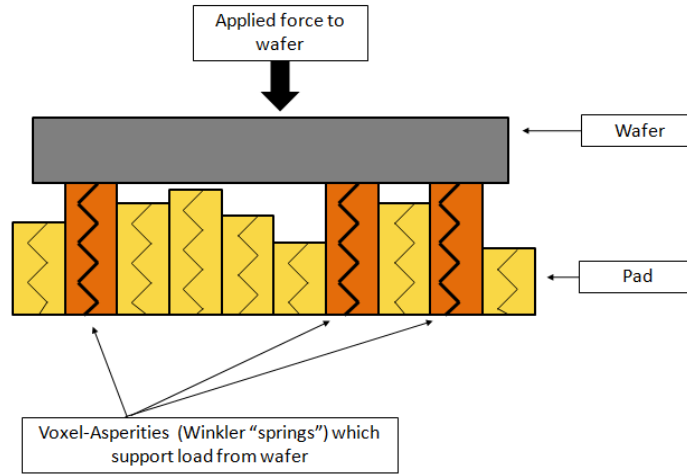


Fig. 2 Schematic of the wafer-pad system using the Winkler elastic foundation.

Backpressure applied to the wafer is counteracted by the contact with the polishing pad. The wafer has two degrees of freedom in that it can move up and down vertically and can rotate. The rotation of the wafer is intended to model the ball joint that supports the wafer carrier during CMP. Summation of forces on the wafer in the vertical direction consists of the backpressure applied to the wafer and the contact force from the pad. The backpressure in the model is prescribed to be 20 psi in accordance with typical CMP backpressures. Newton's second law, equation (3), is used to then calculate the acceleration of the wafer in the vertical direction which is perpendicular to the pad's translation.

$$F_{pad} + \int_{wafer} backpressure = m_{wafer} a_{wafer} \quad (3)$$

In equation (3), F_{pad} is the force on the wafer due to contact pressure with the pad. It is calculated by integrating the contact stress from the pad over the wafer's surface. The backpressure is the pressure applied to the wafer. M_{wafer} and a_{wafer} are the wafer's mass and acceleration, respectively.

Friction forces are generated at the interface by the contact between the wafer and the translating pad. These frictional forces cause moments about the wafer's center which induce a rotation. The wafer is then rotated depending on the sum of these moments.

2.2 Slurry modeling

The slurry plays a critical role in CMP. The slurry contains the nanoparticles which are believed to do the polishing in CMP. Also, the slurry's pressure affects the contact mechanics between the wafer and the pad. To model the slurry, a single phase framework is developed which uses , the Chorin projection to numerically approximate the Navier-Stokes equations [32, 35]. Beginning with the momentum equations, (4a), (4b), and (4c), an explicit Euler time-stepping algorithm is used to solve for the new velocity components, on a staggered grid, at each successive time-step. The variables u, v, w , and p represent the x, y, z components of the fluid velocity and the pressure, respectively.

$$\rho \left(\frac{\partial u}{\partial t} + u \frac{\partial u}{\partial x} + v \frac{\partial u}{\partial y} + w \frac{\partial u}{\partial z} \right) = -\frac{\partial p}{\partial x} + \mu \left(\frac{\partial^2 u}{\partial x^2} + \frac{\partial^2 u}{\partial y^2} + \frac{\partial^2 u}{\partial z^2} \right) \quad (4a)$$

$$\rho \left(\frac{\partial v}{\partial t} + u \frac{\partial v}{\partial x} + v \frac{\partial v}{\partial y} + w \frac{\partial v}{\partial z} \right) = -\frac{\partial p}{\partial y} + \mu \left(\frac{\partial^2 v}{\partial x^2} + \frac{\partial^2 v}{\partial y^2} + \frac{\partial^2 v}{\partial z^2} \right) \quad (4b)$$

$$\rho \left(\frac{\partial w}{\partial t} + u \frac{\partial w}{\partial x} + v \frac{\partial w}{\partial y} + w \frac{\partial w}{\partial z} \right) = - \frac{\partial p}{\partial z} + \mu \left(\frac{\partial^2 w}{\partial x^2} + \frac{\partial^2 w}{\partial y^2} + \frac{\partial^2 w}{\partial z^2} \right) \quad (4c)$$

$$\frac{\partial u}{\partial x} + \frac{\partial v}{\partial y} + \frac{\partial w}{\partial z} = 0 \quad (5)$$

Pressure-velocity coupling is achieved by satisfying the continuity equation (5). The pressure at each time-step is solved through the successive over-relaxation (SOR) method.

2.3 Physics-based coupling and comparison to the Reynolds equation

The interaction between the slurry and the solid surfaces of the wafer and the pad are handled by adjusting the boundary conditions on all solid surfaces. A no-slip, no-flux boundary condition was prescribed at the interface between the slurry and the polishing pad and the wafer. As mentioned in section 1.0, the Reynolds equation has been used for years with much success to predict the pressure generated in thin films at low Reynolds numbers. As a comparison, a two-dimensional converging geometry was created in which both CFD and the Reynolds equation were used to predict the pressure distribution. The Reynolds number in the domain was approximately 0.49. An image of the domain is provided in Fig. 3a and the comparison with the Reynolds equation, equation (2), is provided in Fig. 3b.

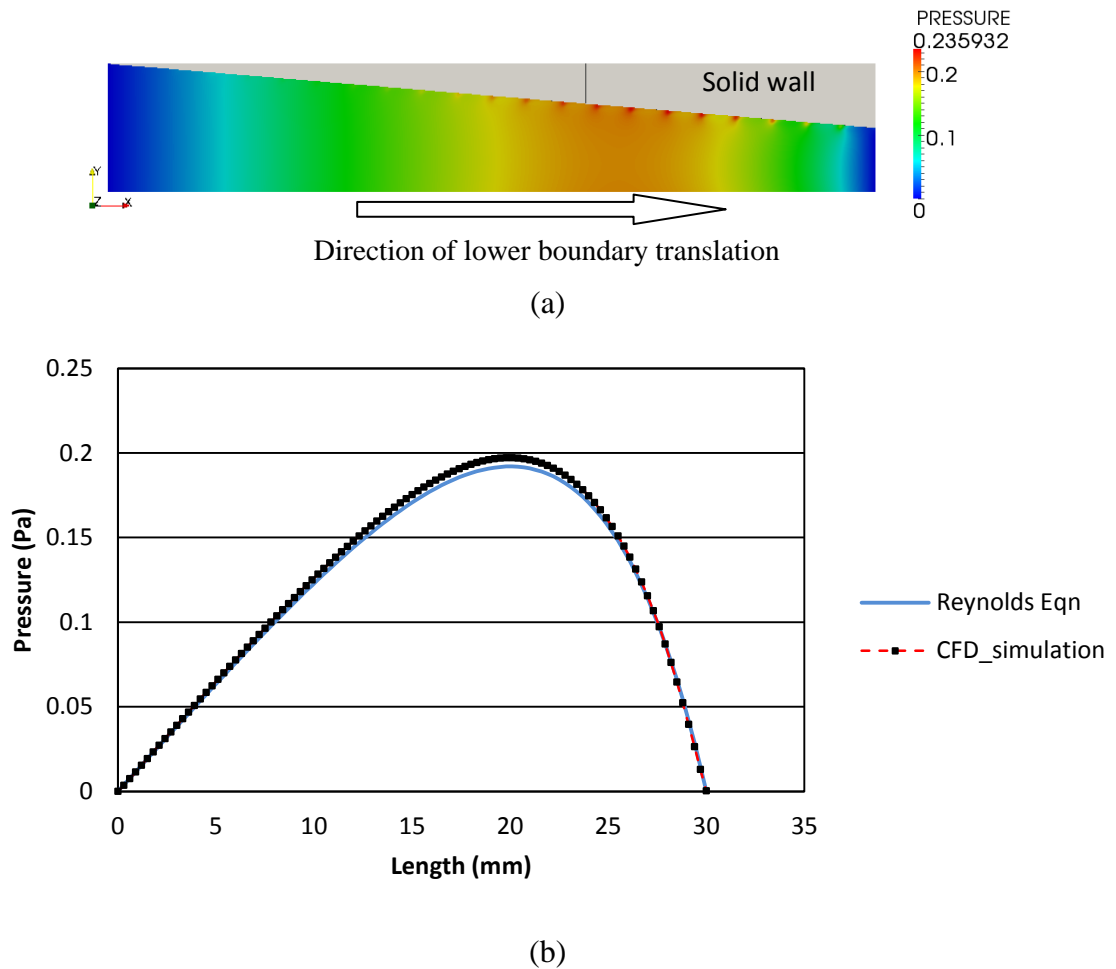


Fig. 3 A comparison between two-dimensional CFD and the Reynolds equation. (a) An image of the CFD domain showing a converging geometry and a pressure contour (b) A graph comparing the quantitative predictions of CFD and the Reynolds equation

In Fig. 3a, the pressure contour, as predicted by the CFD, is displayed. It can be seen that the pressure is mainly constant across the gap (in the y direction). In the derivation of the

Reynolds equation, it is assumed that the pressure across the gap is constant. Thus, the CFD prediction suggests this assumption is valid, and is in good agreement with the Reynolds solution for this geometry. In Fig. 3b, the pressure is plotted across the length of the domain. It can be seen in Fig. 3b that there is very good agreement between the pressure predicted by the Reynolds equation and the pressure predicted by the CFD. This fundamental study indicates that for certain flow domains, the agreement between the Reynolds equation and CFD can be very good. However, as the complexity of the flow domain increases due to objects, such as asperities or abrasive particles, it is believed that CFD can be an invaluable tool to obtain information about both the pressure and velocity of the slurry flow.

3.0 Results and Discussion

In this section, the results from the model are presented for two case studies. The first was a study to estimate the effect of friction on the wafer dynamics. The information from the first study was used in the second study to determine the effect that table speed, or RPM, of the pad will have on the interfacial pressure of the slurry. It should be noted again that this model only simulates a 50 μm x 50 μm area of the wafer-pad interface. As such, the results from it are intended to provide qualitative information on the nature of the wafer-pad interface. In Fig. 4, the modeling domain is visualized.

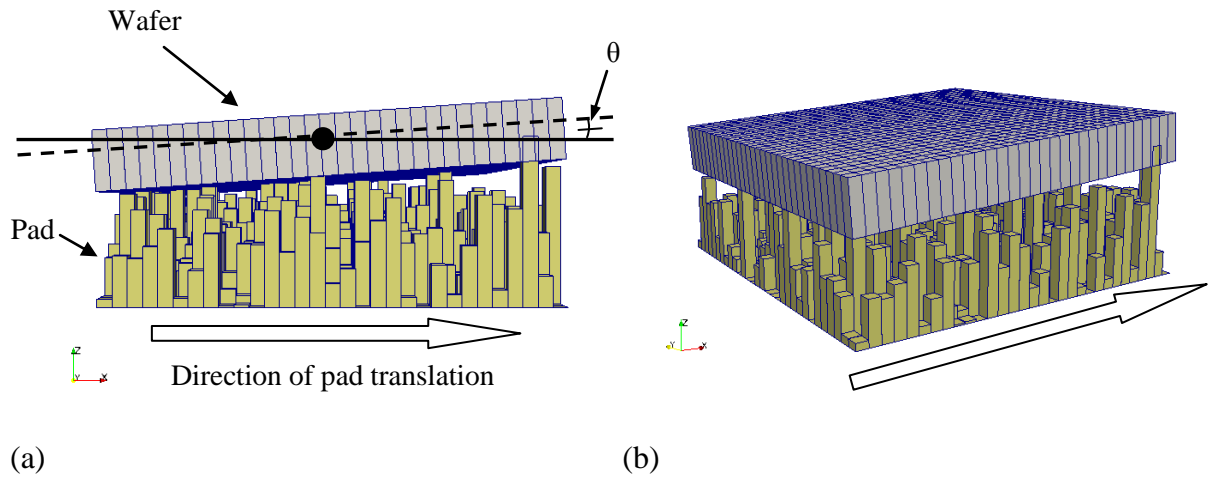


Fig. 4 Image of the pad contacting the inclined wafer. (a) side view showing tilt-angle
(b) Trimetric view

The tilted wafer and rough pad can be seen in Fig 4a. Fig.4b is a trimetric view for clarity. The tilt angle of the wafer is described as the angle of the wafer's rotation relative to the plane of the pad.

3.1 Transient Analysis of Wafer Tilt Angle

The first case study performed was to assess the effect of friction on the wafer's tilt angle. Because understanding the effect of friction was the primary objective, this study was performed without the CFD solution. As the pad passes under the wafer, friction between the wafer and the pad causes the wafer to rotate about the ball joint in the wafer carrier. The coefficient of friction between the wafer and the pad, μ , was varied between 0.1 and 0.5. Correspondingly, the magnitude of the frictional forces at the interface became larger with increased friction coefficients. The increase in friction forces resulted in an increased moment about the wafer's ball joint.

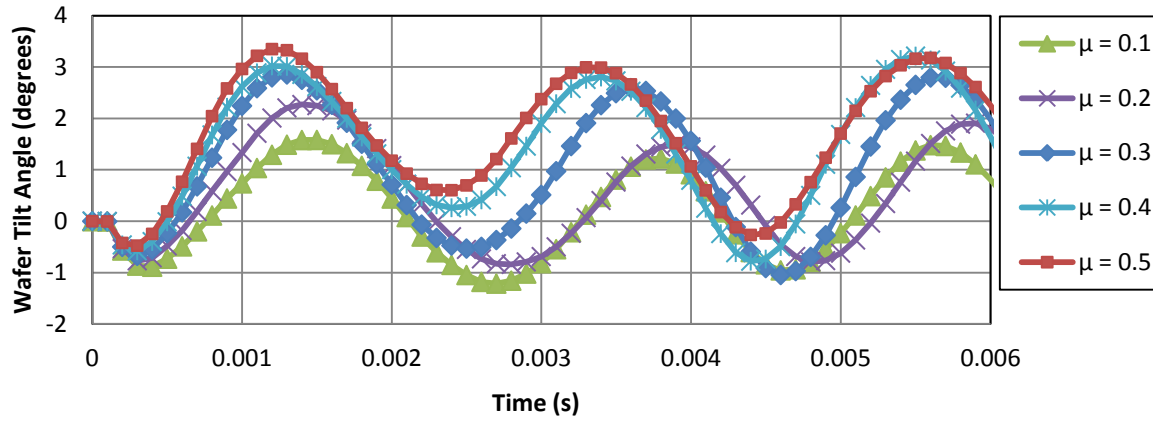


Fig. 5 Transient analysis of the wafer's rotation angle for different friction coefficients

It can be seen in Fig. 5 that the friction forces and the normal forces combine to cause the wafer to rock about the ball joint in the wafer carrier. As the wafer is lowered to the rough pad, the initial contact is with the highest asperities. If these highest asperities are close to the leading edge of the wafer, the contact forces from these asperities creates a moment about the wafer center. This moment causes the wafer to rotate in a direction which produces a converging film geometry. This can be seen in Fig. 6a.

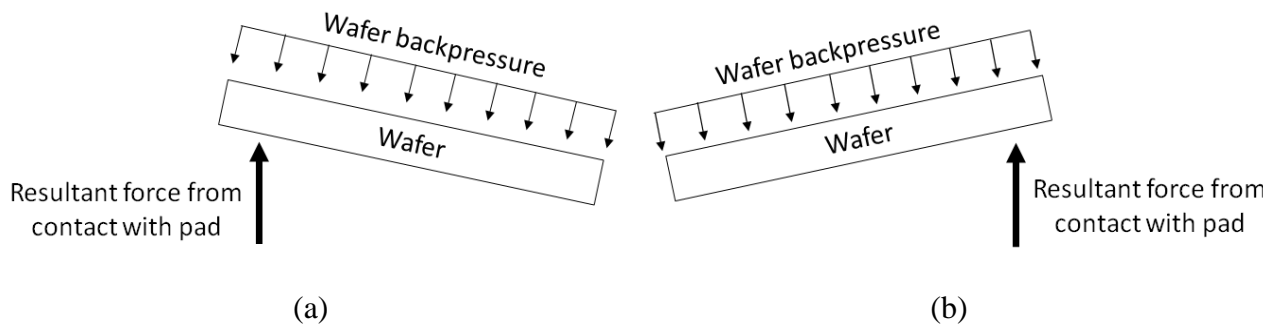


Fig. 6 The effect contact mechanics on wafer rotation. (a) net contact force at leading edge of wafer causing rotation. (b) net contact force at trailing edge of wafer causing rotation.

As these highest asperities move past the center of the wafer, they produce contact stresses which create a moment about the wafer center which causes it to produce a diverging film geometry. This can be seen in Fig. 6b.

The changes in these moments cause the wafer to rock. Friction forces also play a critical role in this process. Because the friction only produces a moment in one direction about the ball joint supporting the wafer, it determines the average tilt angle over time. In other words, though the wafer is dynamically rocking about the ball joint, the net tilt angle is controlled by the friction between the wafer and the pad. In Fig. 7, the average wafer tilt angle of the rocking wafer, over the duration of the simulation, is plotted against several different coefficients of friction.

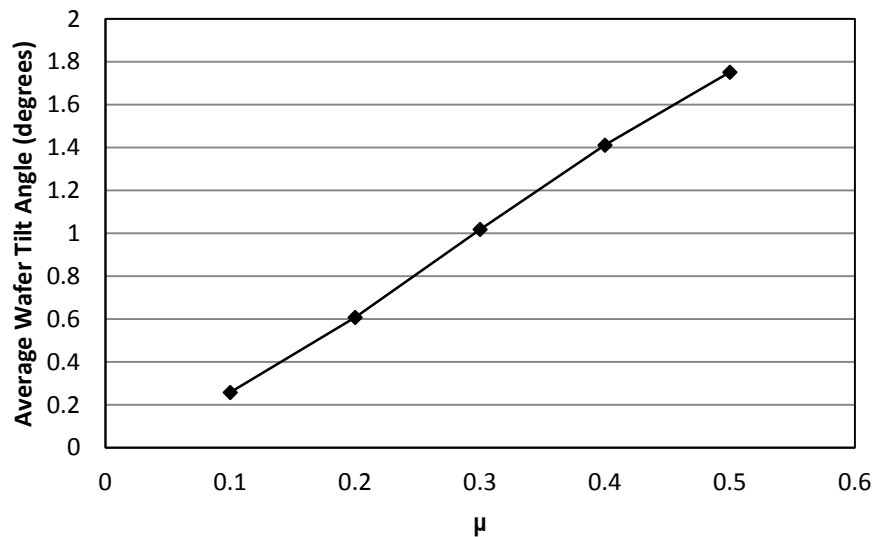


Fig. 7 The average wafer tilt angle for various friction coefficients

It can be seen in Fig. 7 that as the friction coefficient increases, the net tilt angle of the wafer increases. This is because the moment about the wafer's ball joint increases as the

friction coefficient increases. With a larger moment, the wafer's average tilt angle increases as well.

While the model domain size is only a fraction of the full wafer-pad domain, results such as those displayed in Fig. 7 demonstrate that the modeling framework is able to simulate the transient behavior of the interface while taking into account asperities. The actual dynamic response of the wafer to the pad's asperities may produce tilt angles of significantly less magnitude (i.e., less wafer rocking) when the effects of the fluid are taken into account and a larger area of the wafer-pad system is modeled. The reason for this is two-fold. First, the fluid may act as a mechanical damper to remove energy from the wafer-pad system which reduces the dynamic rocking. Second, if a larger area of the wafer is taken into account, the contact stress across the wafer may be more uniform resulting in less of a contact stress-induced moment. Nonetheless, the model highlights that fact that a random distribution of asperities heights can produce contact stresses on the wafer which induce a net moment. As the pad translates under the wafer, the moment from the contact changes and the wafer dynamically responds to it. The ability for a model to predict minute and transient changes in the wafer-pad contacts with this fidelity is important because transient data, such as frictional forces vs. time, have been used in the past to establish slurry performance in CMP polishing [102].

3.2 Interfacial Fluid Pressure

The interfacial fluid pressure has been an area of study in CMP for several years [98, 99]. One unique experimental research finding was that under certain conditions, a sub-ambient fluid pressure could form *in situ* in a CMP-like interface comprised of a metal

fixture (acting as the wafer) and a CMP pad [103]. To assess the current model's sensitivity in predicting this parameter, the wafer tilt angle was fixed and the RPM of the pad was varied. The fluid properties and average gap thickness were set such that similar Reynolds numbers were obtained as those used by Higgs et al. [98]. In the current work, the Reynolds number is approximately 27.8. As was demonstrated in section 3.1, the coefficient of friction between the wafer and the pad has a substantial effect on the wafer dynamics. In this work, a coefficient of friction of 0.6 was selected as it matches Higgs et al. [98] and is close to the 0.8 value used by Shan et al. [97] in CMP modeling. Using the data presented in Fig. 7, it was extrapolated that a coefficient of friction of 0.6 would produce a net wafer tilt angle of 2.2° . Therefore, this tilt angle was fixed in the current section and the pad's translational velocity was varied over several RPM values. The same pad area of $50\text{ }\mu\text{m} \times 50\text{ }\mu\text{m}$ was studied. For this size of the domain, a CFD mesh with 216000 fluid nodes was created and the study took approximately 23 hours to run on an Intel® Core™ i7 CPU at 2.8 GHz and 6GB ram. Preliminary simulations were also run on the Pittsburgh Super Computer (PSC), Blacklight shared-memory system. The results of this study are plotted in Fig. 8.

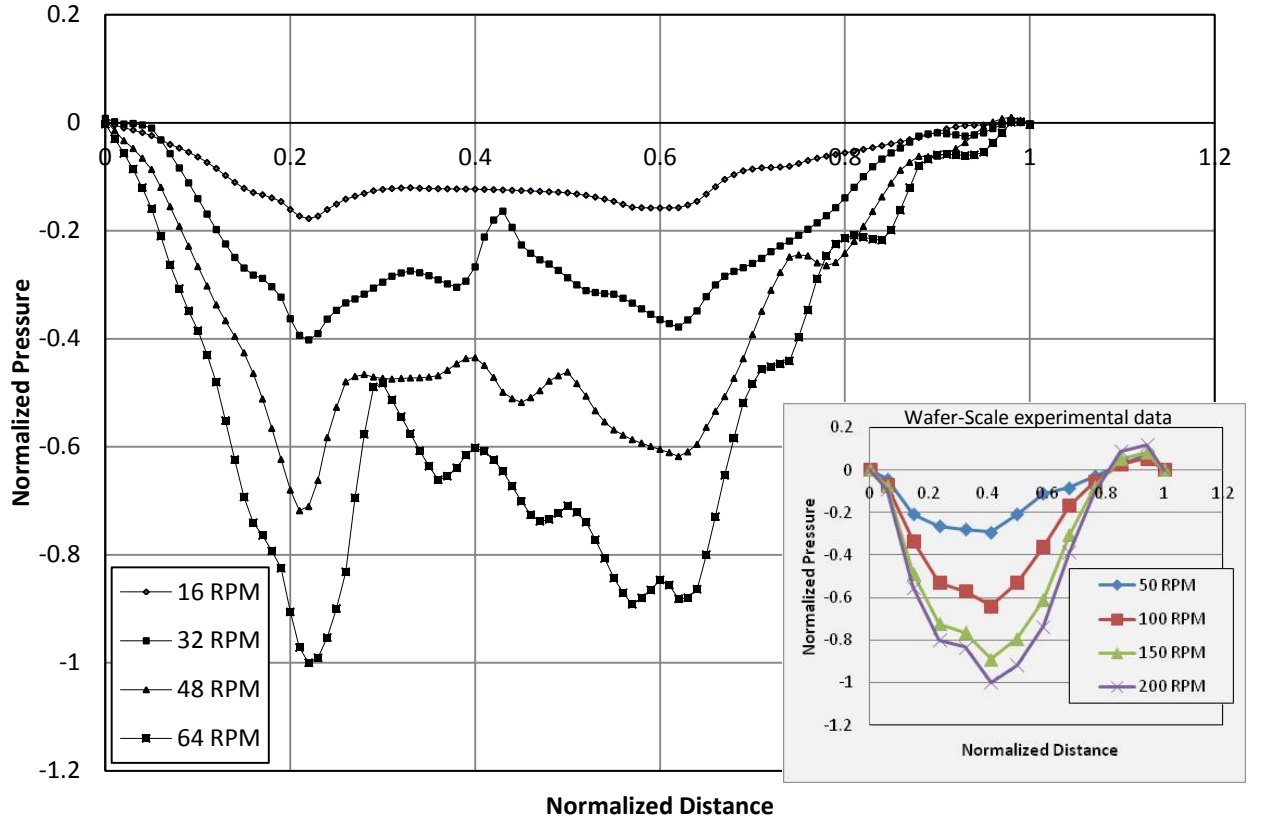


Fig. 8 The normalized interfacial pressure of the slurry under varying table speeds. An inset of experimental data from Higgs et al.[98] is provided for comparison.

In Fig. 8, the normalized slurry pressure along the direction of the moving polishing pad is plotted. Because only a $50\ \mu\text{m} \times 50\ \mu\text{m}$ region of the wafer-pad system was simulated, the pressures predicted from the current model are only valid for a wafer-pad system of this size. To present the results in a manner that could be useful for comparison with a wafer-scale experiment, the results presented in Fig. 8 have been normalized by the largest magnitude of pressure in the simulation. This pressure was 1225.4435 Pa and corresponds to the value of “-1” on the y-axis of the plot in Fig. 8. The x-axis has also been normalized by the length of the domain such that “1” on the x-axis corresponds to $50\ \mu\text{m}$. It can be seen in Fig. 8 that as the RPM increases, the magnitude of the sub-ambient fluid pressure becomes greater. The fluid is sub-ambient because of the

diverging geometry created by the wafer tilt angle. As the fluid diverges under the wafer, its pressure decreases as it occupies the progressively larger volume under the wafer. As the RPM of the pad increases, more fluid is entrained under the wafer and the effect is amplified. Though not the same quantitatively, this trend matches qualitatively to the full wafer-scale experiments obtained by Higgs et al.[98] The pad table speeds are different in the experimental data. However, the speeds were incremented in the same ratios as the parametric study for current model. The inset graph in Fig. 8 displays these experimental results. They have also been normalized by the largest pressure and the length of the wafer. In Fig. 9, contour plots of the pressure in the domain are presented for comparison. In a similar manner to Fig. 8, the contour plots below have been scaled such that the relative differences between the different table speeds studied can be observed.

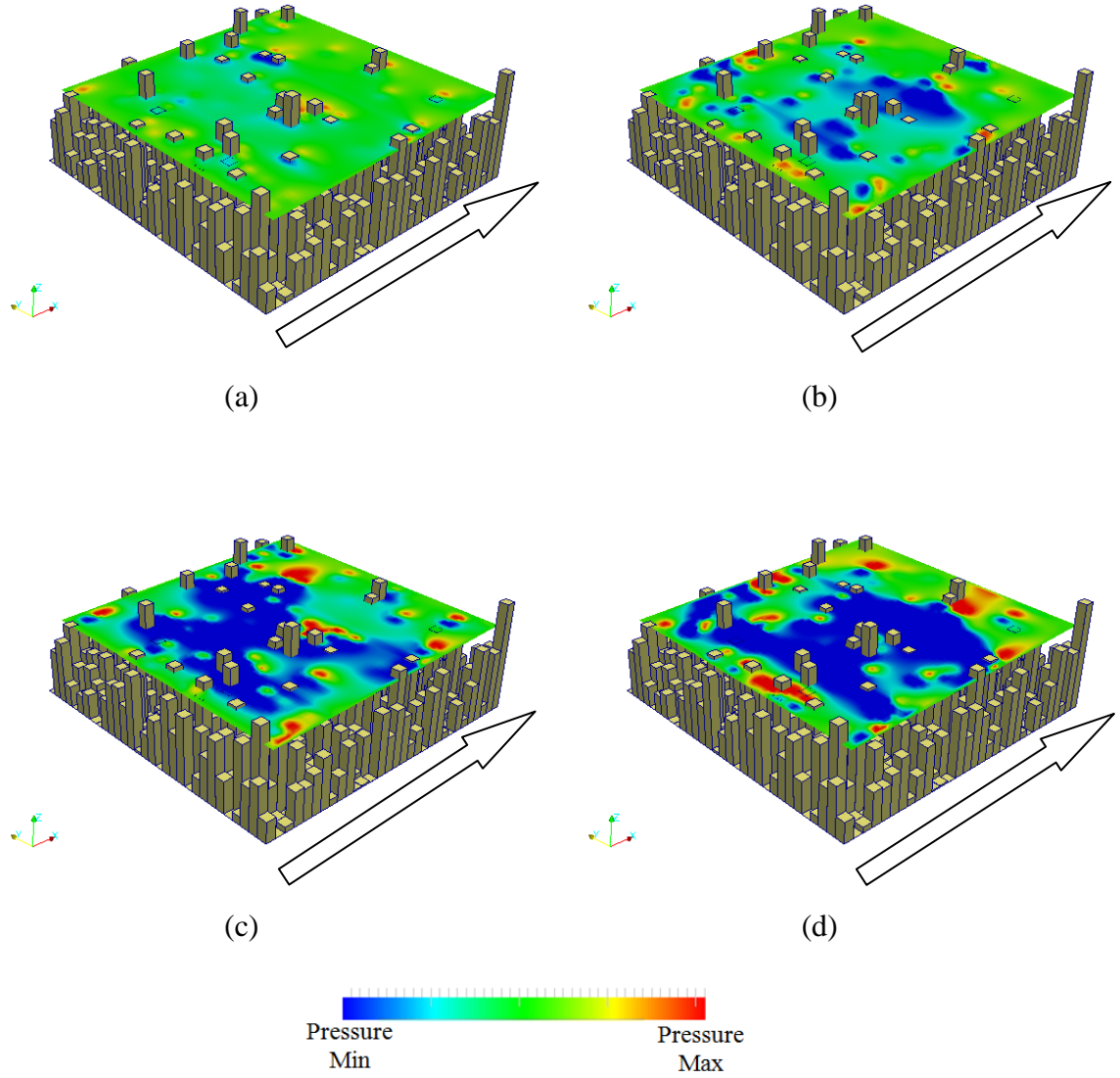


Fig. 9 Contour plot of slurry pressure under the wafer (for clarity, the wafer is not shown in this image). (a) 16 RPM (b) 32 RPM (c) 48 RPM (d) 64 RPM

It can be seen in Fig. 9 that the region of sub-ambient slurry pressure grows as the RPM increases.

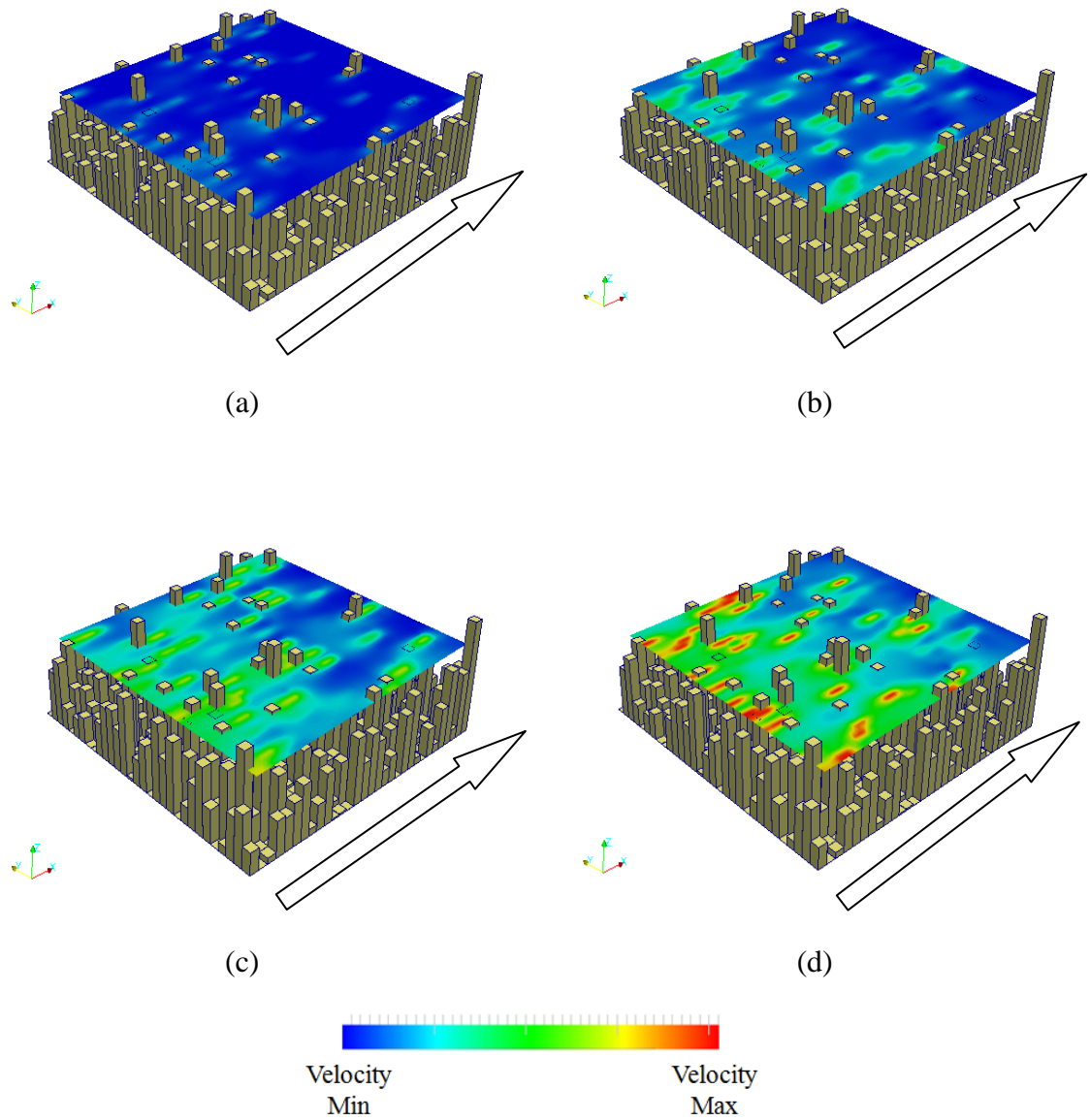


Fig. 10 Contour plot of slurry velocity under the wafer (for clarity, the wafer is not shown in this image). (a) 16 RPM (b) 32 RPM (c) 48 RPM (d) 64 RPM

The use of CFD allows for a more refined prediction of the fluid velocity and pressure in the domain than the Reynolds equation. For example, a contour of the prediction of the fluid velocity magnitude is displayed in Fig. 10.

4.0 Conclusions

In this work a model was presented to analyze the motion of the wafer in a mixed lubrication type CMP environment. Unlike approaches that use the Reynolds equation, this method uses CFD to analyze the slurry flow under the wafer to predict changes in fluid pressure. It was shown that a sub-ambient pressure under the wafer is generated for certain wafer configurations in a similar manner to those seen in experiments [98].

Additionally, select transient effects were studied. The current model displayed the ability to predict transient behavior of the wafer as it is loaded against the polishing pad. Though the wafer constantly moved during the simulation as a result of changes in contact pressures and frictional forces due to the underlying topography, it was seen that higher frictional forces had a net effect on the wafer of producing higher tilt angles.

The current model provides a method to predict slurry pressures during CMP under a small portion of the wafer. Simulating the slurry pressure under the entire wafer, using CFD, remains a challenge. The high aspect ratios generated due to the large wafer area compared to the thin separation gap between the wafer and the pad, would result in much computational demand. Nevertheless, with enough computational resources, the methods described in this work can be extended to simulate the slurry pressure under the entire wafer. Such a simulation, especially if it were extended to slurry entrance and exit regions, may provide important insight into slurry entrainment and flow characteristics during CMP.

5.0 Funding

The authors would like to acknowledge the NASA Graduate Student Researchers Program (GRSP) for their support of the first author. This work used the Extreme Science and Engineering Discovery Environment (XSEDE), which is supported by National Science Foundation grant number TG-MSS120003. This work was also partially supported by an NSF CAREER award #0645124.

Appendix 2: A Comparison of Active Particle Models for Chemical Mechanical Polishing

A version of the following work was published in the Electrochemical Society's Journal of Solid State Science and Technology, vol. 2, p. P87-P96 (doi: 10.1149/2.019303jss). This computational modeling in this work was performed using the Particle-Augmented Mixed Lubrication model developed by Terrell and Higgs (Terrell and Higgs, 2009).

A multitude of models exist to predict the material removal rate (MRR) during CMP. Common among many of these models is the prediction of the MRR based on the product of the material removal rate per particle (MRR_{PP}) and the number of active particles, N_{act} , actively contributing to the material removal. Discrepancies between CMP models and experiments are sometimes compensated for by empirical wear coefficients that are used as fitting parameters placed on the overall CMP model. However, such empirical correlations can obscure deficiencies in the prediction of the material removed per particle and the number of active particles. A decoupled understanding of both MRR_{PP} and N_{act} is essential for accurate modeling of CMP. This work investigates the predictions of several active particle models, decoupled from the prediction of the MRR, to assess their agreement. In addition to the number of active particles, the models are used to predict the number of particles in the interface and the number of particles eligible to become active. It is found that although the models differ greatly in their assumptions to predict these quantities, there is some similarity in their prediction of the number of active particles. Portions of this appendix were reported in the Electro-Chemical Society Journal of Solid State Science and Technology [8].

Nomenclature

a = Radius of slurry particle

A_{nom} = Nominal contact area {Length²}

a_{max} = maximum radius of slurry particle

A_{real} = Real contact area {Length²}

h = Average gap height between the wafer and the pad {Length}

i_{max} = total number of discretized asperities for Particle-Augmented Mixed Lubrication model

ϕ = solid-fraction (volume-based)

λ = line density of particles {Length⁻¹}

$N_{\text{all_PML}}$ = Number of particles in the interface for Particle Mono-Layer model

$N_{\text{all_PI}}$ = Number of particles in the interface for Particle-Indentation model

$N_{\text{all_PAML}}$ = Number of particles in the interface for Particle-Augmented Mixed Lubrication model

$N_{\text{elig_PML}}$ = Number of eligible active particles for Particle Mono-Layer model

$N_{\text{elig_PI}}$ = Number of eligible active particles for Particle-Indentation model

$N_{\text{elig_PAML}}$ = Number of eligible active particles for Particle-Augmented Mixed Lubrication model

$N_{\text{act_PML}}$ = Number of active particles for Particle Mono-Layer model

$N_{\text{act_PI}}$ = Number of active particles for Particle-Indentation model

$N_{\text{act_PAML}}$ = Number of active particles for Particle-Augmented Mixed Lubrication model

Ω = probability that an eligible particle will become active for Particle-Indentation model

t = closet approach of wafer and pad for Particle-Indentation model {Length}

Vol_{all_PML} = Total volume in the interface which can be filled with slurry for Particle Mono-Layer model {Length³}

Vol_{all_PI} = Total volume in the interface which can be filled with slurry for Particle-Indentation model {Length³}

$Vol_{partAVG}$ = Volume of the average particle {Length³}

Vol_{asp} = Volume of the asperities in contact with the wafer for Particle-Indentation model {Length³}

1.0 INTRODUCTION

Integrated circuits (ICs) are used in almost every modern electronic device. Typically, IC's are built on silicon wafers in a process that involves many deposition and material removal steps. Chemical mechanical polishing (CMP) is a commonly used planarization technique for the IC manufacturing industry [104]. It is a critical process in which material is removed from the wafer before the next layer of the IC is constructed. CMP is employed because of its ability to produce flat surfaces with low levels of roughness. Both of these qualities are desired during IC fabrication because variation in the surface of one layer can propagate to other layers, as the IC is fabricated. Moreover, the critical downstream step of lithographic patterning can be unsuccessful if the wafer surface is not planarized. During CMP, the wafer is rotated and pressed into a rotating polishing pad. A chemically-active slurry, containing abrasive nanoparticles, is entrained between the rotating polishing pad and the wafer. The nanoparticles in the slurry wear the surface of the wafer until the unwanted material is removed. Differential wear rates on the wafer during CMP have been shown to produce defects in the IC [105]. These defects negatively affect the IC performance and can lead to a reduced production yields. As a result, there have been many models developed which have helped to elucidate the complex behavior during CMP in the past few years[64, 84, 95, 106]. In 2009, Oh and Seok [107] proposed that non-Prestonian behavior during CMP could be modeled using a modified version of Zhao and Chang's prediction for active particles[64] and a diffusion model to capture the effect of the slurry chemicals on the wafer [107]. Oh and Seok introduced two fitting parameters, related to the pad-wafer contact, to align the number of abrasive particles removing material predicted by their model to phenomenological occurrences during CMP. With their model, Oh and Seok achieved agreement with

experimental results for material removal. In 2010, Xin et al. developed a model for material removal in CMP based upon the formation of a modified layer of material on the surface of the wafer due to the chemically-active slurry [108]. Xin et al. suggested that the particles in the slurry bond with this layer and fluid-induced shear stresses remove the particles from the surface, along with any material that is adhered to them. Kong et al. recently developed a model using statistical methods and Bayesian analysis to predict CMP performance [109]. In their model, *in situ* sensor data from CMP, such as pad-wafer deflections and vibration, was used to predict the material removal rate. To predict the effect of slurry parameters on material removal during CMP, Wang et al. introduced a novel CMP model in 2010 [28]. Wang et al. predicted the total number of abrasive particles removing material by calculating the number of particles on single pad asperity, assuming a uniform distribution of particles in the slurry, and multiplying the result by the total number of pad asperities in contact with the wafer. The wear mechanism assumed by Wang et al. was based upon the deteriorating bonds of the wafer's surface molecules as a result of the slurry chemistry. Wang et al. were able to predict trends found in CMP experiments when varying parameters such as abrasive size and concentration. In 2011, Tsai et al. introduced a CMP model in which grain flow approximation was applied to lubrication theory to predict the film thickness and shear stress during CMP [110]. The model displayed a decrease in film thickness as the wafer backpressure was increased. These results agreed with experimental findings. Wei et al. developed a model in which they balanced forces and moments on the wafer [111]. Wei et al. related the number of particles taking part in the material removal to the concentration of the slurry and took into account the pad grooves to predict the interfacial

fluid pressure and the wafer's material removal rate. To predict the effect of wafer topography on CMP, Wu and Yan introduced a model using finite element analysis (FEA) [112]. This model used combinations of cosine functions to extrapolate FEA results for the contact stress to various scenarios encountered during CMP. Combining their predicted contact stress with Preston's equation for wear, they were able to estimate the material removal rates during CMP.

Predicting the material removal rate (MRR) during CMP is challenging because of the complex interplay between chemical and mechanical processes. Additionally, it is believed that not every particle between the wafer and the pad contributes to material removal. As depicted in Fig. 1, typical CMP parameters only allow the wafer (which is nominally smooth compared to the pad) to make contact with the pad in only a few areas of real contact (A_{real}) during CMP. However, the apparent, or nominal, contact area (A_{nom}) can contain many slurry particles which are in the interface between the wafer but do not make contact with the wafer. These particles reside in the volume between the wafer and the pad and may just be present without affecting the MRR. Recent work by Lei et al. demonstrates this phenomenon well through CMP experiments in which a fluorescence microscope is used to look through a glass wafer and obtain *in situ* particle trajectories [113].

Fig. 1

To account for this fact that not all of the particles within the interface contribute to wear, many authors classify slurry particles as “active” and “inactive”. The active particles are the particles in the wafer-pad interface actively involved in material removal, whereas the

inactive particles are the ones that do not contribute to material removal. Thus, it is common to predict MRR as the material removed per particle (MRR_{pp}) multiplied by the number of active particles under the wafer (N_{act}) [64, 95, 114-118]

$$MRR = MRR_{pp} * N_{act} \quad [1]$$

Predicting the MRR_{pp} is a complex area of research in its own right. Third-body particulate wear formulations, even in dry scenarios, are challenging due to material anisotropy [119, 120], dislocations [121] and other microstructure-related phenomena [122]. Moreover, third-body particles in the sliding interface can act as solid lubricants, or bearings, between the surfaces due to rolling and momentum exchange [123]. Complicating the material removal prediction further is the effect of the chemically-active slurry and complex particle-surface interactions which dictate the wear process [124-127] .

Early CMP models began as mostly-empirical, wafer-scale correlations for the global MRR based upon the Preston's equation [128] (Eq. 2) where K_p is the empirical Preston's coefficient, P is the applied pressure, and V is the relative velocity between the wafer and the pad.

$$MRR = K_p * P * V \quad [2]$$

Despite the fact that much progress in modeling CMP has been made, challenges in predicting the MRR_{pp} have caused many researchers to maintain some empirical coefficients when developing CMP models. In such models, coefficients are, at times, tuned based upon experimental data. Though authors have had success with this method of using empirical data to calibrate CMP models [95, 129], the introduction of the tuned

empirical coefficients can obscure inaccuracies, making it difficult for subsequent research efforts to identify points of improvement. As can be seen from the nature of Eq. 1, proper estimation of the number of active particles in CMP is just as crucial as predicting the MRR_{pp} for the development of fundamental (i.e., non-empirical) CMP models. Using empirical methods to tune the MRR_{pp} can mask uncertainty in the active particle calculations. Moreover, efforts to better predict MRR_{pp} [64, 116, 119, 130] will only advance CMP models if the number of active particles is well understood. Additionally, though abrasive-free slurries have also been developed for CMP, the study of active particles is still relevant for these processes. Chemical corrosion is believed to be the dominant material removal mechanism in abrasive-free slurries. However, it has been observed experimentally that wear debris generated during abrasive-free polishing can introduce particulates into the wafer-pad interface which cause abrasive and adhesive wear [125]. As a result, the study of active particles is of interest even for abrasive-free slurries, as well.

As such, this work investigates the merit of several active particle models to evaluate their agreement when decoupled from the MRR and MRR_{pp} predictions. The active particle models are evaluated through a direct comparison of their predictions under varying CMP parameters. For this study, three active particle models were chosen based on the significant differences in their underlying assumptions and their popularity in the literature. These three models are the Particle Mono-Layer (PML) model [64], the Particle-Indentation (PI) model [95], and the Particle-Augmented Mixed Lubrication (PAML) model [84]. One should note that it is difficult to achieve a fair comparison of the three models as each has a different approach for calculating the contact mechanics

between the wafer and the pad. Therefore, we applied the contact mechanics approach of one model (PAML) to each of the active particle models. We did this to ensure that the difference in contact mechanics approaches did not overshadow the differences in the active particle models. In this way, a fair comparison could be made among the three models' predictions for active particles.

2.0 DESCRIPTION OF MODELS TO PREDICT ACTIVE PARTICLES

In this section, each of the three active particle models are described. The assumptions which are used to create them are detailed as well as the implications those assumptions have in the model's ability to predict the number of active particles (N_{act}) during CMP. As a part of each model's prediction, the total number of particles in the interface (N_{all}) and the number of eligible wear particles (N_{elig}) were calculated. Calculations for those quantities are described in this section.

2.1 The Particle Mono-Layer (PML) Model

Detailed by Zhao and Chang [64], the Particle Mono-Layer (PML) model is explored as a method to predict the number of active particles during CMP (N_{act}). In this approach, the spatial distribution of particles in the slurry is assumed to be uniform. Only the top surface of this particle distribution, a thin mono-layer of particles closest to the wafer, can be eligible to contribute to the wear process. This set of eligible particles is denoted by stripes in Fig. 2. Particles in the mono-layer which occupy the real contact area between the wafer and the pad are actively involved in the wear process and are deemed "active". These particles are denoted as filled-in circles in Fig. 2.

Fig. 2

The remaining, “inactive” particles reside in the space between the wafer and the pad that is not within the real contact area as denoted by un-filled circles in Fig. 2. It is important to note that it is assumed in this model that the presence of particles between the wafer and the pad does not influence the real contact area. In other words, the particles do not cause separation between the wafer and the pad as they do in the Particle Indentation (PI) model. In the PML model, the size of the particles is only characterized by the average radius, a , of all particles. The mathematical formulation for this theory is produced in Eqs. 3,4 and 5. In Eq. 3, the total number of particles in the interface is calculated. In this formula, the solid fraction of the slurry is designed as ϕ and is a CMP process parameter. The volume between the wafer and the pad that can be filled with slurry is determined by the contact mechanics and is designated by the term Vol_{all_PML} . Finally, the volume of the particle, calculated based on spherical particles of average radius a , is used in Eq. 3. N_{all_PML} , the total number of particles in the interface predicted by the PML model, is calculated based upon the total volume in the interface. Though N_{all_PML} was not explicitly calculated in the original work of Zhao and Chang [64], this calculation is a logical extension of the methodology they have presented for calculating the number of active particles. N_{all_PML} is calculated in Eq. 3 where ϕ is the slurry solid fraction and $Vol_{partAVG}$ is the volume of the average particle in the interface. The importance of calculating the total number of particles in the interface is clear as any active particles will be a fraction of this number. Moreover, the number of particles predicted in the interface serves as a good initial comparison for the active particle models as it is independent of some of the complexities that determine whether or not a particle is active.

$$N_{all_PML} = \phi \left(\frac{Vol_{all_PML}}{Vol_{partAVG}} \right) \quad [3]$$

According to PML model, to calculate the number of particles in the domain which are eligible to become active (N_{elig_PML}) it is necessary to first calculate the line-density of the particles assuming a uniform distribution. The line density of the particles, λ , is the number of particles per unit distance. This is calculated based upon the solid fraction and is presented in Eq. 4.

$$\lambda = \left(\frac{\phi}{Vol_{partAVG}} \right)^{1/3} \quad [4]$$

λ^2 is then the areal density of particles, or the number of particles per unit area. The only particles which are eligible to become active are in the thin mono-layer across the face of the wafer. To calculate these, the areal density is multiplied by the nominal contact area, A_{nom} (Eq. 5).

$$N_{elig_PML} = \lambda^2 * A_{nom} \quad [5]$$

Finally, to calculate the total number of active particles for this model, a similar approach is used in which the areal density of particles, λ^2 , is multiplied by the real contact area, A_{real} . This process is shown in Eq. 6.

$$N_{act_PML} = \lambda^2 * A_{real} \quad [6]$$

A_{real} is calculated based upon the contact mechanics between the wafer and the pad. Details about how the contact mechanics between the wafer and the pad were solved in the current study are provided in section 3.

2.2 The Particle-Indentation (PI) Model

The Particle-Indentation (PI) model is a component of the seminal CMP material removal model introduced by Lou and Dornfeld in 2001 [95]. In the current work, the model is termed “particle-indentation” because the closest approach of the pad and the wafer is determined by the indentation of the particles into the surfaces.

The total volume occupied by the slurry, Vol_{all_PI} , is calculated as the product of the average separation distance between the wafer and the compressed pad, h , and the nominal contact area, A_{nom} .

$$Vol_{all_PI} = A_{nom} * h \quad [7]$$

Unlike the PML model, it is assumed that the slurry occupies this entire volume despite the physical presence of asperities. From Vol_{all_PI} , the total number of particles in the domain, N_{all_PI} , can be calculated in the same manner as Eq. 3 using the average particle diameter.

$$N_{all_PI} = \phi \left(\frac{Vol_{all_PI}}{Vol_{partAVG}} \right) \quad [8]$$

The eligible particles in the domain, those which have the potential to become active, are only a fraction of the total number of particles in the domain. To calculate N_{elig_PI} , a few tasks are performed. First, it is necessary to calculate the number of asperities which are in contact with the wafer. Then, the volume of these asperities is calculated. In this model, it is assumed that particles which would have been in the volume occupied by these asperities are pushed against the wafer.

Therefore, N_{elig_PI} is equal to the volume of the asperities in contact with the wafer, Vol_{asp} , multiplied by the number of particles per unit volume. The number of particles per

unit volume is the slurry solid-fraction divided by the volume of the average particle. This calculation is seen in Eq. 9.

$$N_{elig_PI} = \phi \left(\frac{Vol_{asp}}{Vol_{partAVG}} \right) \quad [9]$$

Notably, in the PI model, the effects of a polydispersed slurry are incorporated. The closest approach of the pad and the wafer is limited by the presence of the largest particle. As the asperities of the pad approach the wafer, the particles between them (those that are part of N_{elig_PI}) begin to transmit the load between the approaching surfaces. The largest particle will make contact with the wafer and the pad first. However, due to surface deformation, the larger particle will indent into both the wafer and the pad. An image of this scenario is depicted in Fig. 3.

Fig. 3

In Fig. 3a, the inactive, eligible, and active particles in the PI model are displayed. In Fig. 3b, it can be seen that the asperity of the wafer and the pad are separated by a large particle. The applied pressure on the wafer causes this particle to indent into the wafer and the pad. The combined indentation, Δ_{tot} , is the sum of the particle's indentations into the wafer, Δ_1 , and pad, Δ_2 , respectively. Therefore, the closest approach of the wafer and the pad, t , can be calculated from Eq. 10 where a_{max} is the maximum radius of a slurry particle.

$$t = 2a_{max} - \Delta_{tot} \quad [10]$$

Because the wafer and the pad are only able to approach to within a distance of t , any particle with a diameter less than t is assumed to be inactive. As a result, the number of active particles depends on many CMP parameters such as the wafer and pad's mechanical properties, the applied load during CMP, and the particle size distribution in the slurry. In this model the size distribution of the particles in the slurry are assumed to be Gaussian. A cumulative distribution function (CDF), $F(t)$, is applied to the particle size distribution to determine the probability, Ω , that a particle will have a diameter greater than t .

$$\Omega = 1 - F(t) \quad [11]$$

Therefore, the number of active particles is the product of the number of eligible particles in the gap (Eq. 9) and the probability that a particle will be greater than the minimum approach, t , of the wafer and the pad.

$$N_{act_PI} = N_{elig_PI} * \Omega \quad [12]$$

2.3 The Particle-Augmented Mixed Lubrication (PAML) Model

As an alternative to the two previous analytical models, a computational modeling approach is explored called the Particle-Augmented Mixed Lubrication (PAML) model which was originally developed by Terrell and Higgs [84]. PAML is a multi-physics computational model which combines contact mechanics, fluid mechanics, and particle dynamics to predict wear during CMP. Contact mechanics in PAML are simulated using a Winkler elastic foundation applied to three-dimensional surface elements, termed “voxels”. The voxels are used to represent the asperities of the wafer and pad surfaces. Fluid mechanics in PAML are simulated using three-dimensional computational fluid

dynamics (CFD). Momentum exchanged in particle-particle and particle-surface collisions is calculated using a particle dynamics solver. Much like the PML and PI models, PAML designates active particles as those which are mechanically loaded between the wafer and the pad. However, in contrast to those two analytical models, PAML does not assume the locations of the particles, but determines them by the physics governing the contacting surfaces, fluid motion, and particle dynamics.

Initially in the PAML simulation, the wafer and the pad are brought into contact. The asperities of the wafer and pad deform until they fully support the applied load. At that point, particles are injected into the volume between the wafer and the pad. Like the PI model, the particle radii are prescribed in a Gaussian distribution. The maximum particle radius, a_{\max} , from this distribution is used to calculate the total number of particles in the domain, $N_{\text{all_PAML}}$. To calculate $N_{\text{all_PAML}}$, the separation distance between each discretized pad asperity and the wafer height is calculated. This height will be referred to as H_i where the subscript represents the discretized asperity for which the distance is calculated. An image of how H_i is determined is shown in Fig. 4a.

Fig. 4

For each H_i , the total number of particles that could fit into this space stacked on top of each other is calculated (N_{H_i}). N_{H_i} is summed over all of the discretized asperities, voxels, and scaled by the slurry solid fraction to calculate $N_{\text{all_PAML}}$. This is seen in Eq. 13 where i_{\max} is the total number of voxels.

$$N_{\text{all_PAML}} = \phi \sum_i^{i_{\max}} N_{H_i} \quad [13]$$

Once the total number of particles is calculated, their locations are determined by randomly seeding them in the domain in places where they do not overlap with the discretized asperities or the other particles. At that point, the simulation is started. During the simulation, the pad is moved under the wafer at a prescribed velocity. The drag force on the particles, calculated from the CFD, advects the particles around the CMP interface. Collisions between particles and the surfaces of the wafer and the pad are handled by the particle dynamics code. Similar to PML and PI models, when a particle is found to be mechanically loaded between the surface of the wafer and the pad it is designated an active wear particle. The difference in the PAML model is that the phenomena which bring the particle into the interface is the result of first principles.

2.4 Model Comparison Methodology

In this section, the methods used to compare the three active particle models and the CMP input parameters are described. The contact mechanics between the wafer and the pad are a critical aspect of all three models. However, in the works which introduced each active particle model, the contact mechanics are performed differently. To separate the assumptions associated with the wafer-pad contact mechanics from the assumptions used in calculating the number of active particles, each of the models was compared using the same wafer, the same pad, and the same contact mechanics methodology. It was decided to use the PAML model's contact mechanics algorithm since data, such as the mean asperity height and the stress on each asperity, are natural outputs from the PAML model. Moreover, the PAML contact mechanics algorithm has been shown to suitably model contact mechanics for micron-scale contacts, such as those in CMP [84].

The pad surface was generated from a prescribed Gaussian asperity distribution with a mean asperity height of 10.5 μm and a standard deviation of asperity heights of 4.7 μm (Fig. 5). The wafer surface was assumed smooth for all three models.

Fig.5

Each of the input parameters for the models was matched for comparison. These parameters can be found in Table 1.

Table 1

In three separate case studies, wafer-pad relative velocity, the standard deviation of particle diameters, and the elastic modulus of the pad were varied to compare the models. For each model, the total number of particles predicted to be in the interface (N_{all}), the total number of eligible particles (N_{elig}), and the total number of active particles (N_{act}) were calculated.

The PAML model simulations were performed on a PowerWulf™ computing cluster. Each of the 4 nodes of the cluster contains two dual-core AMD Opteron™ 2.2 GHz processors, and 4 GB ram per core. Each PAML simulation required approximately 120 hours of computation time to complete.

3.0 RESULTS AND DISUCSSION

Predictions from each of the three models were generated over the range of parameters varied during the case studies. The prediction of the number of particles within the

nominal contact area (N_{all}), the prediction of the number of eligible active particles (N_{elig}) and the prediction of the number of active particles (N_{act}) are discussed in this section.

3.1 The Number of Particles within the Nominal Contact Area

The number of active particles can only be a fraction of the total amount of particles contained within the nominal contact area of the wafer-pad interface. As such, the results from each active particle model were first used to determine the total number of particles in the wafer-pad interface. Case studies were performed to assess the model's dependence on the standard deviation of particle sizes and the pad's elastic modulus. The results for the PAML model were multiplied by 10 for graphical clarity in Fig. 6a. and Fig. 6b.

In Fig. 6a, the effect of varying the standard deviation of the particle diameters is presented.

Fig. 6

It should be mentioned again that although the standard deviation of the particle diameters is changing, the average particle size remains the same. For the baseline conditions in which the standard deviation of particle diameters is $0.086\ \mu\text{m}$, the number of particles estimated by the PAML model is approximately an order of magnitude less than the numbers predicted by the PML and PI models. The reason for this difference lies in the fact that the PAML model uses the solid fraction of the slurry as a scaling factor to determine how many particles should be seeded in the domain. In contrast, the PML and PI models use the solid fraction to calculate the number of particles in the domain based

upon the volume under the compressed pad. The PML and PI models are similar in their predictions of the number of particles in the interface. Both models show no dependence on the standard deviation of the particle diameters. This is because, the PML and PI models only use the average particle size to calculate the number of particles in the interface. Therefore, even though the minimum and maximum particle size is changing with the standard deviation of particle diameters, the average particle size is the same. However, there is a dependence on particle diameter standard deviations in the PAML model. It can be seen that the results of the PAML model vary with particle diameter standard deviation. The PAML model seeds particles based upon the maximum particle diameter. For the same mean particle size, increases in the standard deviation result in increases in the maximum particle size. As the particle size is increased, fewer particles will fit in the domain. This is displayed by the decreasing trend in Fig. 6b for the PAML model.

The number of particles in the domain under varying pad elastic moduli is presented in Fig. 6b. As the pad's elastic modulus increases, so does its ability to resist deformation from the applied load of the wafer. Less pad deformation results in less real contact area and more volume under the wafer for slurry to occupy. It can be seen in this study that for all three models, an increase in the pad's elastic modulus results in more particles in the domain for a constant load. For the PML and PI models, the reason this occurs is because more volume is present under the wafer for slurry to occupy as the pad's elastic modulus increases. More volume results in more particles for the same given slurry solid fraction and abrasive particle size. The results from the PAML model predict a similar phenomenon but are about an order of magnitude lower because the PAML model uses

the solid fraction as a scaling parameter instead of using it in a volume-based seeding calculation as described by Eqn. 13.

3.2 The Number of Eligible Particles

Though there are a number of particles in the domain (N_{all}), only a fraction of these are eligible to become active. Establishing the number of particles eligible to become active is a method to get closer to predicting the number of active particles in the domain which is used in CMP modeling. In this section, the prediction of the number of eligible particles to become active (N_{elig}) is provided for varying particle diameter standard deviations, and pad elastic moduli.

In Fig. 7a, N_{elig} is presented for all three models. By comparing Fig. 7a to Fig. 6a, it can be seen that the number of eligible particles predicted by the three models is closer than the amount of total particles predicted in the domain. The reason for this similarity is that the PI model makes the rather restrictive assumption that all eligible particles reside in the volume of the contacting asperities (Eq. 9). Suggested by the large magnitude of the PML model's N_{elig} prediction, the PML model is less restrictive. This is because any particle in the mono-layer on the top surface is eligible to become active. It should be noted that for each case, the N_{elig} for PAML is the same as the N_{all} for PAML because in the PAML modeling framework, every particle is eligible to become active.

Fig. 7

The effect of variation in particle diameters is shown in Fig. 7a. This graph is similar to Fig. 6a except that it is clear here that the PI and the PAML model prediction's are closer.

When observing the PI and the PML models in Fig. 7a, it can be seen that they do not vary with particle diameter standard deviation. The reason for this is that both the PI and PML models use the average particle for calculating the number of eligible wear particles in the domain.

Once again, increases in the pad's elastic modulus cause a decrease in the amount of real contact area. As depicted in Fig. 7b, each model's prediction for N_{elig} differs. For the PML model, N_{elig} is not a function of the volume in the domain but rather the nominal contact area and the solid fraction (Eq. 5). As a result, $N_{\text{elig_PML}}$ is constant. The PI model produces an interesting prediction for the number of eligible particles in the domain because of the competing effects of volume under the wafer and real contact area. For a low elastic modulus, the number of eligible particles predicted by the PI is low. This is because there is very little gap height (t) which the particles can occupy. There is a spike in the number of eligible particles around 25 MPa because at this elastic modulus there is an ideal combination between having enough separation between the wafer and the pad for slurry to occupy, and having enough real contact area for particles to become eligible. As the elastic modulus of the pad increases further, the number of eligible particles predicted by the PI model decreases. This is explained by the fact that although increases in the pad's elastic modulus cause an increased gap height and increased volume between the wafer and the pad, there is relatively little real contact area. As a result, there are relatively few particles eligible to become active. The PAML model responds as it did for the calculation of the number of particles in the domain (N_{all}). Every particle in the domain for the PAML model is eligible to become active.

In both case studies, the study of the effect of particle diameter standard deviation and the study of the effect of the pad's elastic modulus, the number of eligible particles in the domain (Fig. 7) are much closer than the total number of particles in the interface (Fig. 6). This suggests that even though the models make dramatically different assumptions about the number of particles inside of the CMP interface, they tend toward agreement when predicting the number of particles in the interface which are eligible to become active.

3.3 The Number of Active Particles (N_{act})

The predictions for the total number of particles in the interface and the number of particles eligible to become active have been presented in sections 3.1 and 3.2. In this section, the number of active particles for each model is presented. This value is critical in the estimate of material removal rates during CMP. The prediction from the three models under variation in the particle standard deviation and the pad's elastic modulus is presented. Additionally, the active particle prediction from the three models is also presented for a variation in the relative velocity of the wafer and the pad.

In Fig. 8a, the effect of variation in the standard deviation of particle diameters on the predicted number of active particles is presented.

Fig. 8

Except for the case of zero standard deviation, the PML model consistently predicts a higher number of active particles than the PI or PAML models as shown in Fig. 8a. This

is because the PML model is the least restrictive of the three models as its criteria for a particle to become active depends only on the real contact area. The PI model predicts fairly low amounts of active particles until the standard deviation of particles sizes approaches zero. When the standard deviation approaches zero, the probability of a particle being active (Eq. 12) goes to 100% because the wafer makes contact with all of the eligible particles (N_{elig}) in the domain. Though not displayed in Fig. 8a for clarity, the PI model predicts 127 active particles when the standard deviation of particle sizes is set to zero. It can be seen that, except for this case of identical particle sizes, the PAML model and the PI model produce excellent agreement. Though the PML model has a higher value, it is approximately within an order of magnitude of the PI and PAML models.

The number of active particles versus the pad's elastic modulus was also studied. The results of this study are presented in Fig. 8b. In Fig. 8b, it is clear that the PI and PAML models predict very few active particles for almost all pad elastic moduli studied. In contrast, the PML model predicts many active particles for the low pad elastic moduli. This is because the PML model is heavily influenced by the amount of real contact area. As the pad's elastic modulus is decreased, there is more real contact area for a given load. Though the PI and PAML models are also influenced by the real contact area, these models take into account that an increase in real wafer-pad contact area is offset by a decrease in the number of particles within the interface that are eligible to become active (N_{elig}) due to volumetric considerations. Except for very low pad moduli, the PML model's prediction is approximately within an order of magnitude of the PI and PAML

models. As the pad's elastic modulus increases, the PML model's prediction begins to approach that of the PI and PAML models.

Finally, in Fig. 9, the results of a study to assess the number of active particles predicted with variation in the relative velocity between the wafer and the pad is presented.

Fig. 9

The PI and PML models do not capture transient effects are thus do not show a dependence on the relative velocity between the wafer and the pad. In the PAML model, the effect of increasing the wafer-pad relative velocity causes more momentum to be transferred to the fluid which helps to advect particles in the interface. It should be noted that the prediction from the PAML model falls within the predictions of the PI and PML models. For slow relative velocities, the PAML model agrees mostly with the PI model. However, as the relative velocity increases, the PAML predicts a higher number of active particles which trends toward the PML model.

The active particle calculations presented in this work provide a comparison of three different approaches. Experimental data to determine the number of active particles for realistic CMP parameters is particularly challenging to obtain. Not only do the nanoparticles have to be visualized, but there also has to be some method of determining, in situ, if the particles are actively removing material from the wafer. Lei et al. have recently made an effort to provide an understanding of particulate motion in the wafer-pad interface through experiments [113]. In their work, a slurry was used to polish a glass slide that simulated the wafer. A microscope was employed to image the slurry particles and the particle trajectories were determined by particle tracking algorithms. Based on

the analysis of the trajectories, Lei et al. were able to distinguish if a particle was following the motion of the pad (and thus trapped between the wafer and pad) or if the particle was moving freely in the slurry fluid. Assuming that their findings directly correlate to physical CMP experiments for the purposes of this work, the total number of particles between the wafer and the pad would be N_{all} . Lei et al. assumed that the particles which followed the trajectory of the polishing pad were pressed between the wafer and the pad. If this is the case, those particles would be the active particles (N_{act}) given the criteria for determining active particles in the PML, PI, and PAML models. Because all of the models studied in the current work consider the amount of real contact between the wafer and the pad to affect the number of active particles, a case was chosen in which the ratio of real contact area to nominal contact area was about half which is close to the 40% ratio approximation presented in Lei et al. The results from the three models and the experimental results from Lei et al. are provided in Fig. 10.

Fig. 10

In Fig. 10, it can be seen that Lei et al. observed approximately 50% of the particles in the interface to be “active”. For the PML, PI, and PAML models, the values in Fig. 10 are the ratio of the total amount of particles in the domain (N_{all}) to the number of active particles (N_{act}). Though the models are not too far off from each other, all of the models predict a value less than the experimental result. There are many reasons for this to be the case. First, the experimental results suggest that any particle following the circular motion of the pad could be active. Though this is likely the case for many particles, some particles may also be settled on the pad or embedded in a pad depression making them close to the wafer but not pressed into it. If these particles could be distinguished, the

active particle measurement from the experiment may be attenuated. Also, as is evident by the results in the current manuscript, other aspects such as the particle size distribution and relative velocity of the pad and the wafer (not all of which were available from the experiment) will affect the number of active particles. Moreover, the experimental setup used by Lei et al. was not a traditional CMP setup. A few of the differences include; (1) the polishing pad was 16 mm in diameter, (2) there was no flow of fresh slurry entering the wafer-pad interface (3) the “wafer” was a stationary glass slide instead of a rotating wafer, and (4) there are a number of CMP parameters varied during actual CMP which were not varied during this experiment. Nonetheless, Fig. 10 encourages the development and experimental validation of active particle models that can quantitatively predict the results from active particle experiments. As a final note about this experimental comparison, though the causes of this are not yet definitive, it was seen during the experiments of Lei et al. that the percentage of active particles may be strongly correlated to the polishing time. This suggests that it would be beneficial to have active particle models which can capture transient effects.

4.0 CONCLUSION

In this work, the number of active wear particles predicted in the wafer-pad interface was presented for three different CMP models. The models studied were the Particle Mono-Layer (PML), the Particle Indentation (PI), and Particle-Augmented Mixed Lubrication (PAML) models. The PML model is purely analytical. The PI model is analytical but has a statistical component. The PAML model is fully computational. In addition to the number of active particles (N_{ect}), the number of particles within the CMP domain (N_{all})

and the number of particles eligible to become active (N_{elig}) were considered. Each of the models makes vastly different assumptions in the prediction of N_{ect} , N_{all} and N_{elig}

It was found that there was little agreement between the models in their prediction of N_{all} . Better agreement was found among the models in their prediction of N_{elig} . Surprisingly, the prediction of N_{act} was in relatively good agreement considering the discrepancies in the N_{all} and N_{elig} predictions. The difference among the models in their prediction of the total number of particles in the domain (N_{all}) was roughly a factor of 20 for the parameters studied (Fig. 6). To start with such a large difference and get to the N_{act} predictions that are mostly in agreement for the PI and PAML models and only about a factor of 7 off for the PML model is quite remarkable (Fig. 8). What this indicates is that although the assumptions by each model's original authors are dramatically different, the models still converge around the low active particle counts in Fig. 8. There is a danger here in that the reader may conclude that one can use any of the models and get reliable results. However, getting seemingly accurate quantitative results for a limited number of scenarios may yield wildly varying results when the CMP regime or process parameter combinations change. Thus, it is important that models which reconcile themselves with as many CMP physics modes as possible (or at least the physics modes deemed most critical by experiments), be developed. This is the only way that accurate and reliable CMP models can emerge from the community.

Assuming identical contact mechanics treatments as was done in this study, the observed agreement among the models is promising as the number of active particles during CMP is a critical parameter in the quantitative prediction of material removal during CMP. However, because of the different assumptions made in each of the models for predicting

N_{all} , N_{elig} , and N_{act} , it seems that this issue is not fully resolved. Ideally, each of the models would have better agreement not only in the prediction of N_{act} , but also N_{all} , and N_{elig} as well. As such, it seems that the assumptions made in predicting these quantities should be in agreement as well. Additionally, although the difference among the models was less for the prediction of N_{act} than for the prediction of N_{all} , the differences in the prediction of N_{act} are still significant. If Eq. 1 were used to predict the MRR, the relatively small differences in the model's predictions can result in dramatic differences in the quantitative prediction of material removal rates. It must also be noted that the PAML model, which takes into account the transient effects and the flow physics of the slurry, was shown to be able to account for changes in the relative velocity between the wafer and the pad. Moreover, the multi-physics computational approach taken by the PAML model makes it well-poised to account for critical CMP parameters such as changes in slurry viscosity and particle-particle interaction when predicting the number of active particles in CMP. However, the PAML model is computationally expensive. Enhancing its computational efficiency may lead to a high-fidelity, wafer-scale CMP model that may help to answer questions about particle entrainment into the wafer-pad interface to provide a more complete understanding of N_{act} and N_{all} predictions. Finally, this paper highlights the value of quantitative validation of N_{act} and N_{all} through experimental methods. Though there have been several papers which investigate the motion of the slurry in the wafer-pad interface experimentally[113, 131, 132], more attention put toward techniques to determine active particles, at CMP scales, may provide critical information with which these active particle models can be validated.

ACKNOWLEDGMENTS

We would like to thank the National Aeronautics and Space Administration (NASA) Graduate Student Researchers Program (GSRP) and the Alfred P. Sloan Foundation for supporting the first author. This work was also partially sponsored by the NSF CAREER award (#0645124) from the CMMI division.

Tables:**Table 1.** CMP input parameters

| | |
|---------------------------------------|--------|
| Pad Properties | |
| Hardness (MPa) | 5 |
| Elastic Modulus (MPa) | 50 |
| Poisson's Ratio Pad | 0.2 |
| Copper Wafer Properties | |
| Hardness (MPa) | 2000 |
| Elastic Modulus (MPa) | 50000 |
| Poisson's Ratio Wafer | 0.35 |
| Slurry Properties | |
| Particle Material | Silica |
| Particle Elastic Modulus (MPa) | 73000 |
| Particle Density (kg/m ³) | 2000 |
| Particle Radius (μm) | 0.272 |
| Particle Diameter Std. Deviation (μm) | 0.086 |
| Poisson's Ratio Particle | 0.17 |
| Fluid Density (kg/m ³) | 1000 |
| Fluid Viscosity (kg/m s) | 0.001 |
| Solid-Fraction | 0.04 |
| CMP Parameters | |
| Nominal Area (μm ²) | 625 |
| Down Pressure (psi) | 6 |
| Relative Velocity (m/s) | 0.4 |

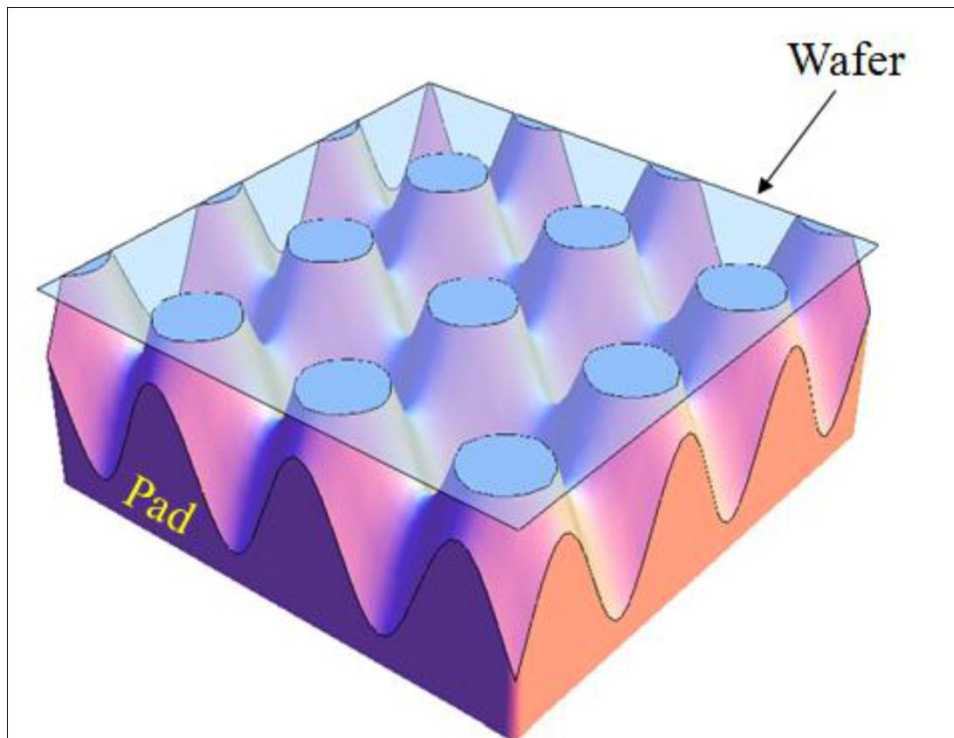


Figure 1 The relatively smooth wafer contacting the asperities on the rough polishing pad

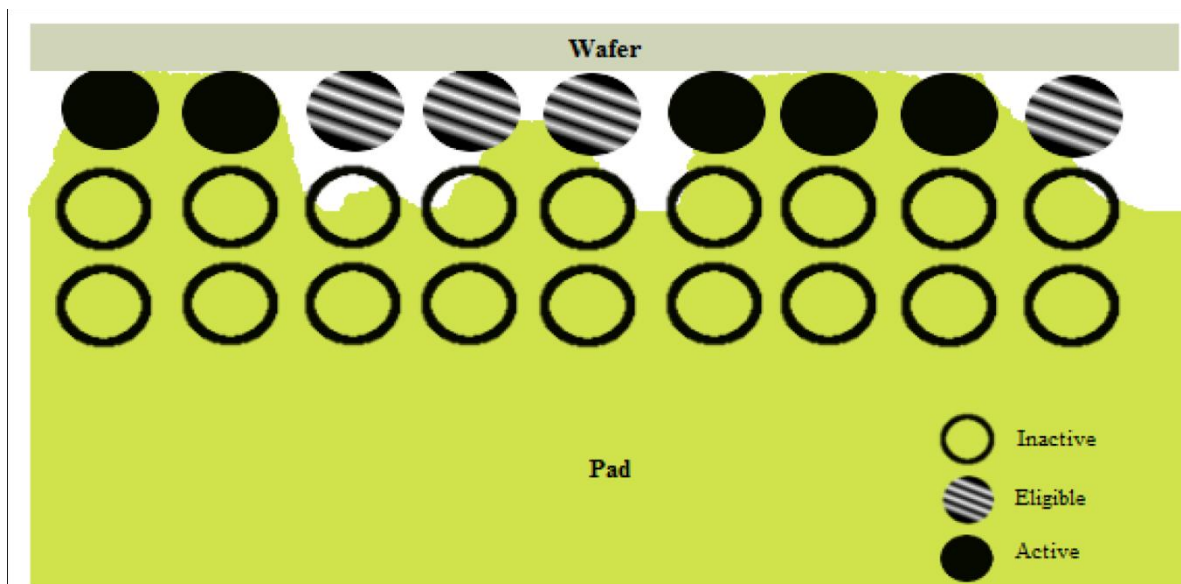


Figure 2 Particle Mono-Layer Model

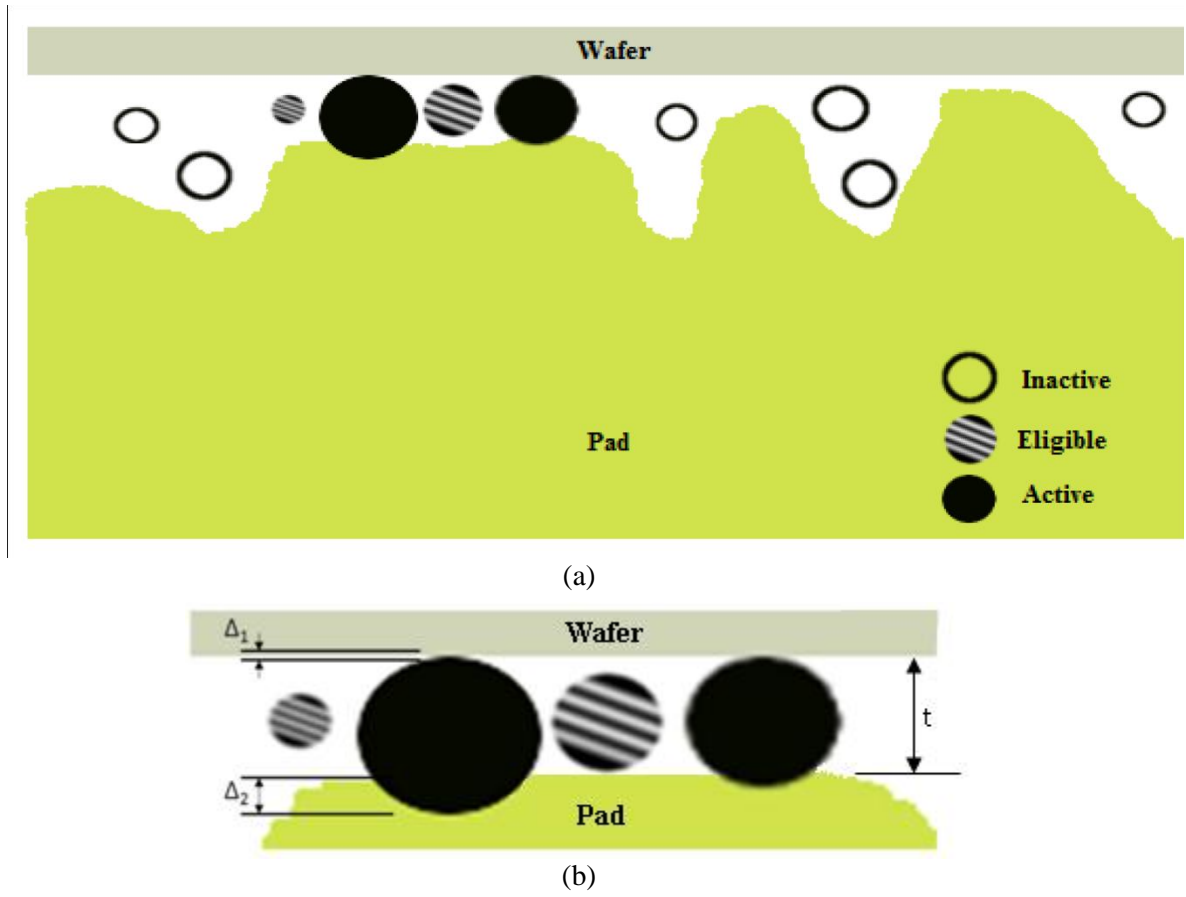
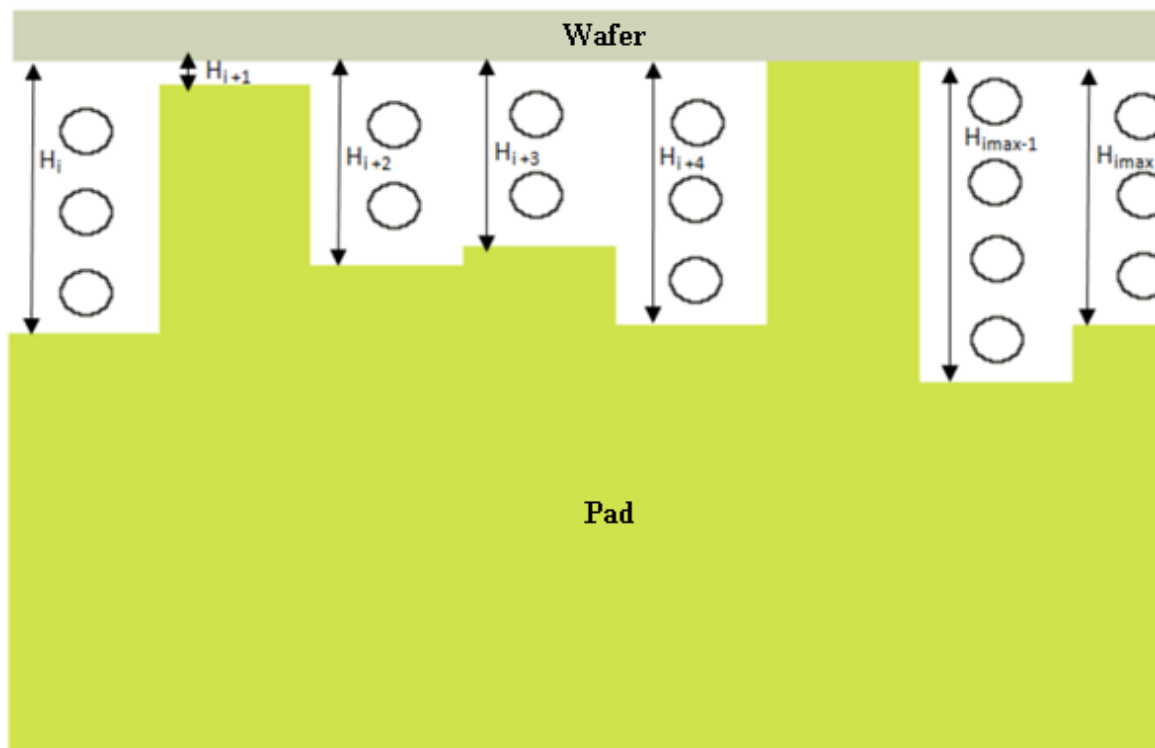
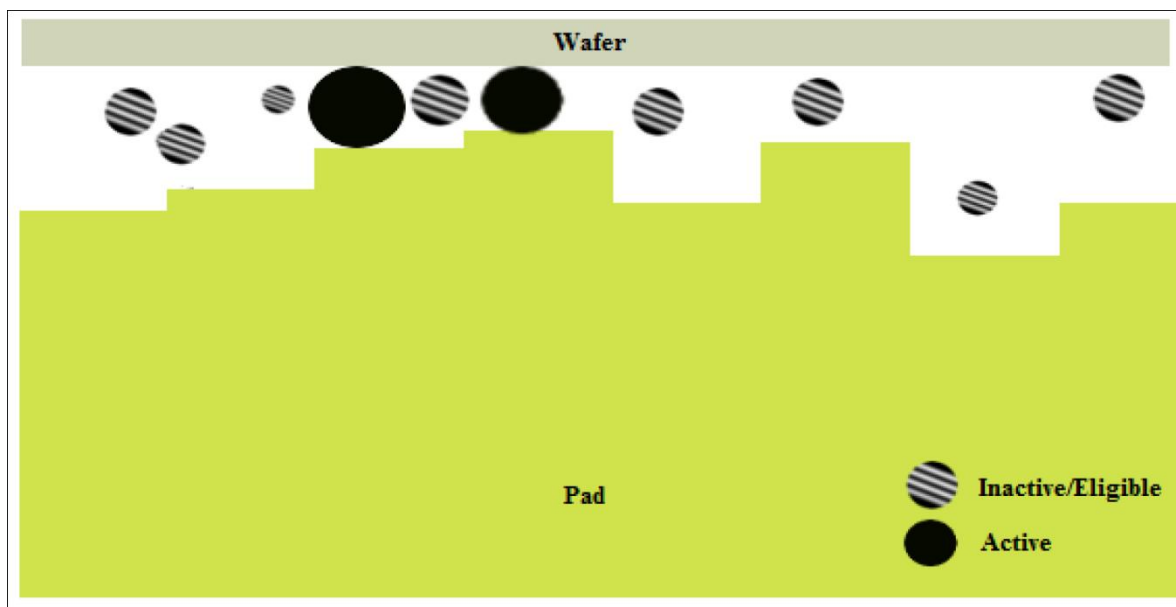


Figure 3 Particle-Indentation model: (a) view of active inactive particles (b) detailed view showing indentations Δ_1 and Δ_2



(a)



(b)

Figure 4 Diagram of PAML model displaying particles in the interface (a) Method used to seed particles in PAML. (b) An imaged showing the determination of active particles in PAML.

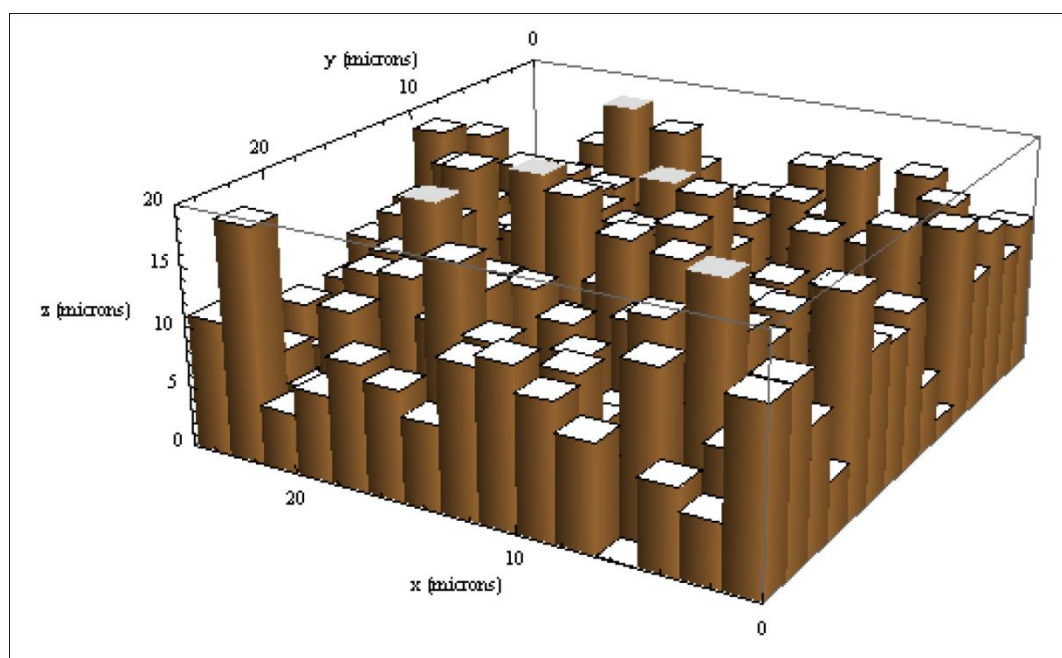
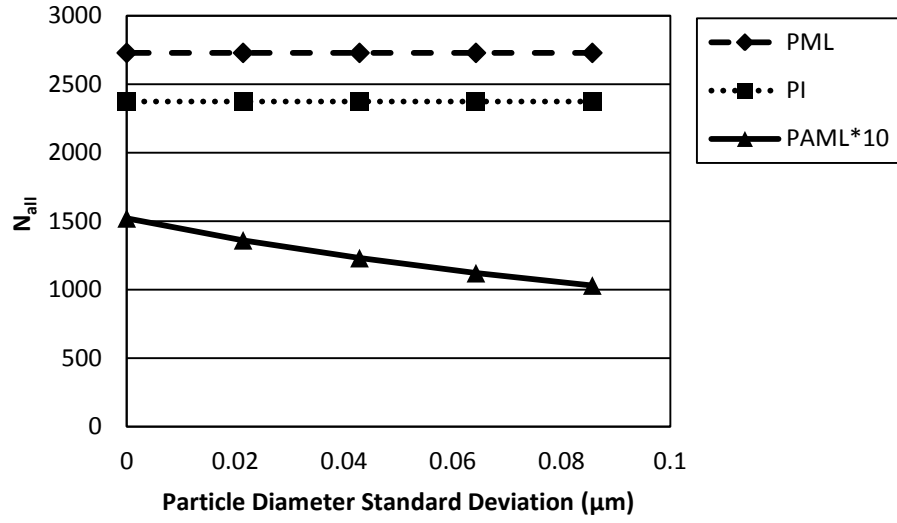
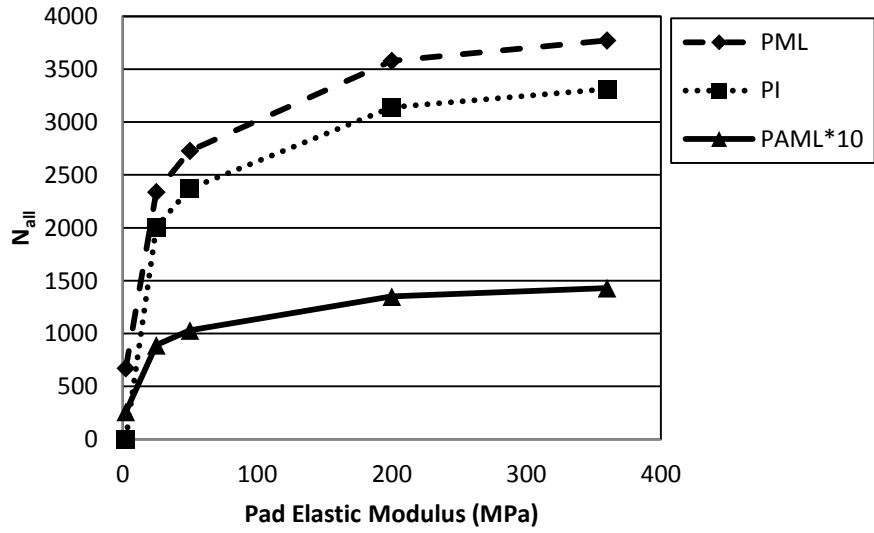


Figure 5 The pad used to compare all models

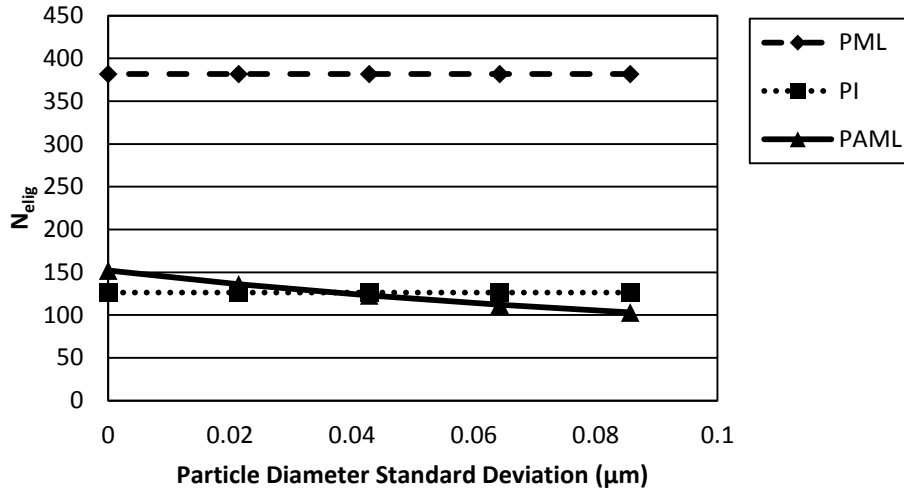


(a)

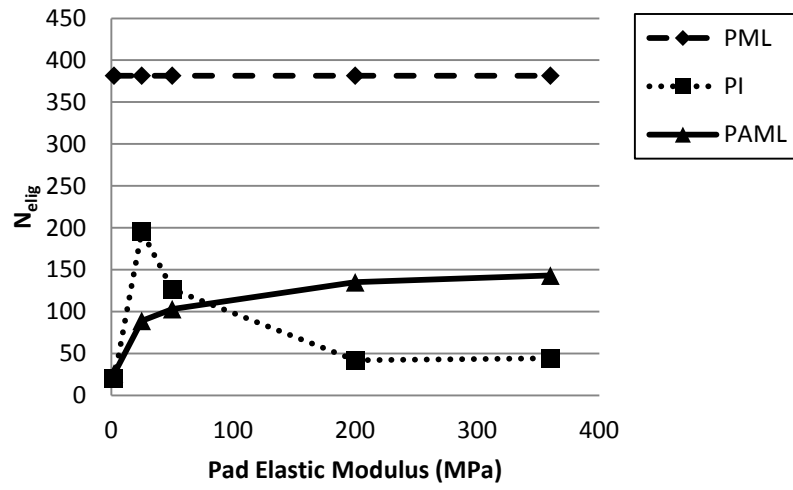


(b)

Figure 6 The total number of particles in the wafer-pad interface. (a) Predictions from the three models with variation in particle diameter standard deviation. (b) Predictions from the three models with variation in the pad's elastic modulus

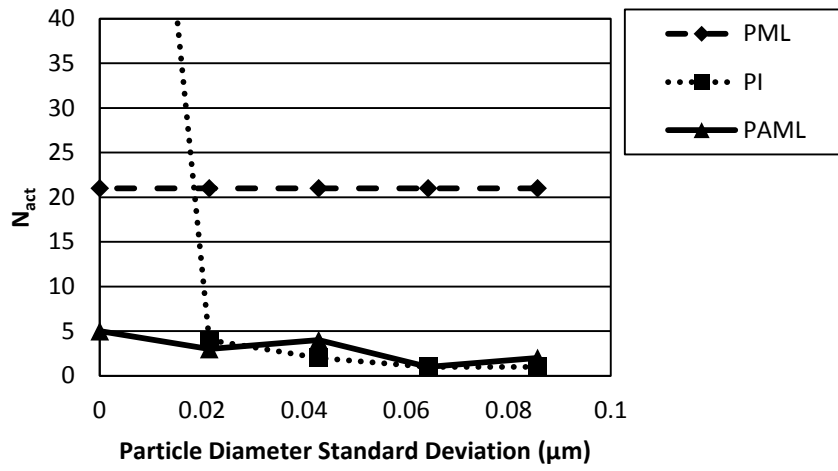


(a)

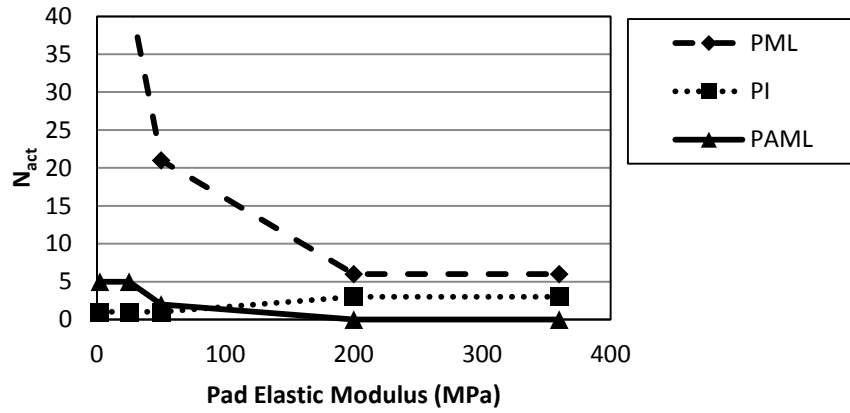


(b)

Figure 7 The total number of eligible wear particles in the wafer-pad interface. (a) Predictions from the three models with variation in particle diameter standard deviation. (b) Predictions from the three models with variation in the pad's elastic modulus



(a)



(b)

Figure 8 The total number of active wear particles in the wafer-pad interface. (a) Predictions from the three models with variation in particle diameter standard deviation. (b) Predictions from the three models with variation in the pad's elastic modulus

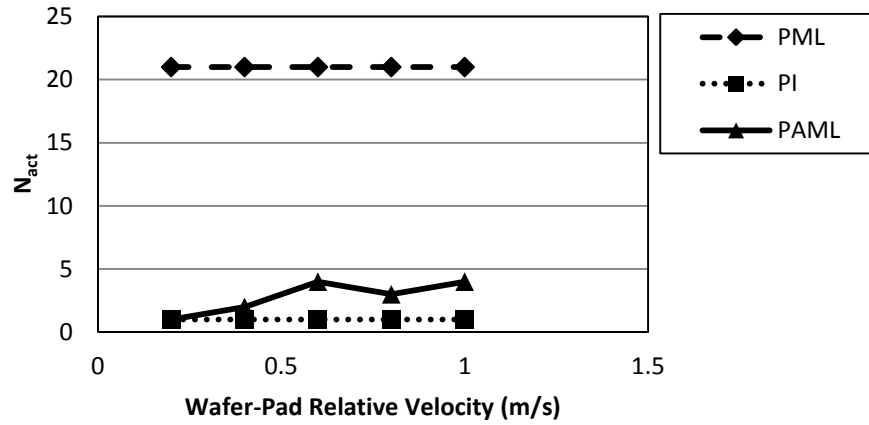


Figure 9 The total number of active wear particles in the wafer-pad interface with variation in the relative velocity between the wafer and the pad.

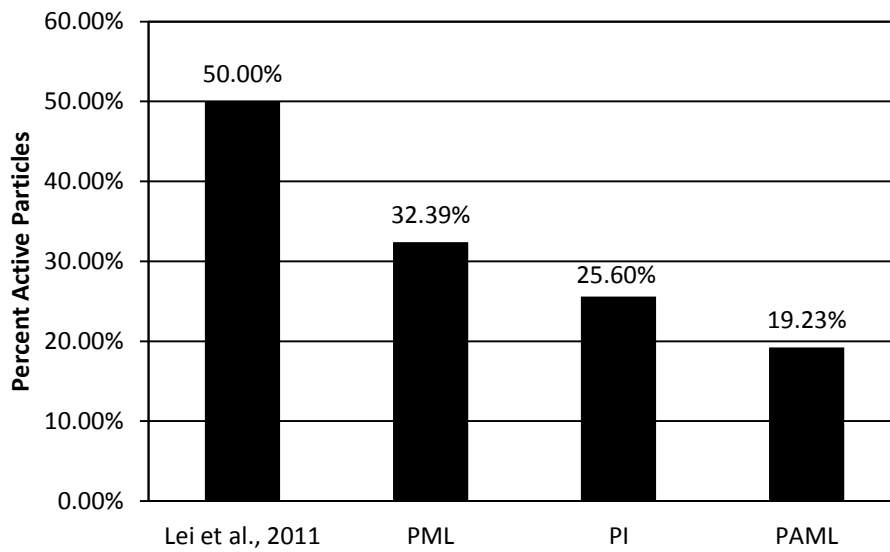


Figure 10 A comparison of the active particle models to the experimental results from Lei et al.

Figure Captions:

Figure 1 The relatively smooth wafer contacting the asperities on the rough polishing pad

Figure 2 Particle Mono-Layer Model

Figure 3 Particle-Indentation model: (a) view of active inactive particles (b) detailed view showing indentations Δ_1 and Δ_2

Figure 4 Diagram of PAML model displaying particles in the interface (a) Method used to seed particles in PAML. (b) An imaged showing the determination of active particles in PAML.

Figure 5 The pad used to compare all models

Figure 6 The total number of particles in the wafer-pad interface. (a) Predictions from the three models with variation in particle diameter standard deviation. (b) Predictions from the three models with variation in the pad's elastic modulus

Figure 7 The total number of eligible wear particles in the wafer-pad interface. (a) Predictions from the three models with variation in particle diameter standard deviation. (b) Predictions from the three models with variation in the pad's elastic modulus

Figure 8 The total number of active wear particles in the wafer-pad interface. (a) Predictions from the three models with variation in particle diameter standard deviation. (b) Predictions from the three models with variation in the pad's elastic modulus

Figure 9 The total number of active wear particles in the wafer-pad interface with variation in the relative velocity between the wafer and the pad.

Figure 10 A comparison of the active particle models to the experimental results from Lei et al.

Appendix 3: “Kicking up some dust” – An Experimental Investigation Relating Lunar Dust Erosive Wear to Solar Power Loss

Wear was a critical problem caused by the sharp and jagged lunar dust particles during the Apollo missions of the 1960's and 1970's [133]. Understanding the effect that lunar dust erosive wear can have on lunar hardware is critical for future plans to return to the Moon. In particular, optical components such as solar concentrators, lenses, and mirrors, are uniquely susceptible to such damage. The change in surface roughness caused by lunar dust particle impingement on these components can affect their reflectance and transmittance resulting in a severe losses in performance [134]. Solar concentrators are devices which collect sunlight over large areas and focus the light into smaller areas for the purposes of heating and energy production. In the current work, a laboratory-scale solar concentrator was subjected to erosive wear by the JSC-1AF lunar dust simulant. The concentrator was focused on a photovoltaic cell and the degradation in electrical current, due to the erosive wear, was measured.

EXPERIMENTAL METHODS

Erosive wear tests were conducted in the Erosion Laboratory at the NASA Glenn Research Center. A TOPAS[®] Solid Aerosol Generator was used to aerosolize the particles. A laboratory-scale solar concentrator was created by using a stainless-steel parabolic dish that was approximately 4 inches in diameter.

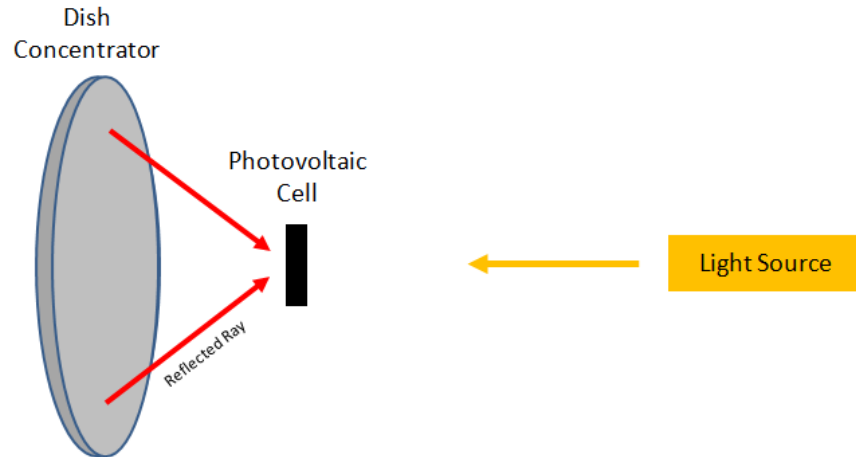
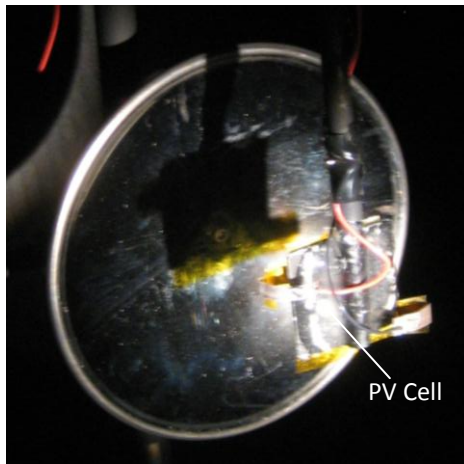


Fig. 1 Schematic of the concentrator and PV cell configuration

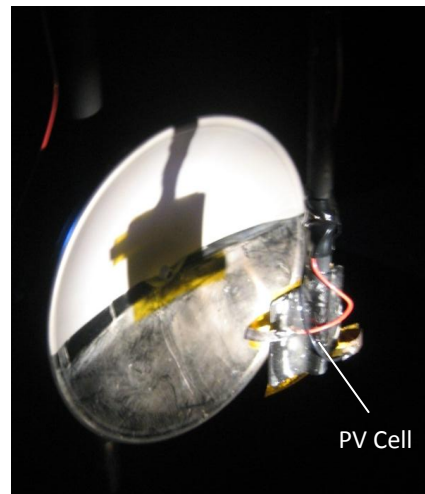
Aerosolized JSC-1AF lunar dust simulant particles were accelerated toward the solar concentrator by a secondary fast-moving air stream. Each quarter of the concentrator received four minutes of exposure to erosive wear. After being exposed to erosive wear, the concentrator was gently cleaned with a solvent. A dual-disc tool was used to determine that the average impact velocity of the particles in the current study was approximately 105 m/s. The 105 m/s impact velocity in the current study is moderate compared to the numerical predictions of Lane et al. who estimated particle velocities in excess of 1000 m/s [135] in lunar conditions. The results in the current study represent a less-severe scenario than what may be experienced on the lunar surface. Even at the moderate velocities used in this study, these tests provide important data which can help to determine the susceptibility of lunar hardware to performance degradation when exposed to lunar dust erosive wear. A photovoltaic (PV) cell was used to determine the effectiveness of the solar concentrator by measuring the electrical current output before and after erosion. A schematic of the test setup is provided in Fig. 1.

RESULTS AND DISCUSSION

In this section, a quantitative comparison of the effect of erosive wear on the solar concentrator is presented. Portions of the concentrator were masked so that the effect of progressive exposure to lunar dust on the concentrator could be observed. In Fig. 2, an image of the fresh, non-eroded, concentrator is displayed along with a concentrator that has been half-eroded.



(a)



(b)

Fig. 2 Photographs displaying light reflected from the concentrator during test (a) fresh concentrator (b) half-eroded concentrator

It can be seen in Fig. 2, that the non-eroded concentrator reflects light more uniformly than the half-eroded concentrator. On the half-eroded concentrator (Fig. 2b), the distinction between the eroded region and the non-eroded region is clear. It is believed that this distinction is evident because the reflectance from the non-eroded portion of the concentrator in Fig. 2b is more specular in nature and directs most reflected light toward the PV cell. In contrast, the reflectance from the eroded portion of the concentrator is more diffuse and scatters incident light. This also explains why the eroded portion of the concentrator in Fig. 2b is “bright” as diffuse reflectance directs more light toward the camera than the specular reflectance of the non-eroded region.

Electrical power production is higher when more incident light is reflected from the concentrator toward the PV cell. To understand the effects that the erosive wear can have on the efficiency of the concentrator, the current output for the two scenarios depicted in Fig. 2 is compared in Fig. 3. In Fig. 3, it is shown that the current output from the non-eroded concentrator is 12.1 milliamps while the current from the eroded concentrator is 7.2 milliamps. This reduction in electrical current output represents a 40% decrease from the PV cell and would be significant for a future lunar mission.

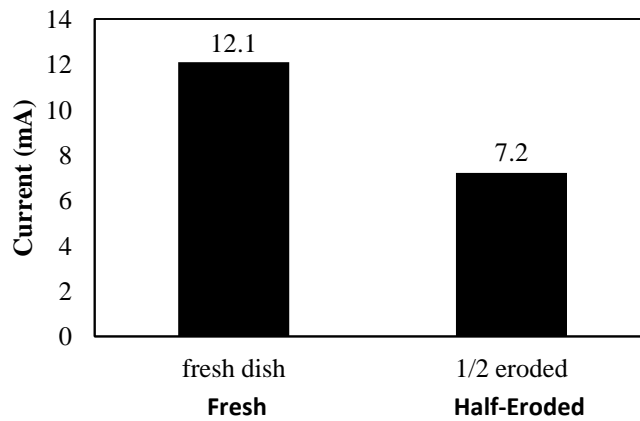


Fig. 3 Electric current output from PV cell for different areas of erosive wear exposure to the concentrator

Conclusion

In this work, erosive wear tests were conducted using the JSC-1AF lunar simulant to assess the potential for lunar dust erosion to degrade the performance of solar concentrators on the Moon. Qualitatively, the surface's optical properties changed as the eroded surface reflected light in a more diffuse manner instead of directing light toward to the photovoltaic (PV) cell. Quantitatively, it was clear that the eroded concentrator was able to produce significantly less electrical current when paired with the PV. The results from this study indicate the need for a better understanding of lunar dust erosive wear on critical surfaces of lunar hardware. The changes in electrical performance presented in this work were significant even for moderate impact velocities and short test durations. The high-velocity impacts in lunar conditions and long-term exposure to lunar dust erosive wear may significantly exacerbate the effect. It is believed that lunar

temperatures, the lunar vacuum, and lunar surface chemistry may have an effect on this phenomenon and more research is needed in these areas. Understanding erosive wear damage on the Moon is critically important for optical surfaces, such as mirrors and lenses, and solar concentrators.

Acknowledgments

The research in this work was supported by the NASA Graduate Student Researchers (GSRP) grant (NNX09AK96H). Additional funding for this work was supplied by the Alfred P. Sloan Foundation. The authors would like to gratefully acknowledge Rick Mondry (NASA Glenn) for his help constructing the experimental rig on which the tests were performed.

References

- [1] Williams, J. A., *Engineering Tribology*: Cambridge University Press, 2005.
- [2] Wang, A. and Essner, A., "Three-body wear of UHMWPE acetabular cups by PMMA particles against CoCr, alumina and zirconia heads in a hip joint simulator," *Wear*, vol. 250, pp. 212-216, 2001.
- [3] Fan, J., Myant, C., Underwood, R., and Cann, P., "Synovial fluid lubrication of artificial joints: protein film formation and composition " *FARADAY DISCUSSIONS*, vol. 156, pp. 69-85, 2012.
- [4] Dowson, D., "Tribological principles in metal-on-metal hip joint design " *PROCEEDINGS OF THE INSTITUTION OF MECHANICAL ENGINEERS PART H-JOURNAL OF ENGINEERING IN MEDICINE*, vol. 220, pp. 161-171, 2006.
- [5] Bron, A. J., Tiffany, J. M., Gouveia, S. M., Yokoi, N., and Voon, L. W., "Functional aspects of the tear film lipid layer," *Experimental Eye Research*, vol. 78, pp. 347-360, 2004.
- [6] Dunn, A., Uruena, J., Huo, Y., Perry, S., Angelini, T., and Sawyer, W. G., "Lubricity of Surface Hydrogel Layers," *Tribology Letters*, vol. 49, pp. 371-378, 2013.
- [7] Prinz, J. F. and Lucas, P. W., "An optimization model for mastication and swallowing in mammals," *PROCEEDINGS OF THE ROYAL SOCIETY B-BIOLOGICAL SCIENCES*, vol. 264, pp. 1715-1721, 1997.
- [8] Mpagazehe, J. N. and III, C. F. H., "A CFD-DEM Model to Predict Rotary Drilling," *Tribology International*, 2012, in preparation.
- [9] Fenske, G., Erck, R., and Demas, N., "DOE/DOD Parasitic Energy Loss Collaboration " Argonne National Laboratory 2012.
- [10] <http://www.epa.gov/oms/climate/documents/420f12063.pdf>, E. P. A.-. Available: <http://www.epa.gov/oms/climate/documents/420f12063.pdf>
- [11] <http://www.eia.gov/petroleum/gasdiesel/>, E. P. A.-.
- [12] Ertel, A. and Grubin, A., "Investigation of Scientific and Industrial Research," Central Scientific Research Institute for Technology and Mechanical Engineering, Moscow 1949.
- [13] Street, K. W., Marchetti, M., Wal, R. L. V., and Tomasek, A. J., "Evaluation of the tribological behavior of nano-onions in Krytox 143AB," *Tribology Letters*, vol. 16, 2004.
- [14] Higgs, C. F. and Worniyoh, E., " An in situ mechanism for self-replenishing powder transfer films: Experiments and modeling " *Wear*, vol. 264, pp. 131-138, 2008.
- [15] Boning, D., Lee, B., Oji, C., Ouma, D., Park, T., Smith, T., and Tugbawa, T., "Pattern Dependent Modeling for CMP Optimization and Control," in *Materials Research Society (MRS) Spring Meeting*, San Francisco, CA, 1999.
- [16] Runnels, S. R., "Advances in physically based erosion simulators for CMP," *Journal of Electronic Materials*, vol. 25, pp. 1574-1580, 1996.
- [17] Nguyen, V., VanKranenburg, H., and Woerlee, P., "Dependency of dishing on polish time and slurry chemistry in Cu CMP," *Microelectronic Engineering*, vol. 50, pp. 403-410, 2000.
- [18] Mpagazehe, J. N., Thukalil, G. A., and III, C. F. H., "A Study to Estimate the Number of Active Particles in CMP," in *Materials Research Society Spring Meeting*, San Francisco, CA, 2009.
- [19] Edwards, J. K., McLaury, B. S., and Shirazi, S. A., "Modeling Solid Particle Erosion in Elbows and Plugged Tees," *Journal of Energy Resources and Technology*, vol. 123, 2001.

- [20] Zantye, P. B., Kumar, A., and Sikder, A. K., "Chemical mechanical planarization for microelectronics applications," *MATERIALS SCIENCE & ENGINEERING R-REPORTS*, vol. 45, pp. 89-220, 2004.
- [21] Nikas, G. K., "A state-of-the-art review on the effects of particulate contamination and related topics in machine-element contacts " *PROCEEDINGS OF THE INSTITUTION OF MECHANICAL ENGINEERS PART J-JOURNAL OF ENGINEERING TRIBOLOGY*, vol. 224, pp. 453-479, 2010.
- [22] Wang, A. and Essner, A., "Three-body wear of UHMWPE acetabular cups by PMMA particles against CoCr, alumina and zirconia heads in a hip joint simulator," *WEAR*, vol. 250, pp. 212-216, 2001.
- [23] Chinas-Castillo, F. and Spikes, H. A., " Mechanism of action of colloidal solid dispersions," *Journal of Tribology*, vol. 125, pp. 552-557, 2003.
- [24] Lovell, M. R., Kabir, M. A., Menezes, P. L., and Ill, C. F. H., "Influence of boric acid additive size on green lubricant performance," *Philosophical Transactions of the Royal Society A*, vol. 368, pp. 4851-4868, 2010.
- [25] Duan, B. and Lei, H., "The effect of particle size on the lubricating properties of colloidal polystyrene used as water based lubrication additive," *WEAR*, vol. 249, pp. 528-532, 2001.
- [26] Nikas, G. K. and Sayles, R. S., "A study of lubrication mechanisms using two-phase fluids with porous bearing materials," *PROCEEDINGS OF THE INSTITUTION OF MECHANICAL ENGINEERS PART J-JOURNAL OF ENGINEERING TRIBOLOGY*, vol. 222, 2008.
- [27] Darley, H. C. H. and Gray, G. R., *Composition and Properties of Drilling and Completion Fluids*, 5 ed. Houston, TX: Butterworth-Heinemann, 1988.
- [28] Wang, Y., Zhao, Y., An, W., Ni, Z., and Wang, J., "Modeling effects of abrasive particle size and concentration on material removal at molecular scale in chemical mechanical polishing," *Applied Surface Science*, vol. 247, pp. 249-253, 2010.
- [29] Kyle, J. and terrell, E., "Smoothed Particle Methods and Their Applicability to Tribology," in *ASME/STLE 2011 International Joint Tribology Conference*, Los Angeles, California, USA, 2011.
- [30] Mpagazehe, J. N., Queiruga, A. F., and Higgs, C. F., "Towards an understanding of the drilling process for fossil fuelenergy: A continuum discrete approach," *Tribology International*, vol. Article in Press, 2012.
- [31] Martin C. Marinack, J., Mpagazehe, J. N., and C. Fred Higgs, I., "An Eulerian, Lattice-based Cellular Automata Approach for Modeling Multiphase Flows," *Powder Technology*, 2012.
- [32] Chorin, A. J., "Numerical solution of the Navier-Stokes equations," *Mathematics of Computation*, vol. 22, pp. 745 - 762, 1968.
- [33] Löhner, R., *Applied Computational Fluid Dynamics Techniques: An Introduction Based on Finite Element Methods*. West Sussex, England: John Wiley & Sons, Ltd, 2008.
- [34] Terrell, E. J. and C. Fred Higgs, I., "A Particle-Augmented Mixed-Lubrication Modeling Approach to Predicting Chemical Mechanical Polishing," *Journal of Tribology*, vol. 131, 2009.
- [35] Griebel, M., Dornseifer, T., and Neunhoeffler, T., *Numerical Simulation in Fluid Dynamics*. Philadelphia: Society for Industrial and Applied Mathematics (SIAM), 1998.
- [36] White, F. M., *Viscous Flow*: McGraw-Hill, 2006.
- [37] Cundall, P. A. and Strack, O. D. L., "Discrete numerical model for granular assemblies," *Geotechnique*, vol. 29, pp. 47-65, 1979.

- [38] McCarthy, J. J., Jasti, V., Marinack, M., and Higgs, C. F., "Quantitative validation of the discrete element method using an annular shear cell," *Powder Technology*, vol. 203, pp. 70-77, 2010.
- [39] Li, Q., Rudolph, V., Wang, F. Y., and Horio, M., "A Study of Particle Packing Compression under Fluid Drag Force by DEM Simulations," *Developments in Chemical Engineering and Mineral Processing*, vol. 13, pp. 693-708, 2005.
- [40] Marinack, M. C., Mpagazehe, J. N., and Higgs, C. F., "An Eulerian, lattice-based cellular automata approach for modeling multiphase flows," *Powder Technology*, vol. 221, pp. 47-56, May 2012.
- [41] Jhurani, S. M. and Fred Higgs III, C., "An elastohydrodynamic lubrication (EHL) model of wear particle migration in an artificial hip joint," *Tribology International*, vol. 43, pp. 1326-1338, 2010.
- [42] Shapley, N. C., Armstrong, R. C., and Brown, R. A., "Laser Doppler velocimetry measurements of particle velocity fluctuations in a concentrated suspension," *Journal of Rheology*, vol. 46, p. 241, 2002.
- [43] Li, L. and Ma, W., "Experimental Study on the Effective Particle Diameter of a Packed Bed with Non-Spherical Particles," *Transport in Porous Media*, vol. 89, pp. 35-48, 2011.
- [44] Peskin, C., "The immersed boundary method," *Acta Numerica*, pp. 479-517, 2002.
- [45] Hammache, M. and Gharib, M., "An experimental study of the parallel and oblique vortex shedding from circular cylinders," *Journal of Fluid Mechanics*, vol. 232, pp. 567-590, 1991.
- [46] Roshko, A., "On the Development of Turbulent Wakes from Vortex Streets," National Advisory Committee for Aeronautics - California Institute of Technology Report Number 1191, 1954.
- [47] Williamson, C., "Oblique and parallel modes of vortex shedding in the wake of a circular cylinder at low Reynolds numbers," *Journal of Fluid Mechanics*, vol. 206, pp. 579-627, 1989.
- [48] Nishioka and Sato, "Mechanism of determination of shedding frequency of vortices behind a cylinder at low Reynolds numbers," *Journal of Fluid Mechanics*, vol. 89, pp. 49-60, 1978.
- [49] Park, J., Kwon, K., and Choi, H., "Numerical solutions of flow past a cylinder at Reynolds numbers up to 160," *KSME International Journal*, vol. 12, pp. 1200-1205, 1998.
- [50] Immer, C., Metzger, P., Hintze, P. E., Nick, A., and Horan, R., "Apollo 12 Lunar Module exhaust plume impingement on Lunar Surveyor III," *Icarus*, vol. 211, pp. 1089-1102, 2011.
- [51] Carroll, W. F., Davis, R., Goldfine, M., Jacobs, S., L. D. Jaffe, Leger, L., Milwitzky, B., and Nickle, N. L., "Analysis of Surveyor 3 Material and Photographs Returned by Apollo12: Introduction," 1972.
- [52] Cour-Palais, B. G., "News Release 70-26," NASA1970.
- [53] Jaffe, L. D., "Blowing of Lunar Soil by Apollo 12: Surveyor 3 Evidence," *Science*, vol. 171, pp. 798-799, 1971.
- [54] Brownlee, D., Bucher, W., and Hodge, P., "Analysis of Surveyor 3 Material and Photographs Returned by Apollo12: Primary and Secondary Micrometeoroid Impact Rate on the Lunar Surface: A Direct Measurement," 1972.
- [55] Clegg, R. N., Metzger, P. T., Huff, S., and Roberson, L. B., "Lunar Soil Erosion Physics for Landing Rockets on the Moon," presented at the 42nd Lunar and Planetary Science Conference, The Woodlands, TX, 2011.

- [56] Heiken, G., Vaniman, D., and French, B. M., "Lunar Sourcebook: A User's Guide to the Moon," ed: Cambridge University Press, 1991.
- [57] Schränk, D., Sharpe, B., Cooper, B., and Thangavelu, M., *The Moon: Resources, Future Development, and Settlement*, 2nd ed. New York: Springer-Praxis, 2008.
- [58] Kobrick, R., Budinski, K., Street, K., and Klaus, D., "Three-Body Abrasion Testing Using Lunar Dust Simulants to Evaluate Surface System Materials," NASA, Cleveland, OH USA NASA/TM—2010-216781, 2010.
- [59] Jones, L., Jacques, S., Rask, J. C., Tranfield, E., Taylor, L., Kerschmann, R., and Loftus, D. J., "LUNAR DUST BIOLOGICAL EFFECTS," presented at the NASA Lunar Science Institute (NLSI) Lunar Science Conference, Ames, California, 2008.
- [60] Bahadur, S. and Badruddin, R., "Erodent Particle Characterization and the Effect of Particle Size and Shape on Erosion," *Wear*, vol. 138, pp. 189-208, 1990.
- [61] Chen, Q. and Li, D. Y., "Computer simulation of solid particle erosion," *Wear*, vol. 254, pp. 203-210, 2003.
- [62] Kobrick, R. L., Klaus, D. M., and Kenneth W. Street, J., "Validation of proposed metrics for two-body abrasion scratch test analysis standards," *Wear*, vol. 270, pp. 815-822, 2011.
- [63] Sengupta, A., Kulleck, J., Van Norman, J., and Mehta, M., "Thermal coating erosion in a simulated Martian landing environment," *Wear*, vol. 270, pp. 335-343, 2011.
- [64] Zhao, Y. and Chang, L., "A micro-contact and wear model for chemical-mechanical polishing of silicon wafers," *WEAR*, vol. 252, pp. 220-226, 2002.
- [65] Kahraman, S., "Performance analysis of drilling machines using rock modulus ratio " *Journal of the South African Institute of Mining and metallurgy*, 2003.
- [66] Fairhurst, C. and Lacabanne, W. D., "Hard rock drilling techniques," *Mine & Quarry Engineering*, vol. 23, pp. 157-161, 194-197, 1957.
- [67] Detournay, E. and Defourny, P., "A Phenomenological Model for the Drilling Action of Drag Bits," *International Journal of Rock Mechanics & Mining Sciences & Geomechanics Abstracts*, vol. 29, pp. 13-23, 1992.
- [68] Baumgart, A., "Stick-slip and Bit-Bounce of Deep-Hole Drillstrings," *Journal of Energy Resources Technology*, vol. 122, pp. 78-82, 2000.
- [69] Yigit, A. S. and Christoforou, A. P., "Stick-Slip and Bit-Bounce Interaction in Oil-Well Drillstrings," *Journal of Energy Resources Technology*, vol. 128, pp. 268-274, 2006.
- [70] Richard, T., Gernay, C., and Detournay, E., "A simplified model to explore the root cause of stick-slip vibrations in drilling systems with drag bits," *Journal of Sound and Vibration*, vol. 305, pp. 432-456, 2007.
- [71] Bruno, M., Han, G., and Honegar, C. (Winter 2005) Advanced Simulation Technology for Combined Percussion and Rotary Drilling and Cuttings Transport. *GasTIPS*.
- [72] Wijk, G., "Rotary drilling prediction," *International Journal of Rock Mechanics & Mining Sciences*, vol. 28, pp. 35-42, 1991.
- [73] Thuro, K., "Drillability prediction - geological influences in hard rock drill and blast tunnelling," *Geologische Rundschau*, vol. 86, pp. 426-438, 1997.
- [74] Brown, E. T., Green, S. J., and Sinah, K. P., "The Influence of Rock Anisotropy on Hole Deviation in Rotary Drilling - A Reveiw," *International Journal of Rock Mechanics & Mining Sciences*, vol. 18, pp. 387-401, 1981.
- [75] Jing, L. and Hudson, J. A., "Numerical Methods in Rock Mechanics," *International Journal of Rock Mechanics & Mining Sciences*, vol. 39, pp. 409-427, 2002.
- [76] Bobet, A., Fakhimi, A., Johnson, S., Morris, J., Tanon, F., and Ronald Yeung, M., "Numerical Models in Discontinuous Media: Review of Advances for Rock Mechanics

- Applications," *Journal of Geotechnical and Geoenvironmental Engineering*, vol. 135, pp. 1547-1561, 2009.
- [77] Potyondy, D. O. and Cundall, P. A., "A Bonded-Particle Model for Rock," *International Journal of Rock Mechanics & Mining Sciences*, vol. 41, pp. 1329-1364, 2004.
 - [78] Cho, N., Martin, C. D., and Sego, D. C., "A clumped particle model for rock," *International Journal of Rock Mechanics & Mining Sciences*, vol. 44, pp. 997-1010, 2007.
 - [79] Rojek, J., "Discrete Element Modelling of Rock Cutting," *Computer Methods in Materials Science*, vol. 7, pp. 224-230, 2007.
 - [80] Wang, Y. N. and Tanon, F., "Calibration of a discrete element model for intact rock up to its peak strength," *International Journal for Numerical and Analytical Methods in Geomechanics*, vol. 34, pp. 447-469, 2010.
 - [81] Stavropoulou, M., "Modeling of small-diameter rotary drilling tests on marbles," *International Journal of Rock Mechanics & Mining Sciences*, vol. 43, pp. 1034-1051, 2006.
 - [82] Johnson, S., "A New Method of Producing Laterally Stable PDC Drill Bits," *SPE Drilling & Completion*, vol. 23, pp. 314-324, 2008.
 - [83] Terrell, E., Jasti, V., and Higgs III, C. F., "Modeling the Motion of Slurry Nanoparticles during Chemical Mechanical Polishing," in *Proceedings of IMECE2005*, 2005.
 - [84] Terrell, E. J. and Higgs, C. F., "A Particle-Augmented Mixed Lubrication Modeling Approach to Predicting Chemical Mechanical Polishing," *Journal of Tribology*, vol. 131, p. 012201, 2009.
 - [85] Uhlmann, M., "An immersed boundary method with direct forcing for the simulation of particulate flows " *Journal of Computational Physics*, vol. 209, pp. 448-476, 2005.
 - [86] Donea, J., Giuliani, S., and Halleux, J. P., "An arbitrary lagrangian-eulerian finite element method for transient dynamic fluid-structure interactions," *Computer Methods in Applied Mechanics and Engineering*, vol. 33, pp. 689-723 1982.
 - [87] Hirt, C. W., Amsden, A. A., and Cook, J. L., "An arbitrary Lagrangian-Eulerian computing method for all flow speeds," *Journal of Computational Physics*, vol. 14, pp. 227-253, 1974.
 - [88] Black, A. D., Walker, B. H., Tibbitts, G. A., and Sandstrom, J. L., "PDC Bit Performance for Rotary, Mud Motor, and Turbine Drilling Applications " *SPE Drilling Engineering*, vol. 1, pp. 409-416, 1986.
 - [89] "World Energy Demand and Economic Outlook," U.S. Energy Information Administration 2010.
 - [90] Howarth, D. F. and Rowlands, J. C., "Quantitative Assesment of Rock Texture and Correlation with Drillability and Strength Properties," *Rock Mechanics and Rock Engineering*, vol. 20, pp. 57-85, 1987.
 - [91] Fear, M. J., "How to Improve Rate of Penetration in Field Operations " *SPE Drilling & Completion*, vol. 14, pp. 42-49, 1999.
 - [92] Miller, D. and Ball, A., "Rock Drilling with Impregnated Diamond Microbits - An Experimental Study," *International Journal of Rock Mechanics & Mining Sciences*, vol. 27, pp. 363 - 371, 1990.
 - [93] Mpagazehe, J. N. and Higgs, C. F., "A 3D, Transient Model to Predict Interfacial Phenomena during CMP using Computational Fluid Dynamics," *Proceedings of the Institution of Mechanical Engineers, Part J, Journal of Engineering Tribology*, vol. Accepted for publication, 2012.

- [94] Sawyer, W. G., "Surface shape and contact pressure evolution in two component surfaces: application to copper chemical mechanical polishing," *Tribology Letters*, vol. 17, 2004.
- [95] Luo, J. and Dornfeld, D. A., "Mechanical removal mechanism in chemical mechanical polishing: theory and modeling," *IEEE TRANSACTIONS ON SEMICONDUCTOR MANUFACTURING*, vol. 14, pp. 112-133, 2001.
- [96] Luo, Q., Ramarajan, S., and Babu, S. V., "Modification of the Preston equation for the chemical-mechanical polishing of copper," *Thin Solid Films*, vol. 335, pp. 160-167, 1998.
- [97] Shan, L., Levert, J., Meade, L., Tichy, J., and Danyluk, S., "Interfacial Fluid Mechanics and Pressure Prediction in Chemical Mechanical Polishing," *Journal of Tribology*, vol. 122, 2000.
- [98] C. Fred Higgs, I., Ng, S. H., Borucki, L., Yoon, I., and Danyluk, S., "A Mixed-Lubrication Approach to Predicting CMP Fluid Pressure Modeling and Experiments," *Journal of The Electrochemical Society*, vol. 152, pp. G193-G198, 2005.
- [99] Park, S.-S., Cho, C.-H., and Ahn, Y., "Hydrodynamic analysis of chemical mechanical polishing process," *Tribology International*, vol. 33, pp. 723-730, 2000.
- [100] Gohar, R., *Elastohydrodynamics*. New York, New York: John Wiley & Sons, 1988.
- [101] Terrell, E. J. and III, C. F. H., "A Particle-Augmented Mixed-Lubrication Modeling Approach to Predicting Chemical Mechanical Polishing," *Journal of Tribology*, vol. 131, 2009.
- [102] Sampurno, Y., Sudargho, F., Zhuang, Y., Goldstein, M., and Philipossian, A., "Feasibility of real-time detection of abnormality in inter layer dielectric slurry during chemical mechanical planarization using frictional analysis," *Thin Solid Films*, vol. 516, pp. 7667-7674, 2008.
- [103] Levert, J. A., Mess, F. M., Salant, R. F., Danyluk, S., and Baker, A. R., "Mechanisms of Chemical-Mechanical Polishing of SiO₂ Dielectric on Integrated Circuits," *Tribology Transactions*, vol. 41, pp. 593-599, 1998.
- [104] Zantye, P. B., Kumar, A., and Sikder, A. K., "Chemical mechanical planarization for microelectronics applications," *Materials science & engineering. R, Reports*, vol. 45, pp. 89-220, 2004.
- [105] Chang, S.-H., "A dishing model for STI CMP process," *Microelectronic Engineering*, vol. 82, pp. 136-142, 2005.
- [106] Che, W., Guo, Y., Chandra, A., and Bastawros, A., "A Scratch Intersection Model of Material Removal During Chemical Mechanical Planarization (CMP)," *Journal of Manufacturing Science and Engineering*, vol. 127, pp. 545-554, 2005.
- [107] Oh, S. and Seok, J., "An integrated material removal model for silicon dioxide layers in chemical mechanical polishing processes," *Wear*, vol. 266, pp. 839-849, 2009.
- [108] Xin, J., Cai, W., and Tichy, J. A., "A fundamental model proposed for material removal in chemical-mechanical polishing," *Wear*, vol. 268, pp. 837-844, 2010.
- [109] Kong, Z., Oztekin, A., Beyca, O. F., Phatak, U., Bukkapatnam, S. T. S., and Komanduri, R., "Process Performance Prediction for Chemical Mechanical Planarization (CMP) by Integration of Nonlinear Bayesian Analysis and Statistical Modeling," *IEEE TRANSACTIONS ON SEMICONDUCTOR MANUFACTURING*, vol. 23, pp. 316-327, 2010.
- [110] Tsai, H.-J., Huang, P.-Y., Tsai, H.-C., and Chiu, S.-J., "Chemical Mechanical Polishing in Elastic Contact and Partial Hydrodynamic Lubrication: Modeling and Experiments," *Materials and Manufacturing Processes*, vol. 26, pp. 319-324, 2011.
- [111] Wei, C.-C., Horng, J.-H., Lee, A.-C., and Lin, J.-F., "Analyses and experimental confirmation of removal performance of silicon oxide film in the chemical-mechanical

- polishing (CMP) process with pattern geometry of concentric groove pads," *Wear*, vol. 270, pp. 172-180, 2011.
- [112] Wu, L. and Yan, C., "Modeling of the Effect of Wafer Topography on Chemical Mechanical Polishing Processes Based on 3D Analysis," *Journal of The Electrochemical Society*, vol. 158, pp. H239-H248, 2011.
 - [113] Lei, J., Guo, D., Luo, J., and Pan, G., "Probing Particle Movement in CMP with Fluorescence Technique," *Journal of The Electrochemical Society*, vol. 158, pp. H681-H685, 2011.
 - [114] Bastawros, A., Chandra, A., Guo, Y., and Yan, B., "Pad Effects of Material-Removal Rate in Chemical-Mechanical Planarization," *Journal of ELECTRONIC MATERIALS*, vol. 31, pp. 1022-1031, 2002.
 - [115] Luo, J. and Dornfeld, D. A., "Effects of Abrasive Size Distribution in Chemical Mechanical Planarization: Modeling and Verification," *IEEE TRANSACTIONS ON SEMICONDUCTOR MANUFACTURING*, vol. 16, pp. 469-476, 2003.
 - [116] Ahmadi, G. and Xia, X., "A Model for Mechanical Wear and Abrasive Particle Adhesion during the Chemical Mechanical Polishing Process," *Journal of The Electrochemical Society*, vol. 148, pp. 99-109, 2001.
 - [117] Zeng, T. and Sun, T., "Size Effect of Nanoparticles in Chemical Mechanical Polishing - A Transient Model," *IEEE TRANSACTIONS ON SEMICONDUCTOR MANUFACTURING*, vol. 18, pp. 655-663, 2005.
 - [118] Sundararajan, S., Thakurta, D. G., Schwendeman, D. W., Murarka, S. P., and Gill, W. N., "Two-Dimensional Wafer-Scale Chemical Mechanical Planarization Models Based on Lubrication Theory and Mass Transport," *Journal of The Electrochemical Society*, vol. 146, pp. 761-766, 1999.
 - [119] Neyer, S., Ozdoganlar, B., and C. Fred Higgs, I., "An Investigation of the Influence of Orientation on CMP through Nanoscratch Testing," presented at the Materials Research Society Symposium, San Francisco, CA, 2009.
 - [120] Steijn, R. P., "Friction and wear of single crystals," *WEAR*, vol. 7, pp. 48-66, 1964.
 - [121] Suh, N. P., "The delamination theory of wear," *WEAR*, vol. 25, pp. 111-124, 1973.
 - [122] Larsen-Basse, J., "Role of microstructure and mechanical properties in abrasion," *Scripta Metallurgica et Materialia*, vol. 24, pp. 821-826, 1990.
 - [123] Godet, M., "Third-Bodies in Tribology," *WEAR*, vol. 136, pp. 29-45, 1990.
 - [124] Tripathi, S., Doyle, F. M., and Dornfeld, D. A., "Fundamental Mechanisms of Copper CMP – Passivation Kinetics of Copper in CMP Slurry Constituents," presented at the Materials Research Society Symposium, San Francisco, CA, 2009.
 - [125] Balakumar, S., Haque, T., Kumar, A. S., Rahman, M., and Kumar, R., "Wear Phenomena in Abrasive-Free Copper CMP Process," *Journal of The Electrochemical Society*, vol. 152, pp. G867-G874, 2005.
 - [126] Paul, E., Horn, J., Li, Y., and Babu, S. V., "A Model of Pad-Abrasive Interactions in Chemical Mechanical Polishing," *Electrochemical and Solid-State Letters*, vol. 10, pp. H131 - H133, 2007.
 - [127] Si, L., Guo, D., Luo, J., Lu, X., and Xie, G., "Abrasive rolling effects on material removal and surface finish in chemical mechanical polishing analyzed by molecular dynamics simulation," *Journal of Applied Physics*, vol. 109, 2011.
 - [128] Preston, F. W., "The theory and design of plate glass polishing machines," *Journal of the Society of Glass Technology*, vol. 11, pp. 214-256, 1927.
 - [129] Shi, F. G. and Zhao, B., "Modeling of chemical-mechanical polishing with soft pads," *Applied Physics A: Materials Science & Processing*, vol. 67, pp. 249-252, 1998.

- [130] Bai, J., Zhao, Y. W., and Wang, Y. G., "A mathematical model for material removal and chemical–mechanical synergy in chemical–mechanical polishing at molecular scale," *Applied Surface Science*, vol. 253, pp. 8489–8494, 2007.
- [131] Coppeta, J., Rogers, C., Racz, L., Philipossian, A., and Kaufman, F. B., "Investigating Slurry Transport Beneath a Wafer during Chemical Mechanical Polishing Processes," *Journal of The Electrochemical Society*, vol. 147, pp. 1903-1909, 2000.
- [132] Mueller, N., Rogers, C., Manno, V., White, R., and Moinpour, M., "In Situ Investigation of Slurry Flow Fields during CMP," *Journal of The Electrochemical Society*, vol. 156, pp. H908 - H912, 2009.
- [133] Kobrick, R. L., Budinski, K. G., K. W. Street, J., and Klaus, D. M., "Three-Body Abrasion Testing Using Lunar Dust Simulants to Evaluate Surface System Materials," NASA, Cleveland, OH USA2010.
- [134] Mpagazehe, J. N., Kenneth W. Street, J., Delgado, I. R., and III, C. F. H., "Erosive Wear Characterization of Materials for Lunar Construction," NASA NASA/TM—2012-217706, 2012.
- [135] Lane, J. E., Metzger, P. T., Immer, C. D., and Li, X., "Lagrangian Trajectory Modeling of Lunar Dust Particles," in *Earth & Space*, Long Beach, California, 2008.